Università degli Studi di Napoli Federico II

Dottorato in Ingegneria Aerospaziale, Navale e della Qualità
XXII ciclo

Dipartimento di Ingegneria Aerospaziale

On the Aerodynamic Force of the Oscillating Airfoils

Tutor
Ch.mo prof. Renato Tognaccini

Candidato
Claudio Maria Marongiu

Anno Accademico 2009

Abstract

The measure of the aerodynamic force around an oscillating airfoil represents the object of many theoretical and experimental researches in the modern Aerodynamics. The classical *near field* methods, based on the solid surface integration of the pressure and shear stresses, and the *far field* methods, obtained through the integral balance of the momentum equations, are the main categories in which all the force calculation techniques are included. The *far field* methods offer several advantages with respect to the classical *near field* ones and represent a positive solution to several limitations observed in the applications. Currently, the use of *far field* methods in the numerical solutions is limited only to the steady flows. It does not exist a well assessed *far field* method for unsteady flow regimes.

The present thesis concerns the development of a new measurement technique of the aerodynamic force by means of a *far field* approach. The method is based solely on the knowledge of the vorticity field. The role of the Lamb vector (i.e. the vortex force) in the determination of the aerodynamic force is clearly highlighted.

Several numerical solutions around an airfoil in pitching conditions (from pre-stall to the dynamic stall) have been achieved in the flow transition regime. The method employed in the fluid dynamic computations is based on the Reynolds Averaged Navier Stokes (RANS) equations in an unsteady reference system. The results obtained in the thesis demonstrate the effectiveness of the present RANS method in the prediction of the dynamic stall characteristics.

By means of the new *far field* method, the real possibility to measure the aerodynamic force also in case of unsteady flows has been demonstrated. In addition, useful qualitative and quantitative information for the aerodynamic design have been extracted through the unsteady breakdown of the force. This technique can be exploited also in the experimental applications, in which the measurement of the aerodynamic force without the knowledge of the pressure is particular critical.

Contents

List of Figures

Symbols

R	gas constant
γ	ratio of the specific heat coefficients
ρ	density
p	pressure
e	internal specific energy
E	total specific energy
λ	thermal conductivity
T	temperature, time period
$\underline{q}$	thermal flux
H	total specific enthalpy
t	time
$\underline{\mathbf{x}}$	position vector
$\underline{n}$	normal direction versor
$\underline{i}$	x direction versor
$\underline{j}$	y direction versor
$\underline{k}$	z direction versor
u, v, w	cartesian components of the velocity
q	velocity module
$\underline{\mathbf{u}}$	velocity vector
ϕ	velocity potential
$\underline{\omega}$	vorticity, $\underline{\nabla} \times \underline{\mathbf{u}}$
ω	angular frequency, turbulence frequency ε/κ
δ	boundary layer thickness
$\underline{\boldsymbol{l}}$	Lamb vector $\underline{\omega} \times \underline{\mathbf{u}}$
μ	dynamic viscosity
ν	kinematic viscosity μ/ρ
$\underline{\underline{\tau}}$	viscous stress tensor
μ_t	turbulent viscosity
κ	turbulent kinetic energy
$\underline{\underline{\tau}}^t$	Reynolds stress tensor

Ω	fluid volume
$\partial\Omega$	boundary of the fluid volume
Σ	external surface
B	solid body volume
∂B	solid body surface
$\underline{\underline{\mathbf{I}}}$	unit tensor
$\langle \cdot \rangle$	mean operator
$\underline{\nabla} \cdot$	gradient operator
$\underline{\nabla} \times \cdot$	curl operator
$\underline{\mathbf{F}}$	aerodynamic force
U_∞	free stream velocity
α	angle of attack
α_0	amplitude of the angle of attack motion
α_m	mean angle of attack
k	reduced frequency $= \frac{\omega c}{2U_\infty}$
C_P	Pressure coefficient, $\frac{2(p-p_\infty)}{\rho_\infty U_\infty^2}$
C_f	Skin friction coefficient, $\frac{2\tau_w}{\rho_\infty U_\infty^2}$
C_l	lift coefficient
C_d	drag coefficient
C_m	moment coefficient
$(\cdot)_\Omega$	volume contribution to the aerodynamic coefficient
$(\cdot)_\Sigma$	surface contribution to the aerodynamic coefficient
$(\cdot)_{\dot{\omega}}$	hydrodynamic impulse contribution to the aerodynamic coefficient
$(\cdot)_B$	body motion contribution to the aerodynamic coefficient
Re	Reynolds number
M	Mach number
Pr	Prandtl number

Acronyms

AIAA	American Institute for Aeronautics and Astronautics
CFD	Computational Fluid Dynamics
DES	Detached Eddy Simulation
DNS	Direct Numerical Simulation
DSV	Dynamic Stall Vortex
DTS	Dual Time Stepping
LDV	Laser Doppler Velocimetry
LES	Large Eddy Simulation
LSB	Laminar Separation Bubble
PIV	Particle Image Velocimetry
RANS	Reynolds Averaged Navier Stokes
SST	Shear Stress Transport
TNT	Turbulent Non Turbulent
ZEN	Zonal Euler Navier

Chapter 1

Introduction

1.1 Scientific and industrial motivations

The Aerodynamics of the oscillating airfoils has been the object of important researches in fluid dynamics since the 60's. Nowadays the motivations that encourage this kind of studies originate from the plurality of the applications in several technological sectors. Some examples in which the unsteady Aerodynamics of oscillating wings or airfoils is fundamental are reported in the following.

In the aeronautical industry the unsteady Aerodynamics is essential for the helicopter flight. Of particular concern is the Aerodynamics of the main rotor. It has the double role to balance the helicopter weight and to supply the thrust necessary to advance in the flight. Several phenomena that in the classical steady Aerodynamics are usually well distinguished, occur on the same rotor blade in few tenths of a seconds. Taking as an example the main rotor of the Agusta-Westland AW119, with a diameter of 10.83m, the nominal maximum speed reached by the helicopter is about 257 km/h, as indicated by the manufacturer. By considering a rotational speed of 400rpm, a simple computation of the Mach number reached at the tip during the advancing phase gives a value greater than 0.8 without considering the additional effects of the blade motions, which means a full compressible regime occurs. Conversely, in the region of the retreating blade, the composition of the free stream velocity with the rotational one produces so small total kinematic velocities that the blades run the risk to stall. This phenomenon

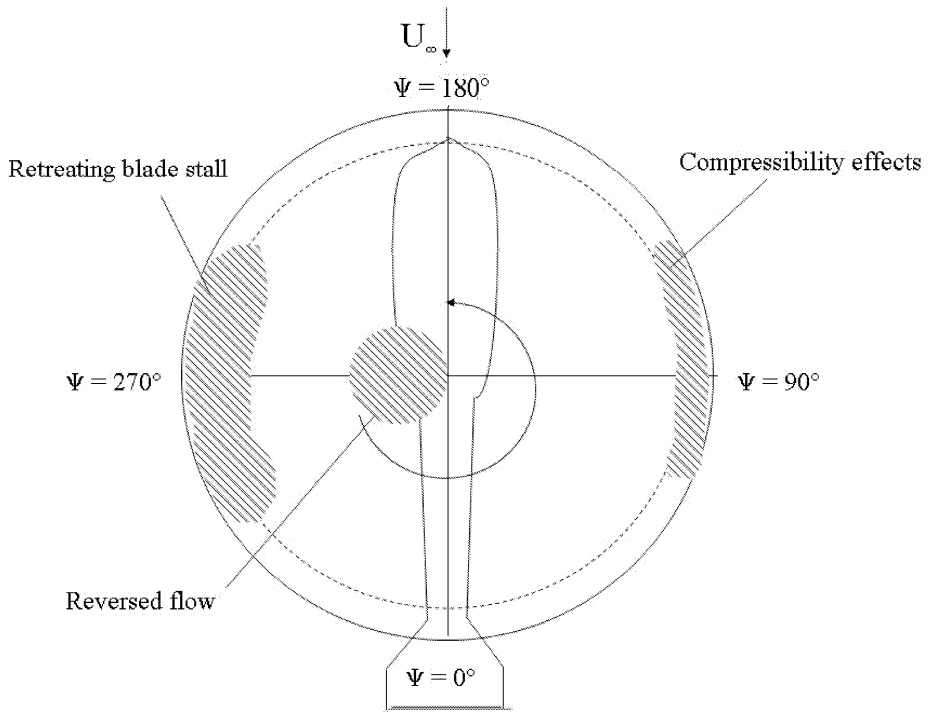

Figure 1.1: Scheme of the unsteady aerodynamic phenomena on an helicopter rotor.

is usually identified as *dynamic stall*. Zones of reverse flow arise near the hub as well. A scheme of the aerodynamic phenomena occurring on a helicopter rotor are represented in figure (1.1). In the 60's, a quite similar behaviour in terms of flow phenomena was discovered by Ham [1], considering the flow past an airfoil in pitching conditions. This finding produced a great number of researches oriented to the study of the oscillating airfoil Aerodynamics. Generally, the *dynamic stall* is introduced by referring to any lifting surface in which the combination of its motion with the asymptotic flow conditions produces a dynamically stalled condition [2]. In the forward flight case, the maximum velocity of an helicopter is strongly limited by these factors and possible progresses are achievable only by improving the blade design or introducing control devices to alleviate the dynamic stall phenomenon.

The studies on the unsteady Aerodynamics, and in particular on the

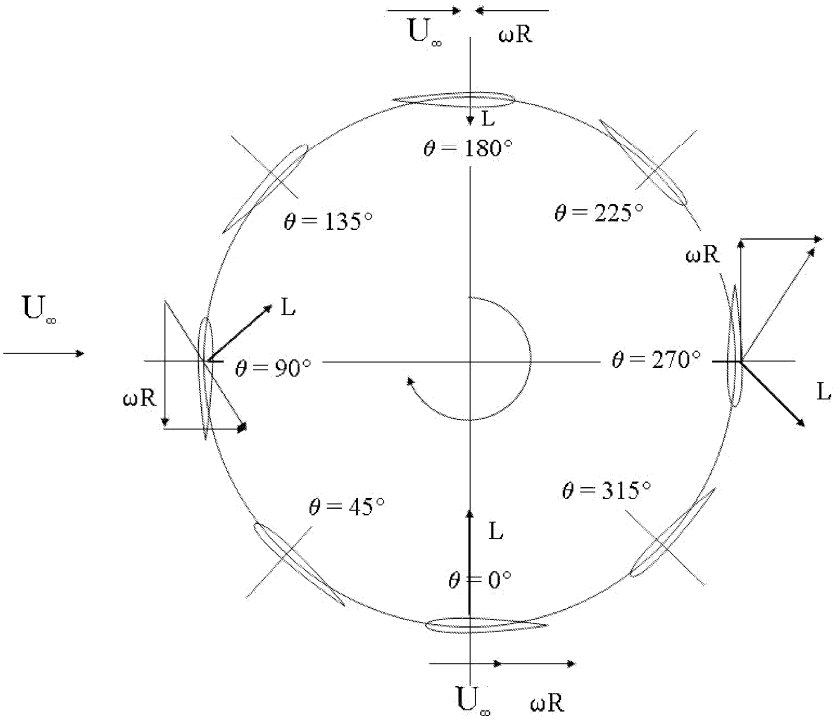

Figure 1.2: Composition of the effective velocities viewed by the blade of a vertical axis wind turbine.

oscillating airfoils, is encountered in many other technological contexts. The design of rapidly maneuvering aircrafts, for example, has the objective to extend the boundaries of the flight envelope by exploiting the unsteady effects of the Aerodynamics. In this direction, numerical and experimental works are becoming popular since the 80's highlighting the limited applicability of the linear steady Aerodynamics in such situations. Also in this field, many basic studies are carried out on two and three dimensional pitching and rolling models [3]. The severe pitch roll and yaw rates, of the order of the ten degrees per second, applied to the lifting surfaces of such aircrafts, produce strong non linear aerodynamic phenomena such as the dynamic stall.

Similar problems arise on the blades of the wind turbines used for the electrical power generation, even if for different flow parameters. The working conditions are easily altered by any change in the wind direction reducing the

aerodynamic efficiency. The blade sections work in a wide range of angles of attack and for some conditions can meet the dynamic stall phenomenon (see the scheme in figure 1.2). This problem is made critical by the relatively low Reynolds number of the flow ($\sim 10^5$). For both the horizontal and the vertical axis wind turbines, the exact knowledge of the aerodynamic load intensities can improve the design and the structural life of the plant in terms of fatigue limits. Furthermore, other requirements, such as the low sound emissions, must be respected in order to reduce the environment impact. The dynamic stall is the object of intensive investigations both numerical and experimental, because may affect the effectiveness of the whole wind turbine plant [4]. In this regard, Carr [2] pointed out that an error of 30% on the aerodynamic loads corresponds to a reduction of 70% of the life duration of a wind turbine.

In each of these scientific and technological fields, advancements and progresses on the performance are achievable by improving the aerodynamic design of the oscillating airfoils.

1.2 Characteristics of the unsteady airfoils

The first theoretical studies on the non uniform airfoil Aerodynamics were conducted in the 30's thanks to Burgers and Von Karman [5]. The basic concept was that any time change in the airfoil state is equivalent to a time variation in the angle of attack. This point of view allows for a first level of interpretation of the fundamental characteristics of the unsteady Aerodynamics (McCroskey 1982, [6]).

A first issue of the pitching airfoil Aerodynamics is that the unique correspondence between the angular position and the lift and drag experienced by the airfoil is lost. For a given flow incidence α different values of the aerodynamic force may correspond that depend on the time response of the flow-airfoil system. With respect to the corresponding steady performances, more or less large hysteresis loops are observed when a lift or drag curve is drawn as function of the angle of attack α. The time lag occurring between the angle of attack and the applied load demonstrates that the flow exhibits

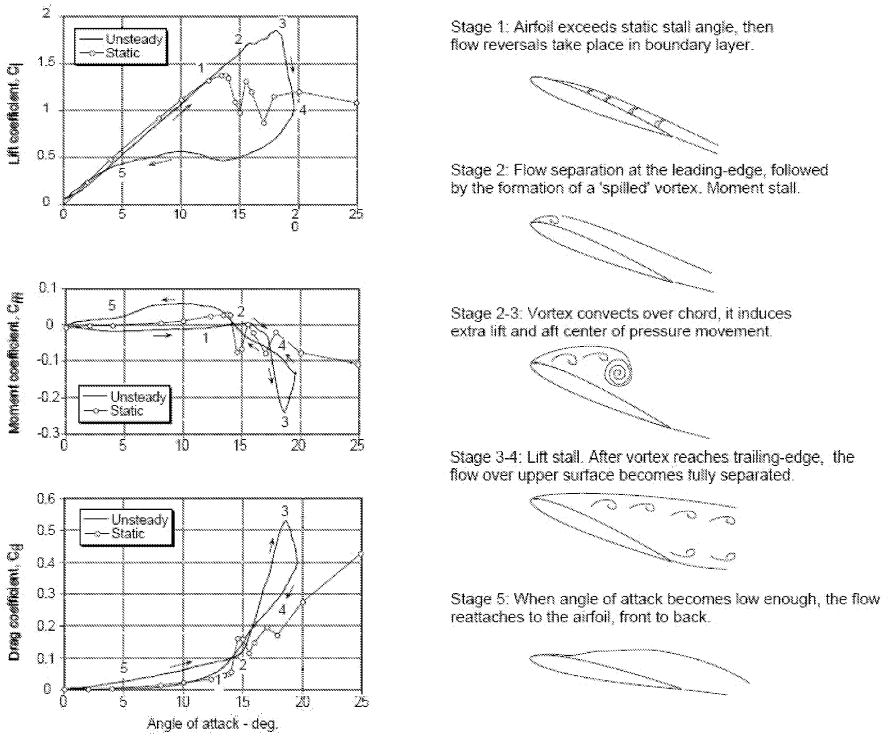

Figure 1.3: Unsteady aerodynamic characteristics of a pitching airfoil. $-\circ-$ static data, – dynamic data. From [7]

a sort of memory of the past time history. Within this frame, several static phenomena have to be revisited under the perspective of the unsteadiness. One of these is the aerodynamic stall of the airfoil, that, as introduced in the previous section, is of fundamental importance in many application fields. By comparing the dynamic stall of a wing or an airfoil with the corresponding static one, several differences appear.

In figure (1.3), the typical unsteady aerodynamic characteristics of a pitching airfoil are plotted. The corresponding static data are also drawn for reference. It is a common practice to subdivide the unsteady aerodynamic cycle as a sequence of events (Leishman [8]). Starting from the stage (1), which corresponds to the static stall of the airfoil, the first substantial

difference is that under dynamic conditions the lift curve continues to grow. An extrapolation of the linear slope is observed up to the points (2) or (3). The excess of lift is explained by a production of vorticity in the boundary layer. The vortices contribute to the flow expansion on the upper side of the airfoil providing a lift increase. But, if the effect on the lift seems to be almost linear, the flow structure is completely different from the steady situation. Zones of reverse but confined flow arise on the upper side of the airfoil. From the stage (2) the so called dynamic stall vortex is formed and a change on the lift curve slope takes place. The stall of the moment coefficient occurs between the stages (2) and (3) before the lift stall. It is associated with the position of the dynamic stall vortex, that during its movement produces an unbalanced pressure distribution. In the helicopter rotors, the moment stall is particularly dangerous because of the strong torsional loads transferred to the structure [9]. The maximum peak of lift is reached when the dynamic stall vortex is approximately at the trailing edge of the airfoil. Then, it is shed in the wake, and secondary vortices detach. During the decreasing phases (3) and (4), the flow remains separated for a certain time interval, during which the process of the reattachment begins. The reattachment point advances at a velocity less than U_∞ and after several time units the flow acquires again the linear behaviour (stage 5).

From the point of view of the aerodynamic design, a very important parameter is the so called *aerodynamic damping* coefficient, which is a measure of the work done by the aerodynamic forces on the airfoil in pitching conditions. The most dangerous situation (negative damping) occurs when the airfoil receives energy from the fluid producing an unstable and diverging condition. The aerodynamic design of a pitching airfoil has the objective to control and reduce the damping associated with the moment curves.

In literature, (McCroskey [10]), three regimes of pitching conditions are usually classified for an oscillating airfoil.

The *pre stall* is the regime in which the pitching motion amplitude is smaller than the static stall angle. No significant separations arise, and the hysteresis associated with the aerodynamic coefficients are small.

The *light stall* regime is characterized by a pitching motion in which stalled and non stalled conditions alternate. The instantaneous flow incidence exceeds the static stall angle only for a portion of the entire loop. The reattachment process has the time to be completed in a fraction of the whole period. Usually the *light stall* occur at low values of the adimensional (i.e. reduced) frequency.

The *deep stall* regime is encountered when the angular motion is such that fully separated flow conditions arise for the most part of the cycle. In such a situation, the flow reattachment is not completed within an oscillating period. Large hysteresis of the aerodynamic coefficients are obtained and the extension of the separated flow is of order of the airfoil chord length.

1.3 Literature overview

While the Aerodynamics of the pre-stall regimes is replicated by analytical and semi-empirical models in a satisfactory manner, a *light stall* or a *deep stall* regime is not tackled in the same straightforward fashion. The difficulty derives from the many factors involved in the determination of the dynamic stall typology and in the lack of a complete physical modelling of the phenomenon. Such factors are summarized below:

- geometry of the airfoil/wing
- typology of the motion
- unsteadiness (reduced frequency, natural flow frequencies, ...)
- compressibility effects
- viscous effects
- transition
- turbulence
- flow three dimensionality

In addition, in real applications, the external Aerodynamics and the dynamics of the structures are coupled in a unique complex physical system. A full characterization of an airfoil in dynamic conditions needs to establish reliable relationships between each of these factors. The aerodynamic force past an oscillating airfoil can be evaluated by means of three methodologies: the experimental measurements, the Computational Fluid Dynamics (CFD) and the semi-empirical methods. In the following an overview on the state of art in each of these field is given.

1.3.1 Experimental investigations

The experimental research has been the pioneer in many sectors of the applied Aerodynamics. In the case of oscillating airfoil investigations, the first systematic studies were due to McCroskey in the 70's. The work of McCroskey et al. [11] in 1976 remarked some fundamental characteristics of the two dimensional oscillating airfoil Aerodynamics. A first indication of the dynamic stall vortex (DSV) speed was also given. Between the 1976 and 1980 Ericsson and Reding, [12, 13, 14] provided useful physical information on the dynamic stall. A first analytical method was achieved as well. A more comprehensive exposition of the dynamic stall features and a classification based on geometrical and physical parameters can be found in the work of McCroskey in 1981 [10]. Later, specific experiments on some parameters of the phenomenon became to appear, such as the pitch rate, the Reynolds number and the compressibility [15, 16, 17]. In 1988, the review paper of Carr [2] pointed out the relevance on the topic by collecting the main results achieved until then. In the recent years, several experimental researches have been published concerning the use of the flow control techniques applied the dynamic stall [18, 19, 20].

However, even if at the end of the 80's, the experimental researches investigated the main aspects of the oscillating airfoil flows, no satisfactory results were achieved on the accurate prediction of the aerodynamic force. Many experimental tests on the dynamic stall used the wall integration methods

(*near field*) of the pressure signals providing reliable values only for the lift component. In such cases, the use of the aerodynamic balances is often not feasible because of the movement of the test model and the interferences associated with the mechanical vibrations. Accurate calculations of the drag are quite rare for an oscillating airfoil for these reasons.

More sophisticated and less intrusive approaches were developed in the 90's, by introducing the flow visualization methods like the Laser Doppler Velocimetry (LDV) and Particle Image Velocimetry (PIV) techniques. Their employment in case of oscillating airfoils began some years later. The advantages of these approaches are undisputed, even though the problem of measuring the aerodynamic force through the flow field occurs. This problem was tackled by Panda & Zaman [21], in 1994, by exploiting the vorticity field for the measure of the lift of an oscillating airfoil. Special techniques based on the *far field* methods are developed expressly for these applications, [22]. Wernert et al. in 1996 [23] used a PIV technique to examine the flow field around an oscillating airfoil at low Reynolds number. Recently (2008-2009) Ferreira et al. [24, 25] published an application of the PIV technique to measure the unsteady aerodynamic loads on a vertical axis wind turbine model.

1.3.2 Numerical simulations

With a delay of about ten years with respect to the experimental results, reliable CFD simulations of the flow past oscillating airfoils appeared in the 90's. The reasons for such a delay are manifold. The turbulence represents a crucial point for the numerical simulations of any flow at Reynolds number greater than 10^4. Alternative methods to the Direct Numerical Solution (DNS) of the Navier Stokes equations are introduced to avoid the Reynolds limitations arising from the wide range of time and spatial scales to be solved in a turbulent flow. A proper compromise between the computational cost and the turbulence modeling accuracy yields to define a hierarchy of intermediate approaches such as the Large Eddy Simulation (LES), the Detached

Eddy Simulation (DES), and the Reynolds Average Navier Stokes (RANS) methods (Spalart [26]). Concerning the turbulent simulation of an oscillating airfoil the only feasible method remains the one based on the RANS equations in the unsteady form. To date, it is still the unique approach able to respond positively to the industrial requirements in terms of CPU time and computational cost.

However, in the case of oscillating airfoils, the problem complicates due to the introduction of moving body techniques and of the massive separations flows typical in the dynamic stall. As the computer power grew more realistic simulations were performed first in two dimensional cases, [27] and then over three dimensional geometries [28]. In 2005, Spentzos et al. [29, 30, 31] performed three dimensional RANS simulations of a dynamic stall on wings with different planforms. Unsteady RANS simulations of multi-blade rotors (UH60) including the deformation data are becoming feasible with the use of highly performing computers, as demonstrated by Hahn et. al. in 2006 [32, 33] and by Choi et al. in 2007 [34]. Besides, numerical flow control techniques applied to the dynamic stall , [35, 36], and procedures design and optimization of the oscillating airfoils, [37], have been developed in the last years.

However a crucial point remains the turbulence modeling and its validation in so different flow conditions. The problem of the laminar-turbulent transition and of the massive separated flows is still far to be resolved (Van Dyken et al., [38]). Geissler & Haselmeyer [39] pointed out these aspects for the dynamic stall of a 2D-wing. New experimental and numerical works continue to be published, (Martinat et al. 2008 [40]) providing useful information to establish the confidence level of the RANS approach for the simulation of such complex flows. For the near future other techniques as the LES methods are designed only for moderate Reynolds flows without complex geometries. In this regard, a significant LES application of the flow past an oscillating airfoil was achieved in 2006 at a Reynolds number of order 10^5 by Nagarayan et al. [41].

In principle, the computation of the aerodynamic force through a nu-

merical flow solution should not represent any difficulty. But the practical experience disproves this statement. The numerical prediction of the aerodynamic drag represents one of the most delicate aspects of an airfoil or wing design already for the steady configurations. The American Institute for Aeronautics and Astronautics (AIAA) periodically plans dedicated workshops on the drag prediction of aeronautical configurations [42, 43, 44]. The goal of numerically predicting the true drag with the accuracy of one count ($\Delta C_d = 10^{-4}$) seems to be still far from the industrial practice, even if this uncertainty for a commercial aircraft may correspond to about one thousand of kilograms in terms of payload [45]. This gives an idea of the tremendous impact that a small error on the drag has on the whole perfomance of an aircraft, and the consequences in terms of engine design, weight and consumptions. The problems increase for the oscillating airfoils or wings. To tackle this problem, the CFD community holds a particular interest on the capabilities of the *far field* methods applied to a numerical flow solution. Even if the *near field* and *far field* formulations provide the same information, on condition that the numerical solution is fully converged everywhere in the field and the scheme is conservative, there is the possibility through the *far field* methods to exclude some spurious contributions from the aerodynamic force computation. These techniques allow to obtain a weaker grid dependency on the computed drag, so avoiding expensive convergence studies, especially on complex and three dimensional configurations, as pointed in the works of Paparone & Tognaccini, [46], and Tognaccini [47, 48].

1.3.3 Semi-empirical methods

A third way to compute the aerodynamic force is represented by the use of semi-empirical methods. In spite of the popularity of the CFD methods and of the important progresses achieved in the wind tunnel measurements, the development of the semi-empirical methods covers a significant part of the research on the dynamic stall. In fact, in case of effective rotorcraft design the use of such methods is unavoidable since the high computational

effort of a numerical simulation and the costs of the wind tunnel experiments. Many all-comprehensive flight-mechanic softwares incorporate several analytical models able to predict the characteristics of the dynamic stall of airfoils. The Beddoes-Leishman method [49] is one of the most widely used. Several modifications and improvements of the original version have been proposed during the years [50]. However other models are also successfully employed as well [51]. For small angular oscillations these models exploit the theories of the linear unsteady aerodynamics and for the dynamic stall conditions use empirical correlations based on the flow physics observations. The input of such models consist of a series of parameters depending on the airfoil characteristics. The tuning and the improvements of such methods can be achieved only by providing new and more accurate correlations between the unsteady flow evolution and the aerodynamic force experienced by the airfoil.

1.4 Objectives

The literature survey has shown that the calculation of the aerodynamic force for an oscillating airfoil is a critical problem in both the experimental and numerical aerodynamics. The *far field* methods offer several advantages with respect to the classical *near field* methods and they represent a positive solution to several limitations observed in the applications.

First of all, they can allow for an explicit interpretation of the physical processes involved in the genesis of the aerodynamic force. By means of the integral balance on an opportune control volume, the breakdown of the aerodynamic coefficients is possible and the specific contributions to the total drag (induced, viscous and wave drag), are definable (Destarac & van der Vooren [52], Yamazaki et al. [53]). Of particular importance for the designers is the computation of the induced drag (Spalart, 2008 [54]). Conversely, with a *near field* method only the mechanical breakdown of the aerodynamic force (pressure and viscous contributions) is obtainable.

In the experimental aerodynamics, the *far field* methods are employed because they represent an effective and non intrusive technique to extract

the aerodynamic force from a wind tunnel simulation. In the last years, the renewed interest on these aspects has been due to the growing popularity of measurement techniques such as the PIV.

In the computational fluid dynamics, the *far field* techniques can be arranged in such a way to reduce grid dependency of the aerodynamic force components and to eliminate the spurious contributions associated with the drag.

Currently, the use of *far field* methods in the numerical solutions is limited only to the steady flows. It does not exist a well established and tested *far field* method for unsteady flow regimes.

On the basis of the above observations, the objectives of the present thesis are defined as follows:

- to assess the reliability of the unsteady RANS simulations against the experimental data of flows past oscillating airfoils.
- to define a *far field* method for the prediction of the aerodynamic force suitable for unsteady and turbulent flows.
- to enhance the dynamic stall description by using the *far field* point of view.
- to provide useful information for the input of the semi-empirical methods in the prediction of dynamic stall loads

1.5 Outline

The thesis is organized as follows:

- in chapter 2, a description of the governing equations and of CFD flow solver used for the flow simulations is given. The numerical solutions have been obtained using a standard finite volume method solving the compressible RANS equations, The turbulent calculations are performed with different two equation turbulence models.

- in chapter 3, a review of the unsteady aerodynamics for inviscid flows is reported. The analytical solution of Theodorsen, [55], is demonstrated and compared with an inviscid unsteady flow solution around an oscillating airfoil. Some fundamental mechanisms concurring in the determination of the aerodynamic force are highlighted.

- in chapter 4, a new *far field* method is developed and adapted to the numerical flow solutions of the RANS codes. An original theory developed in the ambit of the Vortex Dynamics has been revisited and discussed for case at high Reynolds number. Several applications on the steady RANS solutions demonstrate the possibility to infer the aerodynamic force by means of the knowledge of the vorticity field.

- in chapter 5, the CFD simulation of a dynamic stall past an oscillating airfoil at transitional Reynolds number is carried out. Three oscillating regimes have been investigated: the *pre stall* , the *light stall* and the *deep stall* case. The reliability of the present RANS method has been confirmed by the comparisons with the data of a recent experiment and with other numerical solutions.

- in chapter 6, a discussion on the dynamic stall features is carried out by exploiting the *far field* point of view. A criterion for the dynamic stall onset has been identified and useful information about the dynamic stall vortex in terms of position and velocity are given as well.

- in chapter 7 the conclusions of the work are drawn.

Chapter 2

Mathematical and numerical models

In this chapter, the fundamental equations of the Fluid Dynamics are reported. A brief description of the numerical models employed in the simulations is presented.

2.1 Governing equations

The most accurate mathematical model for the description of the fluid motion is represented by the Navier Stokes equations [56]. In the present study, the fluid is the air behaving as a single phase perfect gas without chemical reactions. The thermodynamic state is described by the perfect gas law:

$$p = \rho R T \tag{2.1}$$

In equation (2.1), p is the thermodynamic pressure, ρ is the flow density, R is the gas constant and T is the temperature. The second state equation relates the specific internal energy e to the pressure and the density:

$$e = \frac{1}{\gamma - 1}\frac{p}{\rho} \tag{2.2}$$

where γ is the ratio of the specific heat coefficients. For the air in the standard conditions, the gas constant is $R = 287\mathrm{m}^2/(\mathrm{s}^2\mathrm{K})$ and $\gamma = 1.4$. In the present formulation, the equations of the motion are referred to an inertial system without apparent forces. Let Ω be the fluid domain with a boundary $\partial\Omega$, the

Navier Stokes equations express the fundamental principles of the balance of the mass, momentum and total energy in Ω. They are:

$$\frac{\partial}{\partial t}\int_{\Omega}\rho\, dV + \int_{\partial\Omega}\rho\,\underline{\mathbf{u}}\cdot\underline{n}\, dS = 0 \tag{2.3a}$$

$$\frac{\partial}{\partial t}\int_{\Omega}\rho\,\underline{\mathbf{u}}\, dV + \int_{\partial\Omega}\left(\rho\underline{\mathbf{u}}\,\underline{\mathbf{u}} + p\,\underline{\underline{\mathbf{I}}}\right)\cdot\,\underline{n}\, dS = \int_{\partial\Omega}\underline{\underline{\tau}}\cdot\,\underline{n}\, dS \tag{2.3b}$$

$$\frac{\partial}{\partial t}\int_{\Omega}\rho\, E\, dV + \int_{\partial\Omega}\left(\rho\, E\,\underline{\mathbf{u}} + \,p\,\underline{\mathbf{u}}\right)\,\cdot\,\underline{n}\, dS = \int_{\partial\Omega}\left(\underline{\underline{\tau}}\cdot\underline{\mathbf{u}}\, + \lambda\underline{\nabla}\, T\right)\cdot\,\underline{n}\, dS \tag{2.3c}$$

In equations (2.3), $\underline{\underline{\mathbf{I}}}$ is the unit tensor. The viscous stress tensor $\underline{\underline{\tau}}$ for Newtonian fluids is defined as:

$$\underline{\underline{\tau}} = \mu\left(\underline{\nabla}\,\underline{\mathbf{u}} + \underline{\nabla}\,\underline{\mathbf{u}}^{T} - \frac{2}{3}\,\underline{\underline{\mathbf{I}}}\,\underline{\nabla}\,\cdot\underline{\mathbf{u}}\right) \tag{2.4}$$

and $E = e + q^2/2$ is the total specific energy, with $q = |\underline{\mathbf{u}}|$. The dynamic viscosity μ and thermal conductivity λ of Fourier's law for heat transfer vary with the temperature according to Sutherland's laws:

$$\mu = C_1\frac{T^{1.5}}{T + C_2}$$
$$\lambda = C_3\frac{T^{1.5}}{T + C_4}$$

The constants C_i $(i = 1, 4)$ are reported in case of air.

$$C_1 = 1.458\cdot 10^{-6}\ \text{kg/(ms}\sqrt{\text{K}})$$
$$C_2 = 110.4\ \text{K}$$
$$C_3 = 2.495\cdot 10^{-3}\ \text{kg/(mK}^{1.5})$$
$$C_4 = 194\text{K}$$

A flow solution is obtained in a time interval $[t_0, t]$ when the velocity vector $\underline{\mathbf{u}}$, the flow density ρ and the thermodynamic magnitudes p, T and e are known in Ω $\forall t \in [t_0, t]$. The problem is completely defined by setting proper initial and boundary conditions on the state vector

$$\underline{\mathbf{U}} = (\ \rho,\ \rho\,\underline{\mathbf{u}},\ \rho E\ )^{T} \tag{2.5}$$

The existence and uniqueness of the solution of the system (2.3) is still not rigorously established. By means of the Gauss theorem, the integral balance equations (2.3) are transformed in the differential form as follows:

$$\frac{\partial \rho}{\partial t} + \underline{\nabla} \cdot \rho \underline{\mathbf{u}} = 0 \tag{2.6a}$$

$$\frac{\partial \rho \underline{\mathbf{u}}}{\partial t} + \underline{\mathbf{u}} \cdot \underline{\nabla} (\rho \underline{\mathbf{u}}) + \underline{\nabla} p = \underline{\nabla} \cdot \underline{\underline{\tau}} \tag{2.6b}$$

$$\frac{\partial \rho E}{\partial t} + \underline{\nabla} \cdot [(\rho E + p) \underline{\mathbf{u}}] = \underline{\nabla} \cdot \left(\underline{\underline{\tau}} \cdot \underline{\mathbf{u}} + \lambda \underline{\nabla} T \right) \tag{2.6c}$$

In some special cases, the inviscid flow models are also employed. Thus, the Euler equations are obtained from the Navier Stokes by setting $\mu = \lambda = 0$:

$$\frac{\partial \rho}{\partial t} + \underline{\nabla} \cdot \rho \underline{\mathbf{u}} = 0 \tag{2.7a}$$

$$\frac{\partial \rho \underline{\mathbf{u}}}{\partial t} + \underline{\mathbf{u}} \cdot \underline{\nabla} (\rho \underline{\mathbf{u}}) + \underline{\nabla} p = 0 \tag{2.7b}$$

$$\frac{\partial \rho E}{\partial t} + \underline{\nabla} \cdot [(\rho E + p) \underline{\mathbf{u}}] = 0 \tag{2.7c}$$

Furthermore, in the regimes in which the compressibility is negligible, the flow density can be regarded as a constant. The energy equation is no longer coupled with the momentum equation and the equations (2.6) take the following form:

$$\underline{\nabla} \cdot \underline{\mathbf{u}} = 0 \tag{2.8a}$$

$$\frac{\partial \underline{\mathbf{u}}}{\partial t} + \underline{\mathbf{u}} \cdot \underline{\nabla} \underline{\mathbf{u}} + \frac{1}{\rho} \underline{\nabla} p = \nu \nabla^2 \underline{\mathbf{u}} \tag{2.8b}$$

In equation (2.8b), $\nu = \mu / \rho$ is the kinematic viscosity. The set of equations (2.6), (2.7) and (2.8) have a different mathematical character. Proper initial and boundary conditions have to be established. For the applications of external aerodynamics, undisturbed flow conditions are assigned on the pressure and flow velocities on the surface at an infinite distance from the solid body. For viscous computations, (equations (2.6)), an adherence condition is assigned on three components of the velocity. For the Euler equations (2.7), an impermeability condition is specified for the wall normal flow velocity.

Finally, by defining a set of reference quantities (L_r, U_r, ρ_r, μ_r) the nondimensional form of the equations (2.6) are achieved:

$$\frac{\partial \rho}{\partial t} + \underline{\nabla} \cdot \rho \underline{\mathbf{u}} = 0 \tag{2.9a}$$

$$\frac{\partial \rho \underline{\mathbf{u}}}{\partial t} + \underline{\mathbf{u}} \cdot \underline{\nabla} (\rho \underline{\mathbf{u}}) + \underline{\nabla} p = \frac{1}{Re} \underline{\nabla} \cdot \underline{\underline{\tau}} \tag{2.9b}$$

$$\frac{\partial \rho E}{\partial t} + \underline{\nabla} \cdot [(\rho E + p) \underline{\mathbf{u}}] = \underline{\nabla} \cdot \left(\underline{\underline{\tau}} \cdot \underline{\mathbf{u}} \right) \frac{M^2}{Re} + \underline{\nabla} \cdot (\lambda T) \frac{1}{Re\, Pr} \tag{2.9c}$$

where the numbers of Reynolds, Mach and Prandtl are defined as follows:

$$Re = \frac{\rho_r U_r L_r}{\mu_r}$$

$$M = U_r \sqrt{\frac{\gamma \rho_r}{p_r}}$$

$$Pr = \frac{\mu_r c_p}{\lambda_r}$$

The Arbitrary Lagrangian Eulerian (ALE) formulation [57] is used to take into account the rigid motion of bodies in the fluid domain. The exposition is referred to the inviscid flow equations (2.7), being the viscous terms not affected by the rigid moving frame. In particular, by considering a moving control volume $\Omega(t)$, we have:

$$\frac{\partial}{\partial t} \int_{\Omega(t)} \rho \, dV + \int_{\partial\Omega(t)} \rho \, (\underline{\mathbf{u}} - \underline{\mathbf{u}}_s) \cdot \underline{n} \, dS = 0 \tag{2.10a}$$

$$\frac{\partial}{\partial t} \int_{\Omega(t)} \rho \, \underline{\mathbf{u}} \, dV + \int_{\partial\Omega(t)} \rho \, \underline{\mathbf{u}} \, (\underline{\mathbf{u}} - \underline{\mathbf{u}}_s) \cdot \underline{n} \, dS + \int_{\partial\Omega(t)} p \, \underline{n} \, dS = 0 \tag{2.10b}$$

$$\frac{\partial}{\partial t} \int_{\Omega(t)} \rho E \, dV + \int_{\partial\Omega(t)} \rho \, E \, (\underline{\mathbf{u}} - \underline{\mathbf{u}}_s) \cdot \underline{n} \, dS + \int_{\partial\Omega(t)} p \, \underline{\mathbf{u}} \cdot \underline{n} dS = 0 \tag{2.10c}$$

where $\underline{\mathbf{u}}_s$ is the velocity of the points on $\partial\Omega(t)$. In the hypothesis of rigid displacements, the measurement of volume $\Omega(t)$ does not change in time, and the velocities $\underline{\mathbf{u}}_s$ and $\underline{\mathbf{u}}_o$ of two points $\underline{S}$ and $\underline{O}$ of $\partial\Omega$ are related by:

$$\underline{\mathbf{u}}_s = \underline{\mathbf{u}}_o + \underline{\dot{\Theta}} \times (\underline{S} - \underline{O}) \tag{2.11}$$

where $\underline{\dot{\Theta}}$ is the angular velocity of the rigid motion of Ω. The effectiveness of this approach has been verified by simulating several basic flow test cases of moving solid bodies (Marongiu et al. [58]).

2.2 RANS equations

The Navier Stokes equations are able to resolve the flows in both laminar and turbulent regimes. However, the Direct Numerical Solution (DNS) of the equations (2.6) and (2.8), in case of turbulent flows, requires so high time and spatial resolutions that they become no longer applicable to Reynolds numbers greater than 10^4 (based on the scale length of the problem, [59]). For high Reynolds and turbulent flow simulations, other set of equations are employed. By introducing the Reynolds decomposition, the instantaneous velocity is given by the sum of two terms:

$$\underline{\mathbf{u}} = \langle\, \underline{\mathbf{u}} \,\rangle + \underline{\mathbf{u}}' \tag{2.12}$$

where $\langle\, \underline{\mathbf{u}} \,\rangle$ is the mean velocity and $\underline{\mathbf{u}}'$ is the fluctuation. In a turbulent flow, the mean velocity can be estimated in several ways ([59]). Let $\underline{\mathbf{u}}$ be the instantaneous velocity, for statistically stationary flows, the time average over an interval T is defined as:

$$\langle\, \underline{\mathbf{u}} \,\rangle_T \equiv \frac{1}{T} \int_t^{t+T} \underline{\mathbf{u}}\, dt \tag{2.13}$$

For flows that have a defined periodicity T, the ensemble average is introduced as:

$$\langle\, \underline{\mathbf{u}} \,\rangle_N \equiv \frac{1}{N} \sum_{n=1}^{N} \underline{\mathbf{u}}(t + NT) \tag{2.14}$$

where N is the number of realizations. The spatial average for a cubic domain $\Omega = L^3$ is defined in the cases of homogeneous turbulence as:

$$\langle\, \underline{\mathbf{u}} \,\rangle_L \equiv \frac{1}{L^3} \int_\Omega \underline{\mathbf{u}}\, dV \tag{2.15}$$

The averages (2.13), (2.14) and (2.15) are approximated ways to define the exact mean, which is given once that the probality density function $f(V)$ of

$\underline{\mathbf{u}}$ is known:

$$\langle\, \underline{\mathbf{u}} \,\rangle \equiv \int_{-\infty}^{+\infty} V\, f(V)\, dV \tag{2.16}$$

For statistically stationary flows it results that $\langle\, \underline{\mathbf{u}} \,\rangle_T \to \langle\, \underline{\mathbf{u}} \,\rangle$ for $T \to \infty$. The Reynolds Averaged Navier Stokes (RANS) equations are obtained by exploting the definition (2.12). The incompressible form (2.8) is used for these scopes. We have:

$$\underline{\nabla} \cdot \langle\, \underline{\mathbf{u}} \,\rangle = 0 \tag{2.17a}$$

$$\frac{\partial \langle\, \underline{\mathbf{u}} \,\rangle}{\partial t} + \langle\, \underline{\mathbf{u}} \,\rangle \cdot \underline{\nabla} \langle\, \underline{\mathbf{u}} \,\rangle + \frac{1}{\rho} \underline{\nabla} \langle\, p \,\rangle = \nu \nabla^2 \langle\, \underline{\mathbf{u}} \,\rangle + \frac{1}{\rho} \underline{\nabla} \cdot \underline{\underline{\tau}}^t \tag{2.17b}$$

The mean velocity $\langle\, \underline{\mathbf{u}} \,\rangle$ is governed by the same set of equations except for the presence of the Reynolds stress tensor $\underline{\underline{\tau}}^t = -\rho \langle\, \underline{\mathbf{u}}' \, \underline{\mathbf{u}}' \,\rangle$. Due to the symmetry of $\underline{\underline{\tau}}^t$, six new unknowns are introduced. The turbulent viscosity hypothesis of Boussinesq assumes that the deviatoric part of the Reynolds stress is proportional to the velocity gradient. Namely:

$$\underline{\underline{\tau}}^t = \mu_t \left(\underline{\nabla} \langle\, \underline{\mathbf{u}} \,\rangle + \underline{\nabla} \langle\, \underline{\mathbf{u}} \,\rangle^T \right) - \frac{2}{3} \kappa \underline{\underline{\mathbf{I}}}\, \rho \tag{2.18}$$

where $\kappa = \langle\, \underline{\mathbf{u}}' \cdot \underline{\mathbf{u}}' \,\rangle / 2$ is the turbulent kinetic energy. The scalar coefficient $\mu_t = \mu_t(\underline{\mathbf{x}}, t)$ is called eddy viscosity. The closure problem is now reduced to two unknowns. The turbulence modelling tries to establish one or more relations among μ_t, κ and the mean velocity $\langle\, \underline{\mathbf{u}} \,\rangle$.

2.2.1 The closure models

A large variety of models are used in the CFD solvers, from the simplest algebraic relations to one and two differential equations [60]. The $\kappa - \omega$ models are the class of turbulence models in which the eddy viscosity μ_t is computed as:

$$\mu_t = \frac{\rho\, \kappa}{\omega} \tag{2.19}$$

where $\omega \propto \varepsilon / \kappa$ and ε is the dissipation rate at which the turbulent kinetic energy is converted into thermal internal energy. The standard $\kappa - \omega$ model

of Wilcox [61] is constituted by the following two equations:

$$\frac{\partial \rho\, \kappa}{\partial t} + \underline{\nabla} \cdot (\rho\, \kappa\, \underline{\mathbf{u}}) = \rho(P_k - \omega\beta^*\kappa) + \underline{\nabla} \cdot [\mu + \ \mu_t\, \sigma_k\, \underline{\nabla}\, \kappa] \qquad (2.20a)$$

$$\frac{\partial \rho\, \omega}{\partial t} + \underline{\nabla} \cdot (\rho\, \omega\, \underline{\mathbf{u}}) = \rho(P_\omega - \omega\beta\omega^2) + \underline{\nabla} \cdot [\mu + \mu_t\, \sigma_\omega\, \underline{\nabla}\, \omega] \qquad (2.20b)$$

where

$$P_k = \tau_{ij} \frac{u_i}{x_j}$$

and

$$P_\omega = \gamma_\omega \frac{\omega}{\kappa} \tau_{ij} \frac{u_i}{x_j}$$

The constants of the Wilcox $\kappa - \omega$ model are reported:

$$\beta^* = 0.09, \ \ \sigma_k = 0.5, \ \ \beta = 0.075, \ \ \sigma_\omega = 0.5;$$

$$\gamma_\omega = \frac{\beta}{\beta^*} - \frac{\sigma_\omega\, \kappa_a^2}{\sqrt{\beta^*}}$$

$$\kappa_a^2 = \frac{\sqrt{\beta^*}\left(\frac{\beta}{\beta^*} - \gamma_\omega\right)}{\sigma_\omega}$$

2.2.2 The TNT model of Kok

Kok [62] provided a modification of the original $\kappa - \omega$ model of Wilcox. The Turbulent Non Turbulent (TNT) $\kappa - \omega$ model modifies the $\kappa - \omega$ equation (2.20b) by introducing a cross diffusion term C_D as follows:

$$\frac{\partial \rho\, \omega}{\partial t} + \underline{\nabla} \cdot (\rho\, \omega\, \underline{\mathbf{u}}) = \rho(P_\omega - \omega\beta\omega^2) + \underline{\nabla} \cdot [\mu + \mu_t\, \sigma_\omega\, \underline{\nabla}\, \omega] + C_D \qquad (2.21)$$

where

$$C_D = \sigma_d \frac{\sigma_d}{\omega} Max \left[\frac{\partial \kappa}{\partial x_j} \frac{\partial \omega}{\partial x_j}, 0 \right] \qquad (2.22)$$

The constants of the TNT $\kappa - \omega$ model are:

$$\beta^* = 0.09, \ \ \sigma_k = \frac{2}{3}, \ \ \beta = 0.075, \ \ \sigma_\omega = 0.5, \ \ \sigma_d = 0.5$$

2.2.3 SST model of Menter

A further development of the $\kappa-\omega$ models is represented by the Shear Stress Transport (SST) model of Menter [63]. In this model the cross diffusion term C_D is modified as follows:

$$C_D = 2(1 - F_1)\rho\,\sigma_{\omega_2}\frac{1}{\omega}\frac{\partial\kappa}{\partial x_j}\frac{\partial\omega}{\partial x_j} \tag{2.23}$$

where each constant is calculated by using the blending function:

$$\phi = F_1\,\phi_1 + (1 - F_1)\phi_2 \tag{2.24}$$

The values of the constants for the inner zone are:

$$\sigma_{\kappa_1} = 0.85;\;\; \sigma_{\omega_1} = 0.50;\;\; \beta_1 = 0.075;$$

For the outer zone:

$$\sigma_{\kappa_2} = 1.0;\;\; \sigma_{\omega_2} = 0.856;\;\; \beta_2 = 0.0828;$$

and

$$\beta^* = 0.09;\;\; \gamma_{\omega_{1,2}} = \frac{\beta_{1,2}}{\beta^*} - \frac{\sigma_{\omega_{1,2}}\,\kappa_a^2}{\sqrt{\beta^*}}$$

The blending function F_1 is computed as:

$$F_1 = \tanh arg_1^4 \tag{2.25}$$

where

$$arg_1 = Min\left[max\left(\frac{\sqrt{\kappa}}{0.09\,\omega\,y}, \frac{500\nu}{\omega\,y^2}\right), \frac{4\rho\sigma\nu\omega_2}{C_D y^2}\right] \tag{2.26}$$

and

$$C_D = Max\left[2\rho\sigma_{\omega_2}\frac{1}{\omega}\frac{\partial\kappa}{\partial x_j}\frac{\partial\omega}{\partial x_j}, 10^{-20}\right] \tag{2.27}$$

In the SST model the eddy viscosity is computed as:

$$\mu_t = \rho\frac{a_1\,\kappa}{Max(a_1\Omega, \Omega F_2)} \tag{2.28}$$

with $a = 0.31$. The second blending function F_2 is:

$$F_1 = \tanh arg_1^2 \tag{2.29}$$

$$arg_2 = Max\left[2\frac{\sqrt{\kappa}}{0.09\,\omega\,y}, \frac{500\nu}{\omega\,y^2}\right] \tag{2.30}$$

2.3 The numerical method

2.3.1 ZEN Code

The flow solver used in the present thesis is ZEN, a multi-block code widely used and tested for the analysis of complex configurations in the subsonic, transonic, and supersonic regimes (Catalano & Amato [64]). The equations are discretized by means of a standard cell-centered finite volume scheme with blended self adaptive second and fourth order artificial dissipation. The turbulence equations are weakly coupled with the RANS equations and solved only on the finest grid level of a multi-grid cycle. Algebraic, one-equation, two-equations, and non linear eddy viscosity turbulence models are available. In the following, some details about the time integration scheme are given.

The residual form

By indicating with u, v, w the cartesian components of the velocity $\underline{\mathbf{u}}$ the vector form of the Navier Stokes equations (2.3) is given by:

$$\frac{\partial}{\partial t}\int_{\Omega}\underline{\mathbf{U}} + \int_{\partial\Omega}\underline{\mathbf{F}}\ \cdot\underline{n}\ dS = 0 \tag{2.31}$$

where $\underline{\mathbf{F}} = \underline{\mathbf{F}}_c - \underline{\mathbf{F}}_v$ is the flux vector composed of the convective and viscous contributions:

$$\underline{\mathbf{F}}_c = \begin{pmatrix} \rho\underline{\mathbf{u}} \\ \rho\underline{\mathbf{u}}\,\underline{\mathbf{u}} + p\underline{\underline{\mathbf{I}}} \\ \rho\underline{\mathbf{u}}H \end{pmatrix} \tag{2.32}$$

$$\underline{\mathbf{F}}_v = \begin{pmatrix} 0 \\ \underline{\underline{\tau}} \\ -\underline{q} + \underline{\mathbf{u}}\cdot\underline{\underline{\tau}} \end{pmatrix} \tag{2.33}$$

where $H = E + p\rho^{-1}$ is the total specific enthalpy. The finite volume approach exploits the semi-discretized form of the equation (2.31) by subdividing the volume Ω into a set of elementary volumes $V_{i,j,k}$ delimited by the surfaces $S_{i,j,k}$. The balance equation (2.31) in $V_{i,j,k}$ between two time

instants t^n and t^{n+1} is:

$$\int_{V_{ijk}} \underline{\mathbf{U}}\,(\underline{\mathbf{x}}, t^{n+1})dV - \int_{V_{ijk}} \underline{\mathbf{U}}\,(\underline{\mathbf{x}}, t^{n})dV + \quad \int_{t^n}^{t^{n+1}} \left[\int_{S_{ijk}} \underline{\mathbf{F}}\,(\underline{\mathbf{x}}, t) \cdot \underline{n} dS \right] dt = 0 \tag{2.34}$$

By defining the averages over the volume V_{ijk}:

$$\underline{\mathbf{U}}^n = \frac{1}{V_{ijk}} \int_{V_{ijk}} \underline{\mathbf{U}}\,(\underline{\mathbf{x}}, t^n)dV \tag{2.35}$$

$$\underline{\mathbf{U}}^{n+1} = \frac{1}{V_{ijk}} \int_{V_{ijk}} \underline{\mathbf{U}}\,(\underline{\mathbf{x}}, t^{n+1})dV \tag{2.36}$$

and the averaged residual between t^n and t^{n+1}:

$$\underline{\mathbf{R}}^{n,n+1} = \frac{1}{\Delta t} \quad \int_{t^n}^{t^{n+1}} \left[\int_{S_{ijk}} \underline{\mathbf{F}}\,(\underline{\mathbf{x}}, t) \cdot \underline{n} dS \right] dt \tag{2.37}$$

the balance equation (2.34) becomes:

$$\frac{1}{\Delta t}(\underline{\mathbf{U}}^{n+1} - \underline{\mathbf{U}}^{n}) + \frac{1}{V_{ijk}} \underline{\mathbf{R}}^{n,n+1} = 0 \tag{2.38}$$

The limit of the equation (2.38) for $t^{n+1} \to t^n$ provides the residual form of the Navier Stokes equations:

$$V_{ijk} \frac{\partial \underline{\mathbf{U}}}{\partial t} + \underline{\mathbf{R}} = 0 \tag{2.39}$$

In case of steady flows, the equation (2.39) reduces to:

$$\underline{\mathbf{R}} = 0 \tag{2.40}$$

The residuals $\underline{\mathbf{R}}$ are obtained as the difference of the fluxes on the six faces of each cell. The same fluxes are evaluated by averaging the values at the centers of the cells.

The integration in case of steady flows

The equation (2.39) is evaluated throughout the multi-stage Runge Kutta scheme (Jameson, [65]). Let q the number of stages, and m the index of the single stage, the step of the Runge Kutta is:

$$\underline{\mathbf{U}}^{n+\frac{m}{q}} = \underline{\mathbf{U}}^n - \alpha_m \frac{\triangle t}{V_{ijk}} \underline{\mathbf{R}}^{n+\frac{m-1}{q}} \tag{2.41}$$

where the coefficients α_m depend on the number of stages q and are determined on the basis of accuracy requirements. For the steady computations several techniques are introduced to accelerate the convergence rate.

The time integration for unsteady solutions

The Dual Time Stepping (DTS) method is used for the unsteady computations (Jameson, [66]). The flow solution at each time step is obtained by reformulating the problem as a steady one; the steady state solution is computed by integrating over an unphysical parameter called dual time. Starting from the semidiscrete equation (2.39), the time derivative is computed by a second order accuarate formula:

$$\frac{3\underline{\mathbf{U}}^{n+1} - 4\underline{\mathbf{U}}^{n} - \underline{\mathbf{U}}^{n-1}}{2\triangle t} = -\frac{1}{V_{ijk}}\underline{\mathbf{R}}^{n+1} \tag{2.42}$$

By indicating with k the dual iteration index and with n the current time level, the DTS method modifies the residual as follows:

$$\underline{\mathbf{R}}^{\star} = \underline{\mathbf{R}}^{k} + V_{ijk}\frac{3\underline{\mathbf{U}}^{k} - 4\underline{\mathbf{U}}^{n} - \underline{\mathbf{U}}^{n-1}}{2\triangle t} \tag{2.43}$$

The new residual $\underline{\mathbf{R}}^{\star}$ is such that

$$\lim_{k\to\infty} \underline{\mathbf{R}}^{\star} = 0 \tag{2.44}$$

As a consequence, the solution at each time step of the equation

$$\underline{\mathbf{R}}^{\star} = 0 \tag{2.45}$$

provides the unknown $\underline{\mathbf{U}}^{n+1}$. It is worth noting that the equation (2.45) is formally analogous to the equation (2.40) used for the steady state formulations. Thus, by introducing a pseudo time derivative of the state variable

$$\frac{\partial \underline{\mathbf{U}}}{\partial \tau} = -\frac{1}{V_{ijk}}\underline{\mathbf{R}}^{\star} \tag{2.46}$$

the equation (2.46) can be treated by using the same numerical techniques adopted for the steady solvers. In ZEN, the unsteady procedure has been verified on several test cases (Marongiu et al. [67, 68]).

Chapter 3

Unsteady aerodynamics of ideal flows

The hypothesis of inviscid and incompressible fluid represents a strong idealization with respect to a real flow case. However, several and useful results are obtained under these hypotheses. The basic mechanisms that generate the unsteady aerodynamic force on the oscillating airfoils are identified and discussed. An analytical solution for thin oscillating airfoils found by Theodorsen is demonstrated and applied. The results presented in the chapter are collected from some classical text-books on Fluid Mechanics ([69], [70], [71]).

3.1 Basic concepts

In case of an inviscid and incompressible flow, the velocity $\underline{\mathbf{u}}$ and pressure p are determined by means of the Euler equations (2.7). By applying the curl operator to the momentum equation (2.7b), and using the following vector identity,

$$\underline{\mathbf{u}} \cdot \underline{\nabla}\, \underline{\mathbf{u}} = \frac{1}{2} \underline{\nabla} \left| \underline{\mathbf{u}} \right|^2 - \underline{\mathbf{u}} \times \underline{\omega} \tag{3.1}$$

where $\underline{\omega} = \underline{\nabla} \times \underline{\mathbf{u}}$ is the vorticity, the Helmholtz equation is achieved:

$$\frac{\partial \underline{\omega}}{\partial t} + \underline{\nabla} \times \underline{\omega} \times \underline{\mathbf{u}} = 0 \tag{3.2}$$

The vector $\underline{\boldsymbol{l}} = \underline{\omega} \times \underline{\mathbf{u}}$ is called Lamb vector. The flows in which the vorticity and velocity vectors are parallel are said *Beltrami flows*. If $\underline{\mathbf{u}} \cdot \underline{\omega} = 0$ with

$\underline{\omega} \neq 0$, the flows are said *complex lamellar flows*. A particular case of complex lamellar flow is any two dimensional flow. The flow is irrotational when the vorticity $\underline{\omega}$ is zero in any connected region. For an irrotational flow, the velocity potential is defined as:

$$\underline{\mathbf{u}} = \underline{\nabla}\,\phi \tag{3.3}$$

By exploiting equation (3.3), the continuity equation transforms to Laplace's equation:

$$\nabla^2\phi = 0. \tag{3.4}$$

The momentum equation (2.7b) is cast as:

$$\frac{\partial}{\partial t}\,\underline{\nabla}\,\phi + \frac{1}{2}\underline{\nabla}\,|\underline{\mathbf{u}}|^2 = -\,\underline{\nabla}\,p \tag{3.5}$$

By moving any term under the gradient sign, one obtains that:

$$\underline{\nabla}\left(\frac{\partial\phi}{\partial t} + \frac{1}{2}\underline{\nabla}\,|\underline{\mathbf{u}}|^2 + p\right) = 0. \tag{3.6}$$

Namely, Bernoulli's equation for unsteady irrotational flows is achieved:

$$\frac{\partial\phi}{\partial t} + \frac{1}{2}\underline{\nabla}\,|\underline{\mathbf{u}}|^2 + p = F(t) \tag{3.7}$$

where $F(t)$ is an arbitrary function of the time that can be included in the definition of ϕ without altering the velocity $\underline{\mathbf{u}}$. The equations (3.4) and (3.7) describe the unsteady motion of an incompressible irrotational flow. In such a case, the problem is defined by specifying an opportune set of boundary conditions for the potential function ϕ.

3.2 Aerodynamic force for an inviscid flow

The aerodynamic force, exerted by an inviscid flow on a solid body B, is determined by integrating the pressure along the body surface ∂B:

$$\underline{\mathbf{F}} = \int_{\partial B} p\,\underline{n}\,dS \tag{3.8}$$

In the definition (3.8), $\underline{n}$ is the wall normal versor pointing outward of the fluid domain. There are several and fundamental mechanisms concurring in the determination of the force $\underline{\mathbf{F}}$. In the case of inviscid and incompressible flows, they may be related to the kinematic properties of the vorticity distributions. In the following, some basic concepts are recalled.

3.2.1 Virtual or apparent mass

In case of flow around a moving solid body B without circulation, the aerodynamic force is related to the *virtual* or *apparent mass* contribution, which is defined as (see Saffman [71]):

$$\underline{\mathbf{I}}_B = \int_{\partial B} \phi \, \underline{n} \, dS \tag{3.9}$$

where ϕ is the velocity potential function of the flow field. It is possible to show that the relation between the aerodynamic force and the *virtual* mass is:

$$\underline{\mathbf{F}} = -\frac{d}{dt}\underline{\mathbf{I}}_B \tag{3.10}$$

In fact, by using the definition (3.9), the time derivative of $\underline{\mathbf{I}}_B$ is calculated:

$$\frac{d}{dt}\underline{\mathbf{I}}_B = \frac{d}{dt}\int_{\partial B} \phi \, \underline{n} dS = \int_{\partial B} \frac{\partial \phi}{\partial t} \, \underline{n} \, dS + \int_{\partial B} (\underline{\mathbf{u}} \cdot \underline{\nabla} \, \phi) \, \underline{n} \, dS \tag{3.11}$$

By using the unsteady Bernoulli equation (3.7), we have:

$$\frac{d}{dt}\underline{\mathbf{I}}_B = -\int_{\partial B} (\frac{1}{2}\underline{\nabla} \, |\underline{\mathbf{u}}|^2 + p) \, \underline{n} \, dS + \int_{\partial B} \underline{\mathbf{u}} \cdot \underline{n} \, \underline{\nabla} \, \phi \, dS \tag{3.12}$$

The aerodynamic force contribution is recognized by using the definition in equation (3.8):

$$\frac{d}{dt}\underline{\mathbf{I}}_B = -\underline{\mathbf{F}} - \int_{\partial B} \left(\frac{1}{2}|\underline{\mathbf{u}}|^2 \, \underline{n} \, - (\underline{\mathbf{u}} \cdot \underline{n}) \, \underline{\mathbf{u}} \right) dS \tag{3.13}$$

The surface integral on ∂B can be replaced by any surface integral enclosing B provided that there is no vorticity in the field. For an unlimited flow domain, the surface integral vanishes and the equation (3.10) is obtained.

The significance of $\underline{\mathbf{I}}_B$ is evident. In fact, if $M\underline{\mathbf{U}}$ is the momentum of the solid body and $\underline{\mathbf{f}}$ the resultant of the external forces applied on the solid body, Newton's second law is:

$$\frac{d}{dt}M\underline{\mathbf{U}} = \underline{\mathbf{F}} + \underline{\mathbf{f}} \tag{3.14}$$

By exploiting the equation (3.10), we have:

$$\frac{d}{dt}(M\underline{\mathbf{U}} + \underline{\mathbf{I}}_B) = \underline{\mathbf{f}} \tag{3.15}$$

The presence of the *virtual mass* $\underline{\mathbf{I}}_B$ alters the solid body inertia. The term $\underline{\mathbf{I}}_B$ accounts for the effects of the fluid surrounding B. The external force $\underline{\mathbf{f}}$ applied on B is balanced by the real mass of the body and by the virtual mass of the fluid. It is worth noting that such effects appear only in case of unsteady equilibrium. This kind of contribution is associated with any solid body moving with acceleration. If the B is steady, this effect does not appear.

3.2.2 Vortex force

The presence of vorticity in the field, even if the flow is inviscid, changes completely the scenario in which the aerodynamic force interacts. By supposing a steady moving body B, the lift is produced when a non zero circulation of the velocity around a circuit surrounding B occurs. In this regard, the concept of *vortex force* is introduced (Prandtl 1918 and von Karman and Burgers [5]). The *vortex force* of a vorticity distribution in Ω is defined as (Saffman [71]):

$$\underline{\mathbf{F}}_V = -\int_\Omega \underline{\mathbf{u}} \times \underline{\omega}\, dV = -\int_\Omega \underline{\boldsymbol{l}}\, dV \tag{3.16}$$

By inserting the relation (3.1) in equation (3.16), we have:

$$\underline{\mathbf{F}}_V = \int_\Omega (\, \frac{1}{2}\underline{\nabla}\, |\underline{\mathbf{u}}|^2 - \underline{\mathbf{u}} \cdot \underline{\nabla}\, \underline{\mathbf{u}}\,)dV \tag{3.17}$$

and by using the Gauss theorem:

$$\underline{\mathbf{F}}_V = \int_\Omega (\, \frac{1}{2}\underline{\nabla}\, |\underline{\mathbf{u}}|^2 - \underline{\mathbf{u}} \cdot \underline{\nabla}\, \underline{\mathbf{u}}\,)dV = \int_{\partial\Omega} (\, \frac{1}{2}\, |\underline{\mathbf{u}}|^2\, \underline{n} - \underline{\mathbf{u}}\, \underline{\mathbf{u}} \cdot \underline{n})dS \tag{3.18}$$

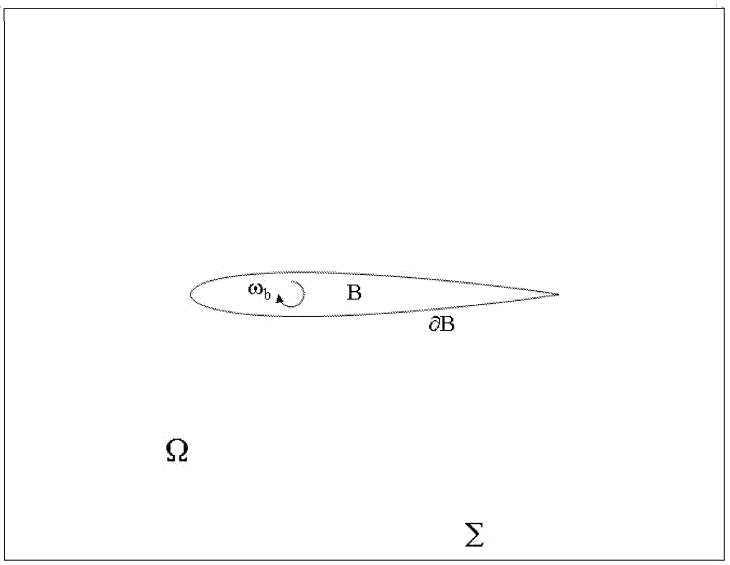

Figure 3.1: Scheme of the *bound* vorticity for an inviscid flow field.

By supposing that Ω contains the solid body B, as indicated in the scheme (3.1), it is possible to show that the aerodynamic force is equivalent to the vortex force in B. In fact, by indicating with Σ the external surface surrouding B, the momentum equation provides:

$$\underline{\mathbf{F}} = \int_{\partial B} p\, \underline{n}\, dS = -\int_{\Sigma} p\, \underline{n}\, ds - \int_{\Sigma} \underline{\mathbf{u}}\, \underline{\mathbf{u}} \cdot \underline{n}\, dS \tag{3.19}$$

By adding and subtracting the vector $|\underline{\mathbf{u}}|^2/2\, \underline{n}$ in equation (3.19), we have:

$$\underline{\mathbf{F}} = -\int_{\Sigma} (\, p + \frac{1}{2}|\underline{\mathbf{u}}|^2)\, \underline{n}\, ds + \int_{\Sigma} (\frac{1}{2}|\underline{\mathbf{u}}|^2\, \underline{\underline{\mathbf{I}}} - \underline{\mathbf{u}}\, \underline{\mathbf{u}}\,) \cdot \underline{n}\, dS \tag{3.20}$$

If the surface Σ is far enough that the total head $(p + |\underline{\mathbf{u}}|^2/2)$ is constant, equation (3.20) reduces:

$$\underline{\mathbf{F}} = \int_{\Sigma} (\frac{1}{2}|\underline{\mathbf{u}}|^2\, \underline{\underline{\mathbf{I}}} - \underline{\mathbf{u}}\, \underline{\mathbf{u}}\,) \cdot \underline{n}\, dS \tag{3.21}$$

Recalling equation (3.17), we have

$$\underline{\mathbf{F}} = -\int_{\Omega \cup B} \underline{\mathbf{u}} \times \underline{\omega}\, dV \tag{3.22}$$

Since the flow is irrotational in Ω,

$$\underline{\mathbf{F}} = -\int_{B} \underline{\mathbf{u}} \times \underline{\omega}\, dV = \underline{\mathbf{F}}_V \tag{3.23}$$

The last equality confirms the concept that in a steady and inviscid case, the aerodynamic force can be modelled as a *bound* vorticity distribution inside the solid volume B. Thus, any time variation of the flow topology (i.e. the angle of attack of an airfoil) produces a time change of the circulation that must be compensated by an equivalent release of vorticity. This last one is called *free* vorticity. In the unsteady cases, the *bound* and *free* vorticity have to be in equilibrium in such a way to fulfill the conservation of the total circulation.

3.2.3 Hydrodynamic impulse

Further relations are obtained by considering the application of impulsive forces on a vorticity distribution. For these purposes, it is useful to introduce the *hydrodynamic impulse*, as

$$\underline{\mathbf{I}} = \int_{\Omega} \underline{\mathbf{r}} \times \underline{\omega}\, dV \tag{3.24}$$

The time derivative of $\underline{\mathbf{I}}$ provides:

$$\frac{d\,\underline{\mathbf{I}}}{dt} = \int_{\Omega} \underline{\mathbf{r}} \times \frac{\partial \underline{\omega}}{\partial t}\, dV \tag{3.25}$$

In absence of solid bodies and external forces, the impulse is time invariance, i.e.:

$$\frac{d\,\underline{\mathbf{I}}}{dt} = 0 \tag{3.26}$$

When the flow motion is generated from an impulsive force of kind $\underline{\mathbf{f}} = \underline{\mathbf{i}}\ \delta(t - t_0)$, where $\delta(t - t_0)$ is the Dirac function, the impulse is no longer a

time invariant and further relations must be established. In such a case, since the time interval is small, the convection terms in the momentum equation are negligible, and an expansion in time is applicable for the velocity and pressure as follows:

$$\underline{\mathbf{u}}(\underline{\mathbf{x}},t) = \underline{\mathbf{u}}(\underline{\mathbf{x}})H(t-t_0) + \underline{\mathbf{u}}^1 H^1(t-t_0) \tag{3.27}$$

$$p(\underline{\mathbf{x}},t) = P(\underline{\mathbf{x}})\delta(t-t_0) + p^1 H^1(t-t_0) \tag{3.28}$$

where H is the Heaviside function ($H' = \delta$) and $P(\underline{\mathbf{x}})$ is usually called impulsive pressure. In such a case, the momentum equation provides:

$$\underline{\mathbf{u}}(\underline{\mathbf{x}})\,\delta(t-t_0) + \underline{\nabla}\,P\,\delta(t-t_0) = \underline{\mathbf{i}}\,\delta(t-t_0) \tag{3.29}$$

Namely,

$$\underline{\mathbf{u}}(\underline{\mathbf{x}}) + \underline{\nabla}\,P\ = \underline{\mathbf{i}} \tag{3.30}$$

The curl of (3.30) yields the following relation:

$$\underline{\omega} = \underline{\nabla} \times \underline{\mathbf{i}} \tag{3.31}$$

The application of the impulsive external force $\underline{\mathbf{f}}$ produces a vorticity governed by the equation (3.31). The volume integral of $\underline{\mathbf{i}}$ can be cast as follows:

$$\int_\Omega \underline{\mathbf{i}}\,dV = \int_\Omega \underline{\mathbf{r}} \times \underline{\nabla} \times \underline{\mathbf{i}}\,dV - \int_{\partial\Omega} \underline{\mathbf{r}} \times \underline{n} \times \underline{\mathbf{i}}\,dS \tag{3.32}$$

Since the surface integral vanishes for an unbounded domain, the volume integral of $\underline{\mathbf{i}}$ reduces to:

$$\int_\Omega \underline{\mathbf{i}}\,dV = \int_\Omega \underline{\mathbf{r}} \times \underline{\nabla} \times \underline{\mathbf{i}}\,dV = \int_\Omega \underline{\mathbf{r}} \times \underline{\omega}\,dV \tag{3.33}$$

where the last equality has been obtained by using equation (3.31). But, in equation (3.33) the definition of the hydrodynamic impulse (3.24) is recognizable. Thus, by integrating in time the equation (3.33), we obtain that:

$$\frac{d\,\underline{\mathbf{I}}}{dt} = \int_\Omega \underline{\mathbf{f}}\,dV \tag{3.34}$$

The relation (3.34) establishes a link between an impulsive external force and the time variation of the hydrodynamic impulse.

By collecting the results exposed so far, the aerodynamic force around a moving body B can be expressed by the sum of three contributions:

$$\underline{\mathbf{F}} = -\frac{d}{dt}\underline{\mathbf{I}}_B - \int_{\Omega \cup B} \underline{\boldsymbol{l}}\, dV - \left(\frac{d\,\underline{\mathbf{I}}}{dt}\right)_{\Omega \cup B} \tag{3.35}$$

The hypotheses of incompressible and inviscid flow contained in an unbounded domain (i.e. the external surface Σ does not intersect any vortical region) underlie the equation (3.35).

3.3 Thin oscillating airfoils

In 1935 Theodorsen [55] obtained the unsteady flow solution for a thin oscillating airfoil. The hypotheses of this solution are:

- incompressible and inviscid flow
- thin airfoils
- small and harmonic oscillations

Theodorsen's solution represents an example in which the mechanisms illustrated in the previous sections occur simultaneously. The demonstration of this problem can be found in the text of Bisplinghoff [72] as well. In the following, the main steps of this proof are reported.

By supposing the free stream velocity parallel to the x axis, the hypothesis of thin airfoil is expressed in terms of velocity components as:

$$u = U_\infty + u' \tag{3.36}$$

$$u', w \ll U_\infty \tag{3.37}$$

Besides, by introducing the potential perturbation ϕ', we have:

$$\frac{\partial \phi'}{\partial x} = u', \quad \frac{\partial \phi'}{\partial z} = w$$

The potential perturbation satisfies the equation of Laplace:

$$\nabla^2 \phi' = 0 \tag{3.38}$$

The linearized Bernoulli equation is also written as

$$p - p_\infty = -\rho U_\infty u' - \rho \frac{\partial \phi'}{\partial t} \tag{3.39}$$

The problem is defined by setting the initial and boundary conditions. On the solid body, the unsteady component of the velocity is associated with the body motion. In the hypotheses of small displacements, it can be expressed as:

$$w = \frac{\partial z_a}{\partial t} + U_\infty \frac{\partial z_a}{\partial x} = w_a(x,t) \tag{3.40}$$

Theodorsen obtains the aerodynamic force as sum of two contributions: the first is the *non circulatory* force determined by a distribution of sources and sinks along the airfoil surface; the second is the *circulatory* force created by means of the *bound* and *free* vorticity distributions.

3.3.1 Non circulatory contribution

The proof of Theodorsen's solution is achieved by transforming the flat plate from the physical plane xz in a circle in the complex plane XZ. The properties of such transformation are illustrated.

The conformal transformation

Let $c = 2b$ be the chord of the profile. The following transformation is introduced from the physical plane xz to the complex plane XZ:

$$x + i\, z = X + i\, Z + \frac{b^2}{4(X + i\, Z)} \tag{3.41}$$

where $i = \sqrt{-1}$ is the imaginary unit. The relation (3.41) transforms the profile of length c to a circle of radius $r = b/2$ (see figure 3.2). In fact, by putting $X = r\cos\theta$ and $Z = r\sin\theta$, the equation (3.41) provides:

$$x + i\, z = r\, e^{i\theta} + \frac{b^2}{4re^{i\theta}} = 2r\cos\theta \tag{3.42}$$

The velocity between the planes xz and XZ is subjected to the following relation:

$$\frac{d(x+i\,z)}{d(X+i\,Z)} = 1 - \frac{b^2}{4(X+i\,Z)^2} \tag{3.43}$$

The equation (3.43), evaluated on the circumference points, gives the components of the velocity. In the plane XZ, these components are indicated with q_X and q_Z. By calculating q_X and q_Z at $r = b/2$, we have:

$$\begin{aligned} u' - i\,w &= \frac{q_X - i\,q_Z}{2\sin\theta}\, e^{\,i\,(\theta-\pi/2)} \\ &= \frac{1}{2\sin\theta}\left[q_X\, e^{\,i\,(\theta-\pi/2)} + q_Z\, e^{\,i\,(\theta-\pi)}\right] \end{aligned} \tag{3.44}$$

Since, $e^{\,i\,(\theta-\pi/2)} = \sin\theta - i\,\cos\theta$, and $e^{\,i\,(\theta-\pi)} = -\cos\theta - i\,\sin\theta$, the equation (3.44) provides:

$$u' - i\,w = \frac{1}{2\sin\theta}\left[q_X\sin\theta - q_Z\cos\theta - i\,(q_X\cos\theta + q_Z\sin\theta)\right]$$

By using a polar coordinate system, it results that $q_r = q_X\cos\theta + q_Z\sin\theta$ and $q_\theta = q_Z\cos\theta - q_X\sin\theta$. From these relations, the equations on the velocity components between the two planes are obtained:

$$u' = -\frac{q_\theta}{2\sin\theta} \tag{3.45}$$

$$w = \frac{q_r}{2\sin\theta} \tag{3.46}$$

The potential function in the two planes is related by the following equation:

$$\phi'_2 - \phi'_1 = \int_{\theta_1}^{\theta_2} q_\theta \frac{b}{2}\, d\theta = -\int_{x_1}^{x_2} u'\, dx \tag{3.47}$$

with $x_1 > x_2$ and $\theta_2 > \theta_1$.

The distribution of sources and sinks

Let H^+ be an infinitesimal source sheet distributed on the upper side of the circle. The potential function ϕ' in the point (x, z), induced by such a distribution, is given by the following integral:

$$\phi'(x,z,t) = \frac{1}{4\pi}\int_{-b}^{b} H^+(\xi,t)\ln\left[(x-\xi)^2 + z^2\right] d\xi \tag{3.48}$$

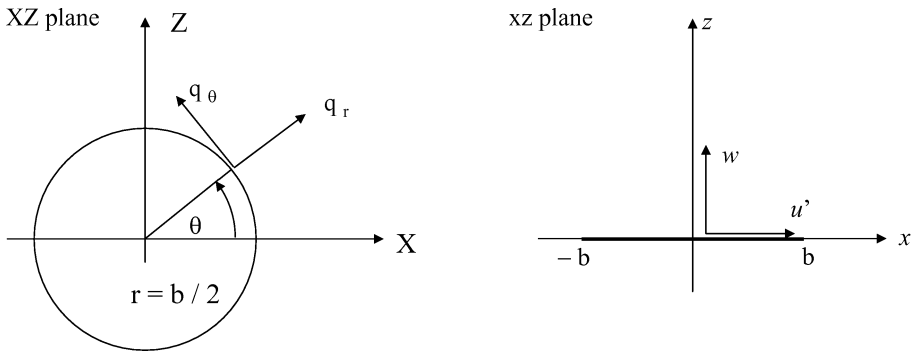

Figure 3.2: Conformal transformation of a circle in the plane XZ to a flat plate in the plane xz.

The wall normal velocity is obtained by evaluating in $z = 0$ the derivative of (3.48) with respect to z:

$$w(x, 0^+, t) = \frac{\partial \phi'}{\partial z}(x, 0^+, t) \tag{3.49}$$

The calculation of this derivative is reported.

Since the flat plate is in $z = 0$, a limit process for $z \to 0^+$ has to be considered.

$$\begin{aligned} w(x, 0^+, t) &= \frac{1}{4\pi} \lim_{z \to 0^+} \frac{\partial}{\partial z} \int_{-b}^{b} H^+(\xi, t) \ln\left[(x - \xi)^2 + z^2\right] d\xi = \\ &= \frac{1}{4\pi} \lim_{z \to 0^+} \int_{-b}^{b} \frac{2z H^+(\xi, t)}{(x - \xi)^2 + z^2} \, d\xi \end{aligned} \tag{3.50}$$

It can be observed that the limit (3.50) is equal to zero for $x \neq \xi$. For $x = \xi$ the integrand function is not defined. A second limit process is considered. Let $[x - \epsilon, x + \epsilon]$ be a small intervall and compute the integral within it. We obtain:

$$w(x, 0^+, t) = \frac{1}{2\pi} \lim_{z \to 0^+} \int_{x-\epsilon}^{x+\epsilon} \frac{z H^+(\xi, t)}{(x - \xi)^2 + z^2} \, d\xi \tag{3.51}$$

Because of the continuity of $H^+(\xi, t)$, it differs from the mean value for a quantity of order $O(\epsilon)$. Then, it can be moved out of the integral sign. By defining $\xi' = (x - \xi)/z$, we have:

$$\begin{aligned} w(x, 0^+, t) &= \frac{H^+(x, t)}{2\pi} \lim_{z \to 0^+} \int_{-\epsilon/z}^{\epsilon/z} \frac{1}{\xi'^2 + 1} \, d\xi' = \\ &= \frac{H^+(x, t)}{\pi} \lim_{z \to 0^+} \operatorname{atan}\left(\frac{\epsilon}{z}\right) = \frac{1}{2} H^+(x, t) \end{aligned} \tag{3.52}$$

Thus, the relation between the source intensity and the wall normal velocity is established.

On the basis of equation (3.52), the source intensity is related to the wall normal velocity as:

$$H^+(x,t) = 2\, w_a(x,t) \tag{3.53}$$

In a similar fashion, a distribution of sinks on the lower side of the flat plate provides the following relation:

$$H^-(x,t) = -2w_a(x,t) \tag{3.54}$$

Because of the equation (3.46), we have the same relations in the plane XZ:

$$H^+(\theta,t) = 4w_a(x,t)\sin\theta \tag{3.55}$$

$$H^-(\theta,t) = -4w_a(x,t)\sin\theta \tag{3.56}$$

The velocity resulting from the distribution of sources and sinks has to be derived. Consider two points $Q^+(r,\psi)$ and $Q^-(r,-\psi)$ symmetrically located on the circumference (see scheme in figure (3.3)). The velocity in a point $P(r,\theta)$ induced by the source $H^+\, r\, d\psi$ and by the sink $H^-\, r\, d\psi$ is built on the basis of geometrical considerations.

Since the velocity induced by a source is inversely proportional to the radial distance, we have:

$$|dq^+| = \frac{H^+ r d\psi}{2\pi\,|P-Q^+|} \tag{3.57}$$

$$|dq^-| = \frac{H^- r d\psi}{2\pi\,|P-Q^-|} \tag{3.58}$$

From the scheme (3.3), we have:

$$\begin{aligned} |P-Q^+| &= r\sqrt{(\sin\psi-\sin\theta)^2+(\cos\theta-\cos\psi)^2} = 2r\sin\frac{\psi-\theta}{2} \\ |P-Q^-| &= 2r\sin\frac{\psi+\theta}{2} \end{aligned}$$

The component dq_θ along the θ direction is obtained by projecting the components dq^+ e dq^- on the tangent direction in P. The angle between dq^+ and dq_θ is $\frac{\psi-\theta}{2}$ and between

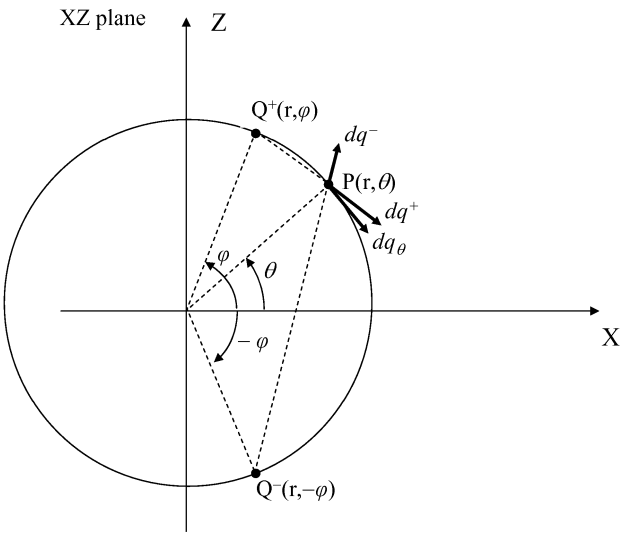

Figure 3.3: Scheme of the velocity components on the circumference in the complex plane

dq^- and dq_θ is $\frac{\psi+\theta}{2}$. Then

$$\begin{aligned} dq_\theta &= -|dq^+|\cos\frac{\psi-\theta}{2} + |dq^-|\cos\frac{\psi+\theta}{2} = \\ &= \frac{r}{2\pi}\left(-\frac{H^+}{|P-Q^+|}\cos\frac{\psi-\theta}{2} + \frac{H^-}{|P-Q^-|}\cos\frac{\psi+\theta}{2}\right)d\psi = \\ &= \frac{1}{4\pi}\left(-\frac{H^+}{\sin\frac{\psi-\theta}{2}}\cos\frac{\psi-\theta}{2} + \frac{H^-}{\sin\frac{\psi+\theta}{2}}\cos\frac{\psi+\theta}{2}\right)d\psi = \\ &= -\frac{w_a(x,t)\sin\theta}{\pi}\left(\frac{\cos\frac{\psi-\theta}{2}}{\sin\frac{\psi-\theta}{2}} + \frac{\cos\frac{\psi+\theta}{2}}{\sin\frac{\psi+\theta}{2}}\right)d\psi \end{aligned} \tag{3.59}$$

By exploiting the following trigonometrical identity:

$$\frac{\cos\frac{\psi-\theta}{2}}{\sin\frac{\psi-\theta}{2}} + \frac{\cos\frac{\psi+\theta}{2}}{\sin\frac{\psi+\theta}{2}} = \frac{-2\sin\theta}{\cos\psi-\cos\theta} \tag{3.60}$$

we have that

$$dq_\theta = \frac{w_a(x,t)}{\pi}\frac{2\sin^2\psi}{\cos\psi-\cos\theta}\,d\psi \tag{3.61}$$

The velocity induced by the whole distribution is obtained by integrating in ψ in the interval $[0\,\pi]$.

The final result is:

$$q_\theta(\theta,t) = \frac{2}{\pi}\int_0^\pi \frac{w_a(x,t)\sin^2\psi}{\cos\psi-\cos\theta}\,d\psi \tag{3.62}$$

The potential function ϕ' is obtained on the basis of the equation (3.47):

$$\phi'_U(\theta,t)-\phi'(\pi,t) = -\frac{b}{\pi}\int_\theta^\pi\int_0^\pi \frac{w_a(x,t)\sin^2\psi}{\cos\psi-\cos\theta}\,d\psi d\theta \tag{3.63}$$

Because of the arbitrary time function in the definition of the potential $\phi\,'$, it is possible to put $\phi'(\pi,t)=0$. Besides, for the symmetry, we observe that the following relation subsists between the lower and upper side potential:

$$\phi'_L(-\theta,t) = -\phi'_U(\theta,t)$$

We suppose the profile oscillates around an axis located at a distance a from the origin and makes vertical displacements h in z direction. Then, the instantaneous position is given by:

$$z_a(x,t) = -h-\alpha(x-ba) \tag{3.64}$$

from which

$$w_a(x,t) = -\dot{h}-\dot{\alpha}(x-ba)-U_\infty\alpha \tag{3.65}$$

By taking into account that $x=b\cos\theta$ and using the relation (3.63), we need to calculate the following integral:

$$\begin{aligned}\phi'_U(\theta,t) = \frac{b}{\pi}(\dot{h}+U_\infty\alpha)\int_\theta^\pi\int_0^\pi \frac{\sin^2\psi}{\cos\psi-\cos\theta}\,d\psi d\theta + \\ \frac{b^2\dot{\alpha}}{\pi}\int_\theta^\pi\int_0^\pi \frac{\sin^2\psi(\cos\theta-a)}{\cos\psi-\cos\theta}\,d\psi d\theta\end{aligned} \tag{3.66}$$

It is useful to calculate the following primitive:

$$F = \int \frac{1}{c_1 \cos t + c_2}\, dt \tag{3.67}$$

with the hypothesis that $c_1 + c_2 \neq 0$. By defining m as

$$m = \frac{c_1 - c_2}{c_1 + c_2}$$

two cases have to be solved in function of the sign of m. If we suppose that $m < 0$ the primitive of (3.67) is:

$$F = \frac{2}{c_1 + c_2} \frac{1}{\sqrt{-m}} \tan^{-1}\left(g(t)\sqrt{-m}\,\right) \tag{3.68}$$

Otherwise

$$F = \frac{1}{c_1 + c_2} \frac{1}{\sqrt{m}} \log\left|\frac{\sqrt{m} + g(t)}{\sqrt{m} - g(t)}\right| \tag{3.69}$$

with

$$g(t) = \sqrt{\frac{1 - \cos t}{1 + \cos t}}$$

By considering in equation (3.66) the integration in ψ we have:

$$\begin{aligned} \int_0^\pi \frac{\sin^2\psi}{\cos\psi + b}\, d\psi &= \int_0^\pi \left(\frac{1 - c_2^2}{\cos\psi + c_2} - \cos\psi + c_2\right) d\psi = \\ &= (1 - c_2^2)\int_0^\pi \frac{1}{\cos\psi + c_2} d\psi + c_2\pi \end{aligned} \tag{3.70}$$

where $c_2 = -\cos\theta$. The primitive of the integral in equation (3.70) is obtained using the equation (3.67) with $a = 1$. In such a case $m = \frac{1 + \cos\theta}{1 - \cos\theta} \geq 0$ for $\theta \in]0, \pi]$. It can be noted that $g(0) = 0$ and, as a consequence, from (3.69) $F(0) = 0$. In $t = \pi$, $g(\pi)$ is not defined. However for $t \to \pi$, the limit of (3.69) provides $F(\pi) = 0$. The first integral in equation (3.66) gives:

$$\int_\theta^\pi \int_0^\pi \frac{\sin^2\psi}{\cos\psi - \cos\theta} d\psi d\theta = -\pi \int_\theta^\pi \cos\theta\ d\theta = \pi\ \sin\theta \tag{3.71}$$

The second integral in (3.66) is calculated as:

$$\int_\theta^\pi \int_0^\pi \frac{\sin^2\psi\cos\theta}{\cos\psi - \cos\theta} d\psi d\theta = \frac{\pi}{2}\sin\theta\cos\theta \tag{3.72}$$

On the basis of the integrals (3.71) and (3.72), we obtain that

$$\phi'_U(\theta, t) = b(\dot{h} + U_\infty\,\alpha)\sin\theta + b^2\dot{\alpha}\,(\,\frac{1}{2}\,\cos\theta - a\,) \tag{3.73}$$

From the Bernoulli equation (3.39), the pressure can be related to the potential function. The pressure difference $p_U - p_L$ is computed as:

$$p_U - p_L = \left[U_\infty \left(\frac{\partial \phi'_U}{\partial x} - \frac{\partial \phi'_L}{\partial x} \right) + \left(\frac{\partial \phi'_U}{\partial t} - \frac{\partial \phi'_L}{\partial t} \right) \right] \tag{3.74}$$

By exploiting the symmetry properties of ϕ', we have:

$$p_U - p_L = -2U_\infty \frac{\partial \phi'_U}{\partial x} - 2\frac{\partial \phi'}{\partial t} = \frac{2U_\infty}{b \sin\theta} \frac{\partial \phi'_U}{\partial \theta} - 2\frac{\partial \phi'}{\partial t} \tag{3.75}$$

By integrating equation (3.75), the expression of the *non circulatory* portion of the lift is obtained:

$$\begin{aligned} L_{NC} &= -\int_{-b}^{b} (p_U - p_L) dx = \int_{-b}^{b} 2U_\infty \frac{\partial \phi'_U}{\partial x} - 2\frac{\partial \phi'_U}{\partial t} dx = \\ &= 2U_\infty \Big[\phi'_U \Big]_{-b}^{b} - \int_{-b}^{b} 2\rho \, \frac{\partial \phi'_U}{\partial t} \, dx \end{aligned} \tag{3.76}$$

It is worth noting that the source and sink distributions do not introduce circulation in the field. As a consequence, the potential function ϕ' is single valued and vanishes at the trailing edge because $\phi'(0,t) = 0$. With this information, we obtain that:

$$\begin{aligned} L_{NC} &= -2\int_{-b}^{b} \frac{\partial \phi'_U}{\partial t} dx = -2\frac{\partial}{\partial t} \int_{-b}^{b} \phi'_U \, dx = \\ &= 2\frac{\partial}{\partial t} \int_0^\pi \phi'_U \sin\theta \, d\theta \end{aligned} \tag{3.77}$$

By calculating the integral in equation (3.77), the *non circulatory* part of the lift is obtained.

$$L_{NC} = = \pi b^2 \big(\ddot{h} + U_\infty \dot{\alpha} - a \, b \, \ddot{\alpha} \big) \tag{3.78}$$

It must be pointed out that a vertical displacement at a constant velocity $\dot{h}$ does not have unsteady effects on the lift. It is fully equivalent to the effects of a steady flow incidence α such that $\dot{h} = U\alpha$. We report also the *non circulatory* part of the aerodynamic moment

$$M_{NC} = \int_{-b}^{b} (p_U - P_L)(x - ba) dx \tag{3.79}$$

The final result is:

$$M_{NC} = \pi b^2 \left[U_\infty \dot{h} + ba\ddot{h} + U_\infty^2 \alpha - b^2 \left(\frac{1}{8} + a^2 \right) \ddot{\alpha} \right] \tag{3.80}$$

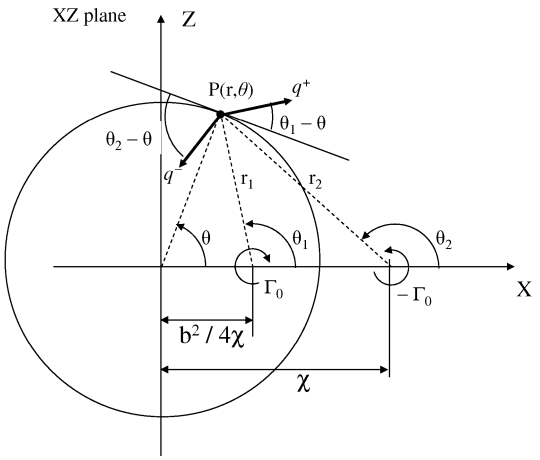

Figure 3.4: *Bound* vortex of intensity Γ_0 and its image of intensity $-\Gamma_0$.

3.3.2 Circulatory contribution

The *non circolatory* part is not able to fulfil the Kutta condition at the trailing edge. In fact, from the equations (3.45) e (3.46) for $x = b$, $\theta = 0$ and $u \to \infty$. Theodorsen resolves this problem by superimposing a vorticity distribution on the body surface (*bound* vorticity) and in the wake (*free* vorticity). But, the boundary conditions of the *non circulatory* part have to be respected together with the condition that circumference in the plane XZ and the plate in the plane xz are stream lines. For this reason, the technique of the image vortices are used. A vortex located at $(\chi, 0)$ of intensity $-\Gamma_0$ in the plane XZ has its image Γ_0 in $(b^2/4\chi, 0)$. This vortex pair respects the condition of a stream line for the circumference. By referring to the figure (3.4), consider the *bound* vortex of intensity Γ_0 and its image $-\Gamma_0$. The centers are located in $(b^2/4\chi, 0)$ and $(\chi, 0)$ respectively. The induced velocity in the point $P(r, \theta)$ is tangent to the circumference. It is possible to show

that the radial component is zero. In this way, the boundary conditions on the body are not modified by the vorticity distribution.

$$\begin{aligned} q(r,\theta) &= q^- \cos(\theta_2 - \theta) - q^+ \cos(\theta_1 - \theta) = \\ &= \frac{\Gamma_0}{2\pi}\left[\frac{r_2 \cos(\theta_2 - \theta)}{r_2^2} - \frac{r_1 \cos(\theta_1 - \theta)}{r_1^2}\right] \end{aligned} \tag{3.81}$$

By geometrical considerations in figure (3.4), we obtain the following relations:

$$r_2^2 = \chi^2 + \left(\frac{b}{2}\right)^2 - \chi b \cos\theta \tag{3.82}$$

$$r_1^2 = \left(\frac{b^2}{4\chi}\right)^2 + \left(\frac{b}{2}\right)^2 - \frac{b^3}{4\chi}\cos\theta \tag{3.83}$$

Furthermore:

$$r_2 \cos(\theta_2 - \theta) = \frac{b}{2} - \chi \cos\theta \tag{3.84}$$

$$r_1 \cos(\theta_1 - \theta) = \frac{b}{2} - \frac{b^2}{4\chi}\cos\theta \tag{3.85}$$

By substituting these relation in equation (3.81), we have:

$$\begin{aligned} q(r,\theta) &= \frac{\Gamma_0}{2\pi}\left[\frac{\frac{b}{2} - \chi\cos\theta}{\chi^2 + \left(\frac{b}{2}\right)^2 - \chi b\cos\theta} - \frac{\frac{b}{2} - \frac{b^2}{4\chi}\cos\theta}{b^2/(4\chi^2)\left[\left(\frac{b^2}{4}\right)^2 + \chi^2 - \chi b\cos\theta\right]}\right] = \\ &= -\frac{\Gamma_0}{\pi b}\left[\frac{\chi^2 - \frac{b^2}{4}}{\chi^2 + \frac{b^2}{4} - \chi b\cos\theta}\right] \end{aligned} \tag{3.86}$$

And, by computing the potential function ϕ'_U:

$$\begin{aligned} \phi'_U(\theta,t) &= -\int_\theta^\pi q_\theta \frac{b}{2}\, d\theta = \\ &= \frac{\Gamma_0}{2\,\pi}\left(\chi^2 - \frac{b^2}{4}\right)\int_\theta^\pi \frac{1}{\chi^2 + \frac{b^2}{4} - \chi b\cos\theta}\, d\theta \end{aligned} \tag{3.87}$$

The integral (3.87) can be computed by exploiting the equation (3.67) with $c_1 = -\chi\, b$ and $c_2 = \chi^2 + (\frac{1}{2}b)^2$. In such a case,

$$m = \frac{-\chi\, b - \chi^2 - (\frac{1}{2}b)^2}{-\chi\, b + \chi^2 + (\frac{1}{2}b)^2} = -\frac{(\chi + \frac{1}{2}b)^2}{(\chi - \frac{1}{2}b)^2} < 0$$

The primitive (3.68) must be used, which provides:

$$F = -\frac{2}{\chi^2 - (\frac{1}{2}b)^2} \tan^{-1}\left[\frac{(\chi - \frac{1}{2}b)}{(\chi + \frac{1}{2}b)}\sqrt{\frac{1+\cos t}{1-\cos t}}\right] \tag{3.88}$$

As a consequence,

$$\begin{aligned}\phi'_U(\theta,t) &= -\frac{\Gamma_0}{\pi}\left[\tan^{-1}\left(\frac{(\chi - \frac{1}{2}b)}{(\chi + \frac{1}{2}b)}\sqrt{\frac{1+\cos t}{1-\cos t}}\right)\right]_\theta^\pi = \\ &= \frac{\Gamma_0}{\pi}\tan^{-1}\left(\frac{(\chi - \frac{1}{2}b)}{(\chi + \frac{1}{2}b)}\sqrt{\frac{1+\cos\theta}{1-\cos\theta}}\right)\end{aligned} \tag{3.89}$$

By means of equation (3.89), we are able to compute the pressure distribution by using the equation (3.75). But in such a case, the time dependency appears through the variable $\chi(t)$ which indicated the instantaneous position of the wake vortex. The hypothesis that the vortex is shed at the free stream velocity is adopted. This assumption allows for the following transformation:

$$\frac{d\xi}{dt} = U_\infty \tag{3.90}$$

where ξ is the vortex location in the plane xz which corresponds to

$$\xi = \chi + \frac{b^2}{4\chi} \tag{3.91}$$

in the plane XZ. Equation (3.91) can be cast as follows:

$$\sqrt{\frac{\xi - b}{\xi + b}} = \frac{\chi - (b/2)}{\chi + (b/2)} \tag{3.92}$$

In this way, equation (3.89) can be written as:

$$\phi'_U(\theta,t) = \frac{\Gamma_0}{\pi}\tan^{-1}\sqrt{\frac{(\xi - b)(1+\cos\theta)}{(\xi + b)(1-\cos\theta)}} \tag{3.93}$$

The derivative of (3.93) with respect to the time t is:

$$\frac{\partial\phi'_U}{\partial t} = U_\infty\frac{\partial\phi'_U}{\partial\xi} = \frac{b\,U_\infty\Gamma_0}{\pi}\frac{\sin\theta}{\xi - b\cos\theta}\frac{1}{\sqrt{(\xi^2 - b^2)}} \tag{3.94}$$

The derivative with respect to θ gives:

$$\frac{\partial \phi'_U}{\partial \theta} = -\frac{\Gamma_0}{2\pi} \frac{\sqrt{\xi^2 - b^2}}{(\xi - b\ \cos\theta)} \tag{3.95}$$

By using the expressions (3.94) and (3.95) in the Bernoulli equation (3.75) the pressure difference can be computed:

$$\begin{aligned} (p_U - p_L)_{\Gamma_0} &= \frac{2U_\infty}{b \sin\theta} \frac{\partial \phi'_U}{\partial \theta} - 2\frac{\partial \phi'}{\partial t} = \\ &= -\frac{U_\infty \Gamma_0}{\pi\ b \sin\theta} \left(\frac{\xi + b\cos\theta}{\sqrt{(\xi^2 - b^2)}} \right) \end{aligned} \tag{3.96}$$

From equation (3.96) the lift produced by the pair of vortices of intensity Γ_0 is determined:

$$L_{\Gamma_0} = -\int_0^\pi (p_U - p_L)\ b\ \sin\theta\ d\theta = \frac{U_\infty\ \Gamma_0\ \xi}{\sqrt{\xi^2 - b^2}} \tag{3.97}$$

It can be noted that for $\xi \to \infty$, (i.e., $t \to \infty$) the lift tends to the value produced by a single vortex of intensity Γ_0. When we deal with a distribution of wake vorticity, the treatment must be referred to an element of vorticity:

$$\Gamma_0 = -\gamma_w(\xi, t)\ d\xi \tag{3.98}$$

Now, the velocity expressed by equation (3.86) transforms to:

$$q(r, \theta) = \int_b^\infty \frac{\gamma_w\ d\xi}{\pi b} \left[\frac{\chi^2 - \frac{b^2}{4}}{\chi^2 + \frac{b^2}{4} - \chi b \cos\theta} \right] \tag{3.99}$$

The pressure difference due to the complete system of wake vorticity is obtained by integrating the equation (3.96) in ξ from b to ∞ downstream the airfoil.

$$p_U - p_L = \frac{U_\infty}{\pi b\ \sin\theta} \int_b^\infty \left(\frac{\xi + b\cos\theta}{\sqrt{\xi^2 - b^2}} \right) \gamma_w(\xi, t) d\xi \tag{3.100}$$

It is convenient to arrange the last integral as follows:

$$p_U - p_L = \frac{U_\infty}{\pi b\ \sin\theta} \int_b^\infty \left[\frac{\xi(1 - \cos\theta)}{\sqrt{\xi^2 - b^2}} + \cos\theta \sqrt{\frac{\xi + b}{\xi - b}} \right] \gamma_w(\xi, t) d\xi \tag{3.101}$$

By integrating from the trailing edge to infinity we find the complete effect of the wake vorticity on the lift:

$$L_C = -U_\infty \int_b^\infty \frac{\xi}{\sqrt{\xi^2 - b^2}} \gamma_w(\xi, t) d\xi \tag{3.102}$$

3.3.3 The Kutta's condition

Equation (3.102) establishes that the *circulatory* portion of the lift is determined by the distribution of wake vorticity $\gamma_w(\xi, t)$ which is unknown. The Kutta condition allows to specify a further equation to compute this quantity. The velocity at the trailing edge is given by adding the relations (3.62) and (3.86) with $\theta = 0$. The Kutta condition establishes that the velocity at the trailing edge is zero, namely:

$$\frac{2}{\pi}\int_0^\pi \frac{w_a(x,t)\sin^2\psi}{\cos\psi - 1}\,d\psi + \int_b^\infty \frac{\gamma_w\,d\xi}{\pi b}\left[\frac{\chi^2 - \frac{b^2}{4}}{\chi^2 + \frac{b^2}{4} - \chi b}\right] = 0 \tag{3.103}$$

By taking into account the relation (3.92) between χ and ξ, the Kutta condition can be written as:

$$\frac{2}{\pi}\int_0^\pi \frac{w_a(x,t)\sin^2\psi}{\cos\psi - 1}\,d\psi + \frac{1}{\pi b}\int_b^\infty \sqrt{\frac{\xi + b}{\xi - b}}\gamma_w(\xi,t)\,d\xi = 0 \tag{3.104}$$

In equation (3.104), the boundary condition prescribes $w_a(x,t)$, (see equation 3.65). Then the unique unknown is $\gamma_w(\xi,t)$. Theodorsen indicates with Q the following integral:

$$Q = -\frac{1}{2\pi b}\int_b^\infty \sqrt{\frac{\xi + b}{\xi - b}}\gamma_w(\xi,t)\,d\xi \tag{3.105}$$

Then, equation (3.104) becomes:

$$Q = \frac{1}{\pi}\int_0^\pi \frac{w_a(x,t)\sin^2\psi}{\cos\psi - 1}\,d\psi \tag{3.106}$$

By substituting the expression of $w_a(x,t)$ in equation (3.65), we have:

$$\begin{aligned} Q &= \frac{1}{\pi}\int_0^\pi \frac{(-\dot{h} - \dot{\alpha}b(\cos\psi - a) - U_\infty\alpha)\sin^2\psi}{\cos\psi - 1}\,d\psi = \\ &= \frac{1}{\pi}\int_0^\pi \left[\dot{h} + \dot{\alpha}b(\cos\psi - a) + U_\infty\alpha\right](1 + \cos\psi)\,d\psi = \\ &= \dot{h} + U_\infty\alpha + b\left(\frac{1}{2} - a\right)\dot{\alpha} \end{aligned} \tag{3.107}$$

Then, we can write the circulatory part of the lift as:

$$L_C = 2\pi\, b\, U_\infty Q \frac{\displaystyle\int_b^\infty \frac{\xi}{\sqrt{\xi^2 - b^2}} \gamma_w(\xi, t) d\xi}{\displaystyle\int_b^\infty \sqrt{\frac{\xi + b}{\xi - b}} \gamma_w(\xi, t)\, d\xi} \tag{3.108}$$

The effects of the wake vorticity $\gamma_w(\xi, t)$ are represented by the ratio of the two integrals in equation (3.108). By assuming simple harmonic oscillations in time, we can write the displacement and the velocity on the flat plate as:

$$z_a(x, t) = \bar{z}_a e^{i\omega t} \tag{3.109}$$

$$w_a(x, t) = \bar{w}_a e^{i\omega t} \tag{3.110}$$

When a periodic solution is established, also the wake vorticity takes a similar form. However, because it is convected downstream, a time delay has to be considered. The wake vorticity can be described in the form:

$$\gamma_w(\xi, t) = \bar{\gamma}_w e^{i\omega(t - \frac{\xi}{U_\infty})} \tag{3.111}$$

By defining the reduced frequency $k = \omega\, b/U_\infty$ and $\xi = \xi^*\, b$,

$$\gamma_w(\xi, t) = \bar{\gamma}_w e^{i\omega(t - k\xi^*)} \tag{3.112}$$

The ratio of the integrals in (3.108) can be manipulated as:

$$\frac{\displaystyle\int_b^\infty \frac{\xi}{\sqrt{\xi^2 - b^2}} \gamma_w(\xi, t) d\xi}{\displaystyle\int_b^\infty \sqrt{\frac{\xi + b}{\xi - b}} \gamma_w(\xi, t)\, d\xi} = \frac{\displaystyle\int_1^\infty \frac{\xi^*}{\sqrt{\xi^{*2} - 1}} d\xi^*}{\displaystyle\int_1^\infty \sqrt{\frac{\xi^* + 1}{\xi^* - 1}}\, d\xi^*} = C(k) \tag{3.113}$$

$C(k)$ is said Theodorsen's function and can be expressed by means of Hankel functions of the second kind:

$$C(k) = F(k) + iG(k) = \frac{H_1^2(k)}{H_1^2(k) + iH_0^2(k)} \tag{3.114}$$

where $H_n^2(k)$ is a combination of Bessel's functions:

$$H_n^2(k) = J_n - iY_n \tag{3.115}$$

The $C(k)$ function is then computed for a given value of the reduced frequency. Therefore, by collecting the equations (3.78), (3.107) and (3.108) the final expression of the Theodorsen's solution is obtained:

$$\begin{aligned} L &= \pi b^2 \left(\ddot{h} + U_\infty \dot{\alpha} - a\, b\, \ddot{\alpha}\right) + \\ &+ 2\pi\, b\, U_\infty C(k) \left[\dot{h} + U_\infty \alpha + b\left(\frac{1}{2} - a\right)\, \dot{\alpha}\right] \end{aligned} \tag{3.116}$$

The expression of the aerodynamic moment is also reported:

$$\begin{aligned} M &= \pi b^2 \left[ba\ddot{h} - U_\infty b\left(\frac{1}{2} - a\right)\, \dot{\alpha} - b^2\left(\frac{1}{8} + a^2\right)\ddot{\alpha}\right] \\ &+ 2\pi U_\infty b^2 \left(a + \frac{1}{2}\right) C(k) \left[\dot{h} + U_\infty \alpha + b\left(\frac{1}{2} - a\right)\, \dot{\alpha}\right] \end{aligned} \tag{3.117}$$

3.3.4 Observations

Theodersen'solution highlights the fundamental features of the unsteady inviscid flow around a thin airfoil. By specializing the equation (3.116) with $\dot{h} = \ddot{h} = 0$, $a = -1/2$ and $\alpha = e^{i\omega t}$ and dividing by $U_\infty^2/2$, the expression of the lift coefficient for an oscillating airfoil is obtained:

$$C_l = \pi\, k\alpha \left(i - \frac{k}{2}\right) + 2\pi C(k)\,(1 + i\, k) \tag{3.118}$$

where the position

$$\omega = \frac{2U_\infty k}{c}$$

has been used. The Theodorsen function $C(k) = F(k) + iG(k)$ is represented in figure (3.5). It is worth noting that as $k \to 0$, $F(k) \to 1$ and $G(k) \to 0$ obtaining the linear steady theory of thin airfoils. In figure (3.6a) the curves obtained by the equation (3.118) are reported for different values of the reduced frequency. For $k \to \infty$, $F(k) \to 0.5$ and $G(k) \to 0$ as well, producing a clockwise rotation of the real part of equation (3.118), as can be seen in figure (3.6b). The complex terms are reported in figure (3.6c). For $k \to \infty$, the non circulatory part diverges because of the proportionality to k. However, for high reduced frequencies, the theory is no longer reliable because the hypothesys of small disturbances is mismatched. Finally, in figure

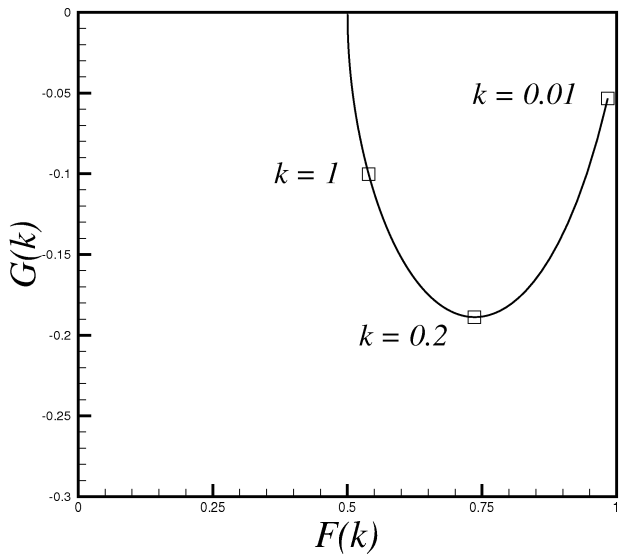

Figure 3.5: Theodorsen function, $C(k) = F(k) + iG(k)$.

(3.6d) a numerical comparison between the inviscid flow solution around the NACA0012 and NACA0006 airfoils against the function (3.118) is reported at $k = 0.05$ and $\alpha = 3° \sin(2kt)$. The agreement improves by reducing the thickness of the airfoil because such contribution is not taken into account by the Theodorsen solution.

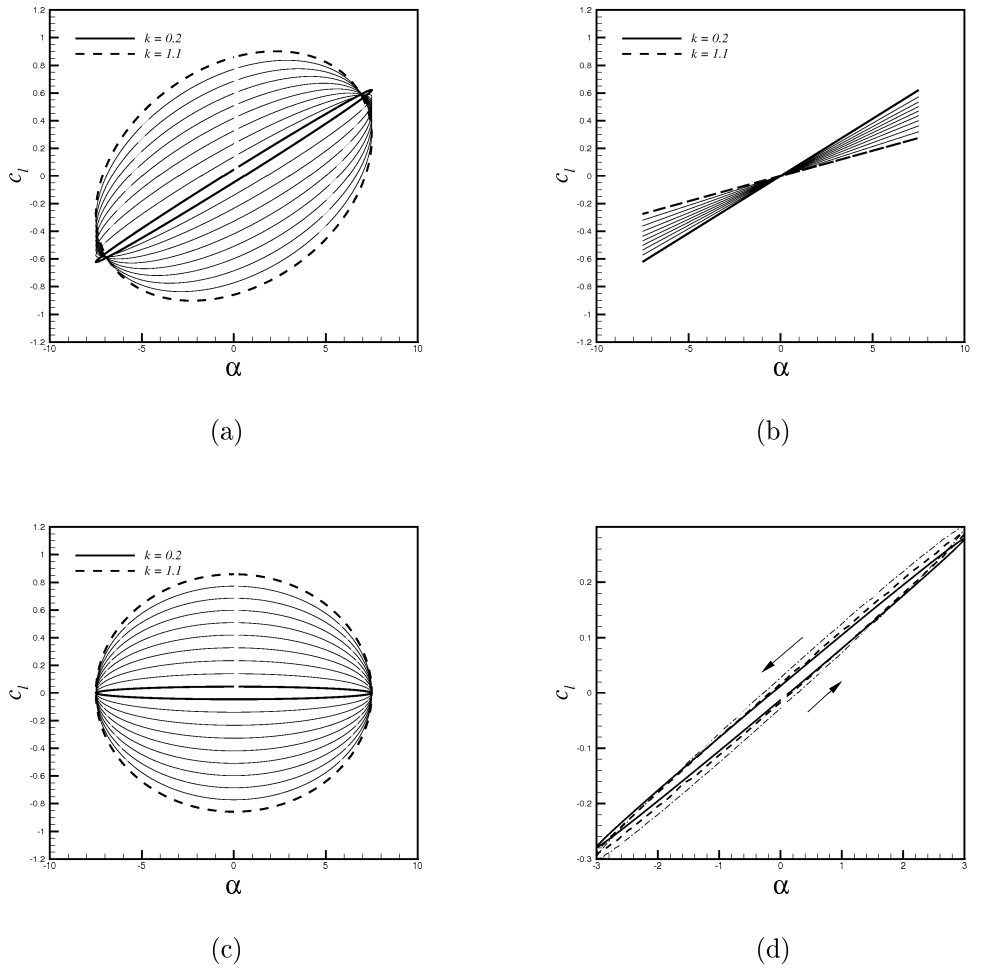

Figure 3.6: Inviscid flow past an oscillating airfoil. (a), Theodorsen solution from $k = 0.2$ to $k = 1.1$; (b), real part of Theodorsen's solution; (c), imaginary part of Theodorsen's solution; (d), numerical flow solutions at $k = 0.1$ and $\alpha = 3^\circ \sin(2kt)$: NACA0012 $- \cdot -$, NACA0006 $- - -$, Theodorsen's solution —.

Chapter 4

A New Far Field Theory

In the present chapter, a *far field* theory, expressing the aerodynamic force by means of the Lamb vector field, is discussed. As pointed in the introduction, many *far field* techniques are usually applied to numerical solutions for steady flows. The extension of the force prediction methods to unsteady flows is not trivial. In this regard, much theoretical research has been carried out on the Vortex Dynamics. Several interesting theories able to supply the *far field* aerodynamic force also in the unsteady case have been developed, even if for incompressible flows. Among various results, the work of Wu J.C. [73] in 1981 is of particular relevance because it constitutes a first *far field* aerodynamic theory for viscous and unsteady flows.

In 2006, Wu J.Z. & al. [74] published an improvement of the Wu J. C.'s formulation. In this theory, The Lamb vector $\underline{\boldsymbol{l}}$ appears to be the key quantity in the generation of the aerodynamic force. In 2007, the same research group [75] showed the first numerical applications of this theory to flows at low Reynolds number ($\sim 10^4$). There are not yet published results concerning the use of such theory to flow at very high Reynolds number.

The aim of the present chapter is to explore the potentialities of Wu's theory in predicting the aerodynamic force for high Reynolds turbulent flows. The conceptual gap between the results obtained for the inviscid flows and the viscous and turbulent ones is thus filled. By means of the Lamb vector integrals we show a practical way to extract the aerodynamic force from a numerical flow field. Such approach includes also the possibility to deal with unsteady flow regimes. For this purpose, the theory is reviewed and extended

under the perspective of the Reynolds Averaged Navier Stokes equations.

4.1 The *far field* approach

The aerodynamic force $\underline{\mathbf{F}}$ is defined as the resultant of the actions exerted on one o more solid bodies by the external flow. By following the notation introduced in chapter 3, let ∂B be the boundary surface that separates the airfoil volume B from the fluid volume Ω (see the scheme in figure 4.1). The definition of the aerodynamic force, already given for inviscid flows in equation (3.8), is modified for viscous flows as follows:

$$\underline{\mathbf{F}} = \int_{\partial B} (p \, \underline{\underline{\mathbf{I}}} - \underline{\underline{\tau}}) \cdot \underline{n} \, dS \tag{4.1}$$

The equation (4.1) represents the *near field* definition of the aerodynamic force because is based on the surface integration along the solid body contours. Generally, the integral (4.1) depends on the time t. Such a dependency is caused from the unsteady behaviour of the integrand functions, pressure and the shear stresses, as well as by the motion or deformation of the body surface $\partial B = \partial B(t)$. Other forms of the aerodynamic force are achievable by exploiting the balance equation of the flow momentum:

$$\int_{\Omega} \rho \, \underline{\mathbf{a}} \, dV = \int_{\partial\Omega} (-p \, \underline{\underline{\mathbf{I}}} + \underline{\underline{\tau}}) \cdot \underline{n} \, dS \tag{4.2}$$

where $\partial\Omega = \partial B \cup \Sigma$, and Σ is a closed external surface around B. In equation (4.2),

$$\underline{\mathbf{a}} = \frac{\partial \underline{\mathbf{u}}}{\partial t} + \underline{\mathbf{u}} \cdot \underline{\nabla} \, \underline{\mathbf{u}}$$

is the material derivative of the velocity (fluid acceleration). In equation (4.2), by isolating the surface integral on ∂B, we obtain the *far field* form of the aerodynamic force:

$$\underline{\mathbf{F}} = - \int_{\Omega} \rho \, \underline{\mathbf{a}} \, dV - \int_{\Sigma} (p \, \underline{\underline{\mathbf{I}}} - \underline{\underline{\tau}}) \cdot \underline{n} \, dS \tag{4.3}$$

Equations (4.1) and (4.3) are equivalent and represent two alternative way to compute the aerodynamic force. The hypothesis is the validity of the

momentum equation (4.2). In equation (4.3), the surface Σ can be chosen in an arbitrary way. The use of the *near field* form (4.1) or the *far field* one (4.3) depends on the capability of measuring the respective integrand functions. Further manipulations are usually introduced with the aim to address some specific issues.

4.2 Wu's theory

In the hypothesis of constant density, we can set $\rho = 1$ throughout the formulas without loss of generality. The following transformations, called Derivative Moment Transformations (DMT), are used in the proofs. Let $\underline{a}$ be a vector field defined in Ω, we have that:

$$\int_{\Omega} \underline{a}\, dV = \int_{\Omega} \underline{\mathbf{r}} \times (\underline{\nabla} \times \underline{a})\, dV - \int_{\partial\Omega} \underline{\mathbf{r}} \times (\underline{n} \times \underline{a})\, dS \tag{4.4}$$

where $\underline{\mathbf{r}} = \underline{\mathbf{x}}\,/(d-1)$ is the scaled position vector and $d = 2, 3$ is the space dimension. Moreover, for a vector field $\phi\, \underline{n}$, the following identity is also applicable on the boundary of Ω:

$$\int_{\partial\Omega} \phi\, \underline{n}\, dS = -\int_{\partial\Omega} \underline{\mathbf{r}} \times (\underline{n} \times \underline{\nabla}\, \phi)\, dS \tag{4.5}$$

By exploiting the Helmholtz equation for the vorticity (obtained by applying the curl operator to the equation (2.8b)),

$$\frac{\partial \underline{\omega}}{\partial t} + \underline{\nabla} \times \underline{\boldsymbol{l}} = \nu \nabla^2 \underline{\omega} \tag{4.6}$$

the first side of equation (4.6) can be cast by using the definition of the accelerator vector:

$$\underline{\nabla} \times\ \underline{\mathbf{a}} = \nu \nabla^2 \underline{\omega} \tag{4.7}$$

We apply the transformation (4.4) to the acceleration vector as follows:

$$\int_{\Omega} \underline{\mathbf{a}}\, dV = \int_{\Omega} \underline{\mathbf{r}} \times \underline{\mathbf{a}}\, dV - \int_{\partial\Omega} \underline{\mathbf{r}} \times (\underline{n} \times \underline{\mathbf{a}})\, dS \tag{4.8}$$

In equation (4.8), the curl of the acceleration is substituted using the equation (4.7):

$$\int_{\Omega} \underline{\mathbf{a}}\, dV = \int_{\Omega} \underline{\mathbf{r}} \times \nu \nabla^2 \underline{\omega}\, dV - \int_{\partial\Omega} \underline{\mathbf{r}} \times (\underline{n} \times \underline{\mathbf{a}})\, dS \tag{4.9}$$

In equation (4.9), the surface integral on $\partial\Omega$, in which the acceleration vector appears, is manipulated by exploiting the momentum equation (4.7):

$$-\int_{\partial\Omega} \underline{\mathbf{r}} \times (\underline{n} \times \underline{\mathbf{a}})\, dS = \int_{\Sigma} \underline{\mathbf{r}} \times \left[\underline{n} \times \left(\underline{\nabla} p - \underline{\nabla} \cdot \underline{\underline{\tau}}\right)\right] dS - \int_{\partial B} \underline{\mathbf{r}} \times (\underline{n} \times \underline{\mathbf{a}})\, dS \tag{4.10}$$

The surface integral on ∂B in equation (4.10) is calculated from the solid surface motion. We indicate this contribution with $\underline{\mathbf{F}}_{III}$:

$$\underline{\mathbf{F}}_{III} = \int_{\partial B} \underline{\mathbf{r}} \times \underline{n} \times \underline{\mathbf{a}}\, dS \tag{4.11}$$

The pressure contribution in the right hand side of (4.10) is transformed using equation (4.5):

$$\int_{\Sigma} \underline{\mathbf{r}} \times \underline{n} \times \underline{\nabla}\, p\, dS = -\int_{\Sigma} p\, \underline{n}\, dS \tag{4.12}$$

By substituting equations (4.10) and (4.12) in the integral (4.9), we have:

$$\begin{aligned} \int_{\Omega} \underline{\mathbf{a}}\, dV &= \int_{\Omega} \underline{\mathbf{r}} \times \nu \nabla^2 \underline{\omega}\, dV - \int_{\Sigma} p\, \underline{n}\, dS + \\ &- \int_{\partial\Omega} \underline{\mathbf{r}} \times \underline{n} \times \underline{\nabla} \cdot \underline{\underline{\tau}}\, dS - \underline{\mathbf{F}}_{III} \end{aligned} \tag{4.13}$$

By inserting the relation (4.13) in the *far field* form expressed by equation (4.3), we have:

$$\begin{aligned} \underline{\mathbf{F}} &= -\int_{\Omega} \underline{\mathbf{r}} \times \nu \nabla^2 \underline{\omega}\, dV + \int_{\Sigma} \underline{\mathbf{r}} \times \underline{n} \times \underline{\nabla} \cdot \underline{\underline{\tau}}\, dS \\ &+ \int_{\Sigma} \underline{\underline{\tau}} \cdot \underline{n}\, dS + \underline{\mathbf{F}}_{III} \end{aligned} \tag{4.14}$$

Also the shear stress tensor $\underline{\underline{\tau}}$ can be expressed in terms of vorticity taking into account that:

$$\underline{\nabla} \cdot \underline{\underline{\tau}} = -\nu\, \underline{\nabla} \times \underline{\omega}$$

$$\underline{\underline{\tau}} \cdot \underline{n} = \nu\, \underline{\omega} \times \underline{n}$$

Now, the aerodynamic force is expressed solely through the knowledge of the vorticity field. In fact:

$$\begin{aligned}\underline{\mathbf{F}} &= -\int_{\Omega} \underline{\mathbf{r}} \times \nu \nabla^2 \underline{\omega}\, dV - \int_{\Sigma} \underline{\mathbf{r}} \times \underline{n} \times (\nu \underline{\nabla} \times \underline{\omega})\, dS \\ &+ \int_{\Sigma} \nu\, \underline{\omega} \times \underline{n}\, dS + \underline{\mathbf{F}}_{III} \end{aligned} \tag{4.15}$$

In synthesis, $\underline{\mathbf{F}}$ is given by the sum of three contributions:

$$\underline{\mathbf{F}} = \underline{\mathbf{F}}_{I} + \underline{\mathbf{F}}_{II} + \underline{\mathbf{F}}_{III} \tag{4.16}$$

The contribution $\underline{\mathbf{F}}_{I}$ is formed by a volume integral on Ω

$$\underline{\mathbf{F}}_{I} = -\int_{\Omega} \left(\underline{\mathbf{r}} \times \nu \nabla^2 \underline{\omega} \right) dV \quad \textit{(diffusion form)} \tag{4.17}$$

Equation (4.17) is called *diffusion* form because contains only viscous vortical terms. In the following, such form will be labeled with $\underline{\mathbf{F}}_{I,\,d}$. The second contribution $\underline{\mathbf{F}}_{II}$ is made by surface integrals on Σ as follows:

$$\underline{\mathbf{F}}_{II} = -\int_{\Sigma} \Big(\underline{\mathbf{r}} \times [\underline{n} \times \nu\, (\underline{\nabla} \times \underline{\omega})] \Big) dS + \int_{\Sigma} \nu\, (\underline{\omega} \times \underline{n})\, dS \tag{4.18}$$

Finally, $\underline{\mathbf{F}}_{III}$, defined in equation (4.11), is associated with the local solid body acceleration. By exploiting the Helmholtz equation for the vorticity (4.6) and the transformation (4.4), the *diffusion* form (4.17) can be cast in an alternative form,

$$\begin{aligned}\underline{\mathbf{F}}_{I} &= -\int_{\Omega} \left(\underline{\mathbf{r}} \times \frac{\partial \underline{\omega}}{\partial t} \right) dV - \int_{\Omega} \underline{\boldsymbol{l}}\, dV \\ &\quad - \int_{\partial\Omega} \underline{\mathbf{r}} \times (\underline{n} \times \underline{\boldsymbol{l}})\, dS \qquad \textit{(advection form)} \end{aligned} \tag{4.19}$$

In equation (4.19), the contribution $\underline{\mathbf{F}}_{I}$ is expressed in terms of the rate of change of the hydrodynamic impulse and Lamb vector integrals. It is called *advection* form and indicated as $\underline{\mathbf{F}}_{I,\,a}$. The vortex force, namely, the volume integral of the Lamb vector, appears explicitly in equation (4.19). In virtue of equation (4.6), the *diffusion* form and *advection* form are equivalent and they represent alternative ways to account for the same flow physics. It

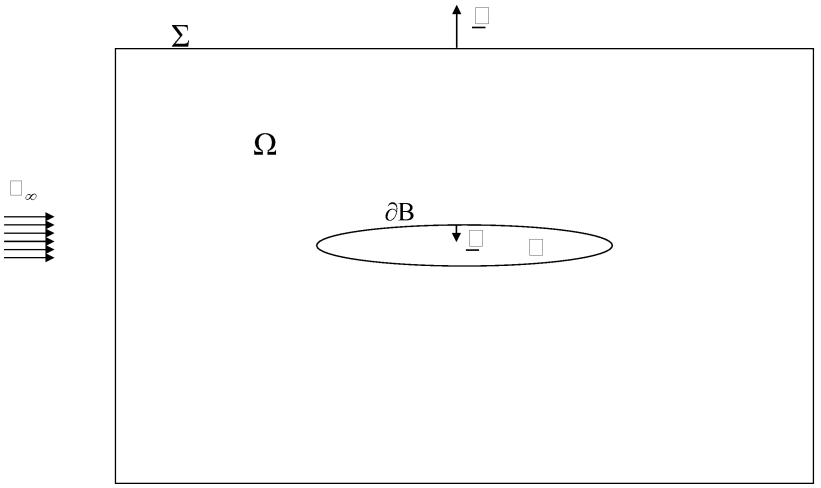

Figure 4.1: Scheme of the fluid control volume around a solid body.

is worth noting that the surface integral in equation (4.19) is extended to $\partial\Omega = \partial B \cup \Sigma$. In the following the contribution on ∂B will be embodied in $\underline{\mathbf{F}}_{III}$ obtaining that:

$$\begin{aligned} \underline{\mathbf{F}}_{I,a} &= -\int_{\Omega} \left(\underline{\mathbf{r}} \times \frac{\partial \underline{\omega}}{\partial t} \right) dV - \int_{\Omega} \underline{\boldsymbol{l}}\, dV \\ &\quad - \int_{\Sigma} \underline{\mathbf{r}} \times (\underline{n} \times \underline{\boldsymbol{l}})\, dS \end{aligned} \tag{4.20}$$

and

$$\underline{\mathbf{F}}_{III} = \int_{\partial B} \underline{\mathbf{r}} \times \underline{n} \times (\underline{\mathbf{a}} - \underline{\boldsymbol{l}})\, dS \tag{4.21}$$

Once a fluid dynamic field is provided, in terms of velocity, vorticity $\underline{\omega}$ and Lamb vector $\underline{\boldsymbol{l}}$ fields, the aerodynamic force is evaluable in the *diffusion* form by using the set of equations (4.17), (4.18) and (4.11), or, alternatively, in

the *advection* form by using (4.19), (4.18) and (4.21). These expressions are exact being a direct transformation of the Navier Stokes equations.

It is interesting to note the analogy between the *advection* form and the aerodynamic force for inviscid and unbounded flows expressed by equation (3.35).

4.3 High Reynolds number flows

The equations derived in the previous section apply only to velocity fields which are solutions of the Navier Stokes equations. Specifically, the flow field must be a solution at a certain time t in a given volume Ω. In this form, the advantage of theory is restricted to the availability of this kind of data. Conversely, the most common practice is to deal with time average or space filter flow fields. Also in case of experimental measurements, the data storage often occurs by averaging in time the flow velocity. Such processes produce the appearance of the extra terms associated with the mean effects of turbulence. In the following section, we address the effects of such processes on the formulas achieved so far.

4.3.1 Far field theory in the RANS form

By applying the curl operator to the RANS equation (2.17b), we obtain:

$$\frac{\partial \langle \underline{\omega} \rangle}{\partial t} + \underline{\nabla} \times \underline{\nabla} \times (\langle \underline{\omega} \rangle \times \langle \underline{\mathbf{u}} \rangle) = \underline{\nabla} \times \underline{\nabla} \cdot (\underline{\underline{\tau}} + \underline{\underline{\tau}}^t) \tag{4.22}$$

where $\langle \underline{\omega} \rangle = \underline{\nabla} \times \langle \underline{\mathbf{u}} \rangle$. In equation (4.22), the shear stress tensor $\underline{\underline{\tau}}$ is computed by using the mean velocity $\langle \underline{\mathbf{u}} \rangle$. In order to obtain a *far field* form based on the RANS equations, we need to introduce the averaged Lamb vector as

$$\langle \underline{\boldsymbol{l}} \rangle = \langle \underline{\omega} \rangle \times \langle \underline{\mathbf{u}} \rangle + \langle \underline{\boldsymbol{l}}'' \rangle \tag{4.23}$$

where $\langle \underline{\boldsymbol{l}}'' \rangle = \langle \underline{\omega}' \times \underline{\mathbf{u}}' \rangle$, and $\underline{\omega}' = \underline{\nabla} \times \underline{\mathbf{u}}'$. It is easy to show that the mean fluctuating Lamb vector $\langle \underline{\boldsymbol{l}}'' \rangle$ is related to the Reynolds stress tensor $\underline{\underline{\tau}}^t$, as

shown by Wu et al. in [76]. In fact, by the definition, we have:

$$\langle \underline{\boldsymbol{l}}'' \rangle = \langle \underline{\omega}' \times \underline{\mathbf{u}}' \rangle = \langle (\underline{\nabla} \times \underline{\mathbf{u}}') \times \underline{\mathbf{u}}' \rangle \tag{4.24}$$

Taking into account that for any vector field is:

$$(\underline{\nabla} \times \underline{a}) \times \underline{a} = -\frac{1}{2}\underline{\nabla}\, a^2 + \underline{a} \cdot \underline{\nabla}\, \underline{a} \tag{4.25}$$

we apply this identity to (4.24), obtaining that:

$$\langle \underline{\boldsymbol{l}}'' \rangle = \langle -\frac{1}{2}\underline{\nabla}\, (\underline{\mathbf{u}}' \cdot \underline{\mathbf{u}}') + \underline{\mathbf{u}}' \cdot \underline{\nabla}\, \underline{\mathbf{u}}' \rangle \tag{4.26}$$

Again, by using the property

$$\underline{\nabla}\ \cdot (\underline{\mathbf{u}}\, \underline{\mathbf{u}}) = \underline{\mathbf{u}} \cdot \underline{\nabla}\, \underline{\mathbf{u}} + (\ \underline{\nabla}\ \cdot \underline{\mathbf{u}}\ )\, \underline{\mathbf{u}}$$

and taking into account that $\underline{\nabla}\ \cdot \underline{\mathbf{u}}' = 0$, we have:

$$\langle \underline{\mathbf{u}}' \cdot \underline{\nabla}\, \underline{\mathbf{u}}' \rangle = \langle \underline{\nabla}\ \cdot \underline{\mathbf{u}}' \underline{\mathbf{u}}' \rangle = -\underline{\nabla}\ \cdot \underline{\underline{\tau}}^t \tag{4.27}$$

Namely,

$$\langle \underline{\boldsymbol{l}}'' \rangle = -\underline{\nabla}\ \cdot \underline{\underline{\tau}}^t - \underline{\nabla}\, \kappa \tag{4.28}$$

where $\kappa = \langle \underline{\mathbf{u}}' \cdot \underline{\mathbf{u}}' \rangle/2$ is the turbulent kinetic energy. The curl of $\langle \underline{\boldsymbol{l}}'' \rangle$ is

$$\underline{\nabla} \times \langle \underline{\boldsymbol{l}}'' \rangle = -\underline{\nabla} \times \underline{\nabla}\ \cdot \underline{\underline{\tau}}^t \tag{4.29}$$

This last relation is used to derive the averaged form of the Helmholtz equation. By substituting the equation (4.23) into equation (4.22), we have:

$$\frac{\partial \langle\, \underline{\omega}\, \rangle}{\partial t} + \underline{\nabla} \times \underline{\nabla} \times (\langle\, \underline{\boldsymbol{l}} \rangle - \langle\, \underline{\boldsymbol{l}}'' \rangle) = \underline{\nabla} \times \underline{\nabla}\ \cdot (\underline{\underline{\tau}} + \underline{\underline{\tau}}^t) \tag{4.30}$$

Namely,

$$\frac{\partial \langle\, \underline{\omega}\, \rangle}{\partial t} + \underline{\nabla} \times \langle\, \underline{\boldsymbol{l}} \rangle = \nu \nabla^2 \langle\, \underline{\omega}\, \rangle \tag{4.31}$$

The Helmholtz equation for the average vorticity $\langle\ \underline{\omega}\ \rangle$ takes the same form of the equation (4.6). The non linearity effects of the averaging process are contained in the definition of the average Lamb vector (4.23). By using the

DMT relations, the *far field* form of the aerodynamic force is cast for an averaged flow field as follows:

$$\langle \underline{\mathbf{F}}_{I,d} \rangle = -\int_{\Omega} \underline{\mathbf{r}} \times (\nu \nabla^2 \langle \underline{\omega} \rangle)\, dV + \langle \underline{\mathbf{F}}^{t} \rangle \tag{4.32}$$

$$\langle \underline{\mathbf{F}}_{II} \rangle = -\int_{\Sigma} \underline{\mathbf{r}} \times \underline{n} \times \nu(\underline{\nabla} \times \langle \underline{\omega} \rangle)\, dS + \int_{\Sigma} \nu(\langle \underline{\omega} \rangle \times \underline{n})\, dS - \langle \underline{\mathbf{F}}^{t} \rangle \tag{4.33}$$

where

$$\langle \underline{\mathbf{F}}^{t} \rangle = \int_{\Omega} \underline{\mathbf{r}} \times \underline{\nabla} \times \langle \underline{\boldsymbol{l}}'' \rangle\, dV \tag{4.34}$$

groups the explicit effects of the mean fluctuating turbulent field. Analogously, the *advection* form is derived by using equation (4.31):

$$\langle \underline{\mathbf{F}}_{I,a} \rangle = -\int_{\Omega} \underline{\mathbf{r}} \times \frac{\partial \langle \underline{\omega} \rangle}{\partial t}\, dV - \int_{\Omega} \langle \underline{\boldsymbol{l}} \rangle\, dV - \int_{\partial\Omega} \underline{\mathbf{r}} \times \underline{n} \times \langle \underline{\boldsymbol{l}} \rangle\, dS + \langle \underline{\mathbf{F}}^{t} \rangle \tag{4.35}$$

The body acceleration term $\langle \underline{\mathbf{F}}_{III} \rangle$ is not altered by the averaging process. It results that:

$$\langle \underline{\mathbf{F}}_{III} \rangle = \underline{\mathbf{F}}_{III} \tag{4.36}$$

It can be noted that the term $\langle \underline{\mathbf{F}}^{t} \rangle$ is simultaneously added and subtracted from equations (4.32), (4.33) and (4.35). Namely, the mean aerodynamic force $\langle \underline{\mathbf{F}} \rangle$ given by

$$\langle \underline{\mathbf{F}} \rangle = \langle \underline{\mathbf{F}}_{I,d} \rangle + \langle \underline{\mathbf{F}}_{II} \rangle + \langle \underline{\mathbf{F}}_{III} \rangle$$

or by

$$\langle \underline{\mathbf{F}} \rangle = \langle \underline{\mathbf{F}}_{I,a} \rangle + \langle \underline{\mathbf{F}}_{II} \rangle + \langle \underline{\mathbf{F}}_{III} \rangle$$

does not depend on $\langle \underline{\mathbf{F}}^{t} \rangle$. The final expression of averaged aerodynamic force is formally similar to the original form derived by Wu for the Navier Stokes equations.

4.3.2 Dimensional analysis

A discussion on the orders of magnitude is reported. First, a uniform dimensionalization based on some reference quantities is considered. In particular, by fixing a velocity and a length of reference,

$$U_r, L_r$$

and defining the reference Reynolds number $Re = U_r L_r/\nu$, the non dimensional form of equations (4.17), (4.18), (4.20) and (4.21) is obtained:

$$\underline{\mathbf{F}}^*_{I,\,d} = -\frac{1}{Re_r}\int_{\Omega^*}\left(\underline{\mathbf{r}}^* \times \nabla^2\underline{\omega}^*\right) dV^* \tag{4.37}$$

$$\underline{\mathbf{F}}^*_{I,\,a} = -\int_{\Omega^*}\left(\underline{\mathbf{r}}^* \times \frac{\partial\underline{\omega}^*}{\partial t^*}\right) dV^* - \int_{\Omega^*}\underline{\boldsymbol{l}}^*\, dV^* - \int_{\partial\Omega^*}\underline{\mathbf{r}}^* \times (\underline{n} \times \underline{\boldsymbol{l}}^*)\, dS^* \tag{4.38}$$

$$\underline{\mathbf{F}}^*_{II} = -\frac{1}{Re_r}\int_{\Sigma^*}\Big(\underline{\mathbf{r}}^* \times [\underline{n} \times (\underline{\nabla} \times \underline{\omega}^*)]\Big) dS^* + \frac{1}{Re_r}\int_{\Sigma^*}(\underline{\omega}^* \times \underline{n})\, dS^* \tag{4.39}$$

$$\underline{\mathbf{F}}^*_{III} = \int_{\partial B^*}\underline{\mathbf{r}}^* \times (\underline{n} \times \underline{\mathbf{a}}^*)\, dS^* \tag{4.40}$$

where * indicates the non dimensional quantities. The non dimensional aerodynamic force $\underline{\mathbf{F}}^*$ is given by $\underline{\mathbf{F}} = U_r^2 L_r^2\, \underline{\mathbf{F}}^*$. It is worth noting that the reference Reynolds number appears only in the expression of $\underline{\mathbf{F}}^*_{I,\,d}$ and $\underline{\mathbf{F}}^*_{II}$. The *advection* form , even if is equivalent to the *diffusion* form , does not depend on the Reynolds number explicitly.

Steady laminar boundary layer analysis

In case of a two dimensional steady and laminar boundary layer flow ($Re \gg 1$), the classical analysis of the order of magnitude of the different terms can be performed by choosing a different scaling for the stream wise and the normal wise directions. By indicating with x and y the stream-wise and the normal wall directions, we introduce $\bar{y} = y/(\delta L_r)$ and $\bar{v} = v/(\delta U_r)$, where $\delta \approx 1/\sqrt{Re}$ is the length scale of the boundary layer [77]. In a two dimensional flow like the boundary layer, the vorticity $\underline{\omega}$ is $\omega\underline{k}$ with ω given

by :

$$\omega = \frac{\partial v}{\partial y} - \frac{\partial u}{\partial y} = \frac{U_r}{L_r}\left(\delta\frac{\partial \bar{v}}{\partial x^*} - \frac{1}{\delta}\frac{\partial u^*}{\partial \bar{y}}\right) \approx -\frac{U_r}{\delta L_r}\frac{\partial u^*}{\partial \bar{y}}$$

By calculating the integrand functions of the equation (4.17), we have:

$$\begin{aligned}
\underline{\mathbf{r}} \times \nabla^2\underline{\omega} &= (y\underline{i} - x\underline{j})\left(\frac{\partial^2\omega}{\partial x^2} + \frac{\partial^2\omega}{\partial y^2}\right) = \\
&= (x\underline{j} - y\underline{i})\left(\frac{\partial^3 u}{\partial x^2\partial y} + \frac{\partial^3 u}{\partial y^3}\right) = \\
&= \frac{U_r}{L_r^2}\left(\frac{1}{\delta}\, x^*\underline{j} - \bar{y}\,\underline{i}\right)\left(\frac{\partial^3 u^*}{\partial x^{*2}\partial \bar{y}} + \frac{1}{\delta^2}\frac{\partial^3 u^*}{\partial \bar{y}^3}\right)
\end{aligned}$$

Taking into account that $dV = L_r^3\,\delta\,dV^*$ and $\nu = U_r L_r \delta^2$ we obtain that:

$$\nu(\,\underline{\mathbf{r}} \times \nabla^2\underline{\omega}\,)dV = L_r^2\,U_r^2\,(\delta^2 x^*\underline{j} - \delta^3\,\bar{y}\,\underline{i})\left(\frac{\partial^3 u^*}{\partial x^{*2}\partial \bar{y}} + \frac{1}{\delta^2}\frac{\partial^3 u^*}{\partial \bar{y}^3}\right)dV^*$$

Thus, the component along the stream wise direction is given by:

$$\underline{\mathbf{F}}^*_{I,\,d}\cdot\underline{i} = \delta\int_{\Omega^*}\bar{y}\frac{\partial^3 u^*}{\partial \bar{y}^3}dV^* + O(\delta^3) \tag{4.41}$$

whereas the normal wise component is:

$$\underline{\mathbf{F}}^*_{I,\,d}\cdot\underline{j} = -\int_{\Omega^*} x^*\frac{\partial^3 u^*}{\partial \bar{y}^3}dV^* + O(\delta^2) \tag{4.42}$$

Concerning the *advection* form integrals expressed in equation (4.20), we need to compute the Lamb vector for a laminar boundary layer. It results:

$$\underline{\boldsymbol{l}} = \underline{\omega}\times\underline{\mathbf{u}} = \frac{U_r^2}{L_r}\frac{\partial u^*}{\partial \bar{y}}(\bar{v}\underline{i} - \frac{1}{\delta}u^*\underline{j})$$

and

$$\underline{\boldsymbol{l}}\,dV = L_r^2\,U_r^2\,\frac{\partial u^*}{\partial \bar{y}}(\,\delta\,\bar{v}\,\underline{i} - u^*\,\underline{j}\,)\,dV^*$$

The moment of the Lamb vector is given by:

$$\underline{\mathbf{r}}\times\underline{n}\times\underline{\boldsymbol{l}} = -U_r^2\frac{\partial u^*}{\partial \bar{y}}\left(\frac{1}{\delta}u^* n_x + n_y\bar{v}\right)\left(\delta\,\underline{i}\,\bar{y} - \underline{j}\,x^*\,\right)$$

The surface element dS is expressed in the non dimensional form as $dS = \delta L_r^2 dS^*$. Thus:

$$(\underline{\mathbf{r}} \times \underline{n} \times \underline{\boldsymbol{l}})\, dS = -L_r^2 U_r^2 \frac{\partial u^*}{\partial \bar{y}} \left(u^* n_x + n_y \delta \bar{v}\right) \left(\delta\, \underline{i}\, \bar{y} - \underline{j}\, x^* \right) dS^*$$

Then, the *advection* form integrals in a boundary layer are:

$$\underline{\mathbf{F}}^*_{I,\,a} \cdot \underline{i} = -\delta \left(\int_{\Omega^*} \bar{v}\, \frac{\partial u^*}{\partial \bar{y}}\, dV^* + \int_{\Sigma^*} \bar{y}\, u^* \frac{\partial u^*}{\partial \bar{y}}\, n_x\, dS^* \right) + O(\delta^2) \tag{4.43}$$

$$\underline{\mathbf{F}}^*_{I,\,a} \cdot \underline{j} = \left(\int_{\Omega^*} u^* \frac{\partial u^*}{\partial \bar{y}}\, dV^* - \int_{\Sigma^*} x^* u^* \frac{\partial u^*}{\partial \bar{y}} n_x dS^* \right) + O(\delta) \tag{4.44}$$

Finally, we estimate the integral $\underline{\mathbf{F}}_{II}$. The curl of the vorticity is:

$$\underline{\nabla} \times \underline{\omega} = \frac{U_r}{\delta L_r^2} \left(\underline{j}\, \frac{\partial^2 u^*}{\partial x^* \partial \bar{y}} - \underline{i}\, \frac{1}{\delta}\, \frac{\partial^2 u^*}{\partial \bar{y}^2} \right)$$

It follows that:

$$\underline{\mathbf{r}} \times \underline{n} \times \nu(\underline{\nabla} \times \underline{\omega}) dS = \; L_r^2\, U_r^2\, \delta \left(n_x \delta \frac{\partial^2 u^*}{\partial x^* \partial \bar{y}} + n_y\, \frac{\partial^2 u^*}{\partial \bar{y}^2} \right) (\underline{i}\, \bar{y}\, \delta - \; \underline{j}\, x^*) dS^*$$

and

$$\nu\, \underline{\omega} \times \underline{n}\, dS = \; L_r^2\, U_r^2 \delta^2\, \frac{\partial u^*}{\partial \bar{y}} (n_y\, \underline{i} - n_x\, \underline{j}) dS^*$$

Then,

$$\underline{\mathbf{F}}^*_{II} \cdot \underline{i} = \delta^2 \int_{\Sigma^*} \left(-\frac{\partial^2 u^*}{\partial \bar{y}^2} \bar{y} + \frac{\partial u^*}{\partial \bar{y}} \right) n_y dS^* + O(\delta^3) \tag{4.45}$$

$$\underline{\mathbf{F}}^*_{II} \cdot \underline{j} = \delta \int_{\Sigma^*} \frac{\partial^2 u^*}{\partial \bar{y}^2} x^*\, n_y\, dS^* + O(\delta^2) \tag{4.46}$$

By resuming, we have obtained that:

This dimensionalization provides that the integral $\underline{\mathbf{F}}_{II}$ is negligible with respect to $\underline{\mathbf{F}}_I$ for both the x and y components. For high Reynolds number and wall bounded flows, the aerodynamic force is valued only in terms of $\underline{\mathbf{F}}_I$.

	$\underline{\mathbf{F}}^*_{I,\,d}$	$\underline{\mathbf{F}}^*_{I,\,a}$	$\underline{\mathbf{F}}^*_{II}$
$\underline{i}$	$O(\delta)$	$O(\delta)$	$O(\delta^2)$
$\underline{j}$	$O(1)$	$O(1)$	$O(\delta)$

Turbulent boundary layer analysis

In case of a turbulent boundary layer on a wall, the previous analysis still holds for the mean flow quantities, by considering $\delta = Re^{-\beta}$, with $\beta > 1/2$ [77]. The additional term $\langle\, \underline{\mathbf{F}}^t \,\rangle$ in general is not negligible. By expressing the integral (4.34) in terms of the Reynolds stress tensor, we have:

$$\langle\, \underline{\mathbf{F}}^{\,t} \,\rangle = \int_\Sigma \underline{\mathbf{x}} \times \underline{n} \times (\underline{\nabla} \cdot \underline{\underline{\tau}}^t)\, dS + \int_\Sigma \underline{\underline{\tau}}^t \cdot \underline{n}\, dS \tag{4.47}$$

In a turbulent boundary layer only the derivatives of the shear stress components τ^t_{xy} have the same order of magnitude of the mean quantities (see Pope [59] p.114). Thus, within this approximation:

$$\left[\underline{\mathbf{r}} \times (\underline{n} \times \underline{\nabla} \cdot \underline{\underline{\tau}}^t)\right]_x \;\approx\; -\,\bar{y}\, n_y\, \frac{\partial\, \tau^t_{xy}}{\partial\, \bar{y}} \tag{4.48}$$

$$\left[\underline{\mathbf{r}} \times (\underline{n} \times \underline{\nabla} \cdot \underline{\underline{\tau}}^t)\right]_y \;\approx\; x\, n_y\, \frac{\partial\, \tau^t_{xy}}{\partial\, \bar{y}} \tag{4.49}$$

while the terms $\underline{\underline{\tau}}^t \cdot \underline{n}$ results negligible. As a consequence, the integral (4.47) reduces to:

$$\langle\, \underline{\mathbf{F}}^{\,t} \,\rangle \;\approx\; \int_\Sigma \frac{\partial\, \tau^t_{xy}}{\partial\, y}\, n_y \left(y\, \underline{i} - x\, \underline{j}\right) dS \tag{4.50}$$

It is worth noting that this contribution is not negligible, but is zero on Σ when $n_y = 0$.

4.3.3 Some remarks

In a practical application the *diffusion* form has the advantage that all integrals can be computed by means of the average vorticity $\langle\, \underline{\omega} \,\rangle$ only. An

important drawback is the involvement of the third spatial derivatives of the velocity field which are more difficult to compute accurately. On the contrary, the *advection* form requires the first order spatial derivatives of the velocity. In addition, the *advection* form allows to recognize the explicit role of vortex force. For these reasons such form will be adopted.

The computation of the aerodynamic force using the sum $\langle \underline{\mathbf{F}}_{I,a} \rangle + \langle \underline{\mathbf{F}}_{II} \rangle + \langle \underline{\mathbf{F}}_{III} \rangle$ does not require the explicit knowledge of $\langle \underline{\mathbf{F}}^t \rangle$. However, the Reynolds stress tensor $\underline{\underline{\tau}}^t$ and turbulent kinetic energy κ are involved in the computation of $\langle \underline{\boldsymbol{l}} \rangle$ by equations (4.23) and (4.28). An alternative way is to compute $\langle \underline{\mathbf{F}}_{I,a} \rangle$ in terms of the mean velocity $\langle \underline{\mathbf{u}} \rangle$ and vorticity $\langle \underline{\omega} \rangle$ as follows:

$$\begin{aligned} \langle \underline{\mathbf{F}}_{I,a} \rangle &= -\int_{\Omega} \underline{\mathbf{r}} \times \frac{\partial \langle \underline{\omega} \rangle}{\partial t} \, dV - \int_{\Omega} \langle \underline{\omega} \rangle \times \langle \underline{\mathbf{u}} \rangle \, dV \\ &- \int_{\partial\Omega} \underline{\mathbf{r}} \times \underline{n} \times (\langle \underline{\omega} \rangle \times \langle \underline{\mathbf{u}} \rangle) \, dS \end{aligned} \tag{4.51}$$

The *advection* form is correctly computed by using the equation (4.51), but, as a consequence, the need to calculate $\langle \underline{\mathbf{F}}^t \rangle$ in $\langle \underline{\mathbf{F}}_{II} \rangle$ now arises. The analysis of the orders of magnitude, previously conducted, allows to neglect these contributions for high Reynolds and wall bounded flows.

The 2D *advection* form (4.51) and the body surface contribution (4.36) can be explicated in an orthogonal cartesian reference system Oxy. The expressions of lift and drag coefficients are obtained by assuming the x axis parallel to the free stream velocity U_∞, and dividing by $U_\infty^2 c/2$. By specializing the *advection* form (4.35) and the body surface contribution (4.36), we have $\underline{\mathbf{r}} = (x, y)$, $\underline{n} = (n_x, n_y)$, $\langle \underline{\mathbf{u}} \rangle = (\langle u \rangle, \langle v \rangle)$, $\langle \underline{\omega} \rangle = \langle \omega \rangle \underline{k}$. The lift and drag coefficients are expressed as:

$$C_l = (C_l)_{\Omega} + (C_l)_{\dot{\omega}} + (C_l)_{\Sigma} + (C_l)_{B} \tag{4.52a}$$

$$C_d = (C_d)_{\Omega} + (C_d)_{\dot{\omega}} + (C_d)_{\Sigma} + (C_d)_{B} \tag{4.52b}$$

where

$$(C_l)_{\,\Omega} = -2\int_{\Omega} \langle\, \omega \,\rangle \, \langle\, u \,\rangle \, dV \tag{4.53a}$$

$$(C_l)_{\,\dot{\omega}} = 2\int_{\Omega} x \, \langle\, \dot{\omega} \,\rangle \, dV \tag{4.53b}$$

$$(C_l)_{\,\Sigma} = 2\int_{\Sigma} x \, \langle\, \omega \,\rangle \, (\langle\, \underline{\mathbf{u}} \,\rangle \cdot \underline{n}) \, dS \tag{4.53c}$$

$$(C_l)_{\,B} = -2\int_{\partial B} x \, a_B \, dS \tag{4.53d}$$

and

$$(C_d)_{\,\Omega} = 2\int_{\Omega} \langle\, \omega \,\rangle \, \langle\, v \,\rangle \, dV \tag{4.54a}$$

$$(C_d)_{\,\dot{\omega}} = -2\int_{\Omega} y \, \langle\, \dot{\omega} \,\rangle \, dV \tag{4.54b}$$

$$(C_d)_{\,\Sigma} = -2\int_{\Sigma} y \, \langle\, \omega \,\rangle \, (\langle\, \underline{\mathbf{u}} \,\rangle \cdot \underline{n}) \, dS \tag{4.54c}$$

$$(C_d)_{\,B} = 2\int_{\partial B} y \, a_B \, dS \tag{4.54d}$$

In the formulas (4.53) and (4.54), $a_B = |\underline{n} \times (\underline{\mathbf{a}} - \underline{\boldsymbol{l}})|$, and $\langle\, \dot{\omega} \,\rangle$ is the time derivative of $\langle\omega\rangle$. In case of unsteady periodic RANS solutions, the quantities in above equations must be considered as phase averages, which are the direct outcome of the unsteady RANS based CFD solvers.

4.4 Applications

The verification and the numerical validation of the present *far field* theory is carried out by the analysis of several steady RANS solutions past an airfoil at high Reynolds number.

4.4.1 Steady RANS solutions

A two dimensional C-type structured grid around the NACA0012 airfoil has been created with 768×200 cells in stream wise and normal wise directions respectively. The outer boundary is located at a distance of about $30c$ from

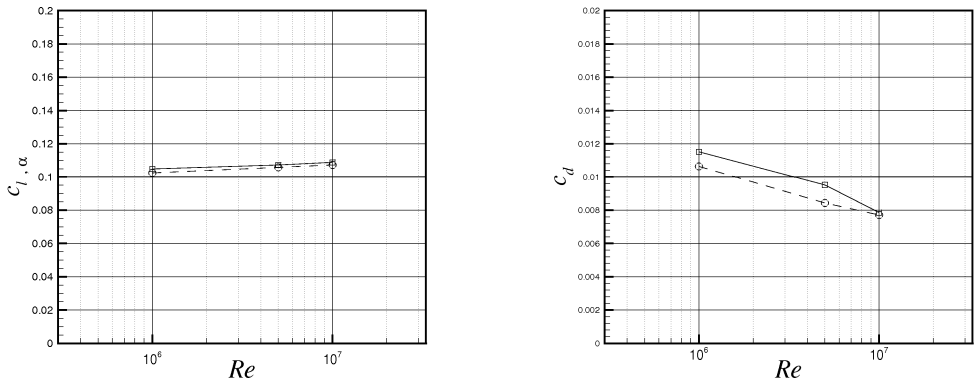

(a) (b)

Figure 4.2: Steady turbulent flow solutions at Reynolds numbers 10^6, $5 \cdot 10^6$ and 10^7. Comparisons with the experimental data of McCroskey [78]. (a) $C_{l\alpha}$; (b) C_d at $\alpha = 0°$.

the airfoil surface. The wake edge is discretized with 128 cells. The airfoil surface has 512 cells. Standard free stream boundary conditions have been set on the outer boundary. Three Reynolds numbers have been investigated, $Re = 10^6$, 5×10^6, and 10^7 at angles of attack within the range $0° \leq \alpha \leq 6°$. The TNT turbulence model has been used. The first cell size along the wall normal direction on the airfoil surface has been accomodated to mantain the y^+ of the order one at each Reynolds number. As a reference, the $C_{l\alpha}$ and the C_d at $\alpha = 0°$ obtained from the standard *near field* integration are compared with some experimental data reported in literature, [78]. In figures (4.2a) and (4.2b), the $C_{l\alpha}$ and the C_d at $\alpha = 0°$ are plotted as function of the Reynolds number. A good agreement is achieved confirming the reliability of the present CFD data.

4.4.2 Far Field analysis of steady RANS solutions

The *far field* form of the aerodynamic force expressed by equations (4.52) does not dependent on the volume Ω selected for the integral calculation. Nevertheless some dependencies are expected when we deal with the numerical solutions. Furthermore, the single contributions can vary according to the

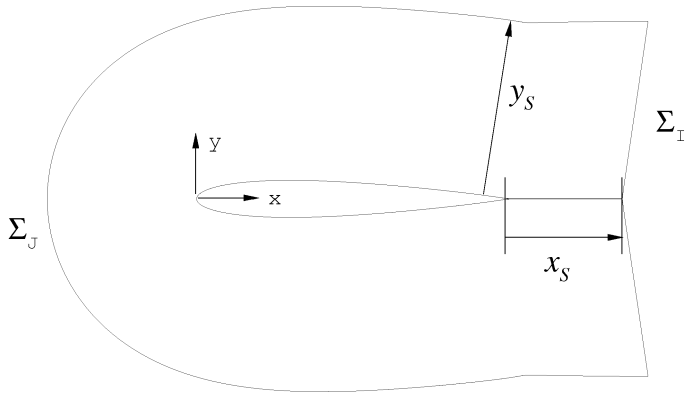

Figure 4.3: Selection of the domain used for the *far field* integration.

position assumed by the surface Σ in the flow field. An integration domain Ω based on a typical computational grid for CFD calculations is proposed in figure (4.3). The surface Σ is defined as $\Sigma_I \cup \Sigma_J$ by fixing some grid lines. The surface Σ_I intersects the airfoil wake at a distance x_S from the trailing edge while the surface Σ_J is located at y_S from the solid surface. In the following, the normalized aerodynamic coeffiecients, $(C_l)^*$ and $(C_d)^*$, defined as the ratio of the *far field* coefficient by the corresponding *near field* one, are used:

$$(C_l)^* = \frac{(C_l)_{Farfield}}{(C_l)_{Nearfield}} \quad ; \quad (C_d)^* = \frac{(C_d)_{Farfield}}{(C_d)_{Nearfield}}$$

where the superscript $*$ specifies the normalization operation.

Effects of the Σ_I location on C_l

In figure (4.4a), the normalized lift coefficients $(C_l)^*$ are reported for several Reynolds numbers and angles of attack by increasing the x_S location of the Σ_I surface from zero to $25c$ downstream the airfoil. The Σ_J surface is located at about $15c$ from the airfoil surface ($y_S \simeq 15c$). The contributions related to the volume integral $(C_l)^*_\Omega$ are reported in figure (4.4b). The surface contributions, $(C_l)^*_{\Sigma_I}$ and $(C_l)^*_{\Sigma_J}$, are plotted separately in figures (4.4c)

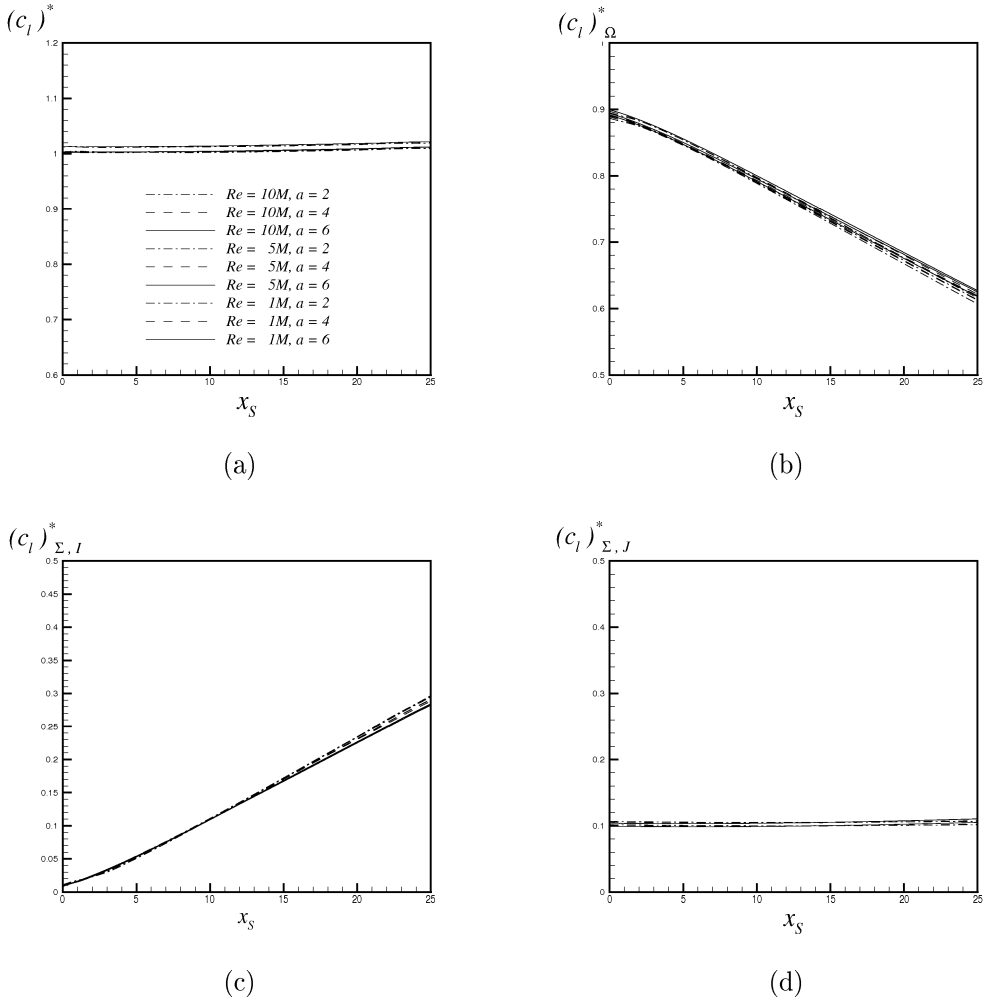

Figure 4.4: Steady turbulent flow solutions at $Re = 10^6$, $5 \cdot 10^6$ and 10^7, angles of attack $\alpha = 2°$, $4°$ and $6°$. Normalized contributions of the lift coefficients by varying x_S: (a) $(C_l)^*$; (b) $(C_l)^*_\Omega$; (c) $(C_l)^*_{\Sigma_I}$; (d) $(C_l)^*_{\Sigma_J}$.

and (4.4d). Although the curves refer to different α and Reynolds numbers, no significant dependency on these parameters is visible. The $(C_l)^*$ is ≈ 1 within a narrow band of 2% while the vortex force contribution $(C_l)^*_\Omega$ and $(C_l)^*_{\Sigma_I}$ vary linearly compensating each other. A constant term is obtained from the surface integral on Σ_J. The variation of $(C_l)^*_{\Sigma_I}$ with x_S is an effect of the external boundary conditions on the lift. This aspect can be explained

considering the analytical expression of $(C_l)_{\Sigma_I}$, which is:

$$(C_l)_{\Sigma_I} = 2 \int_{\Sigma_I} x\, \omega\, u\, dS$$

The wake is intersected by Σ_I at a distance x_S from the trailing edge. This integral can be calculated by exploiting the boundary layer approximation of the vorticity, i.e. $\omega = -\frac{\partial u}{\partial y}$. Thus, the intregral on Σ_I becomes:

$$(C_l)_{\Sigma_I} = -2 \int_{\Sigma_I} x\, \frac{\partial u}{\partial y}\, u\, dS = -x_S \int_{\Sigma_I} \frac{\partial u^2}{\partial y}\, dS = -x_S \Big[u^2(x_S, y_S) - u^2(x_S, -y_S) \Big]$$

For y_S greater than the wake thickness, the Bernoulli equation provides a relation between the velocity and pressure:

$$(C_l)_{\Sigma_I} = -x_S \Big[-p(x_S, y_S) + p(x_S, -y_S) \Big]$$

The slope of $(C_l)_{\Sigma_I}$ is given by:

$$\frac{d(C_l)_{\Sigma_I}}{d\, x_S} = p(x_S, y_S) - p(x_S, -y_S)$$

For $y_S \to \infty$ the flow takes the real free stream conditions and $p(x_S, y_S) \to p_\infty$. As a consequence,

$$\frac{d(C_l)_{\Sigma_I}}{d\, x_S} = 0$$

When y_S is limited, and $p(x_S, y_S) \neq p(x_S, -y_S)$, $(C_l)_{\Sigma_I}$ grows linearly. This effect reflects also on $(C_l)_\Omega$. The linear behaviour is visible in figures (4.4b) and (4.4c). With a more extended CFD domain of about $100c$, it has been proved that the surface contributions $(C_l)^*_{\Sigma_I}$ and $(C_l)^*_{\Sigma_J}$ vanish and $(C_l)^*_\Omega \approx 1$. In figure (4.5a) it is shown a plot of $(C_l)^*_{\Sigma_I}$ obtained by moving the far field boundary at a distance $y_S = 50c$. It is visible a significant reduction in the slope with respect to the case $y_S = 15c$. In figure (4.5b) the contribution $(C_l)^*_{\Sigma_J}$ vanishes as the distance y_S of the external boundary from the body increases.

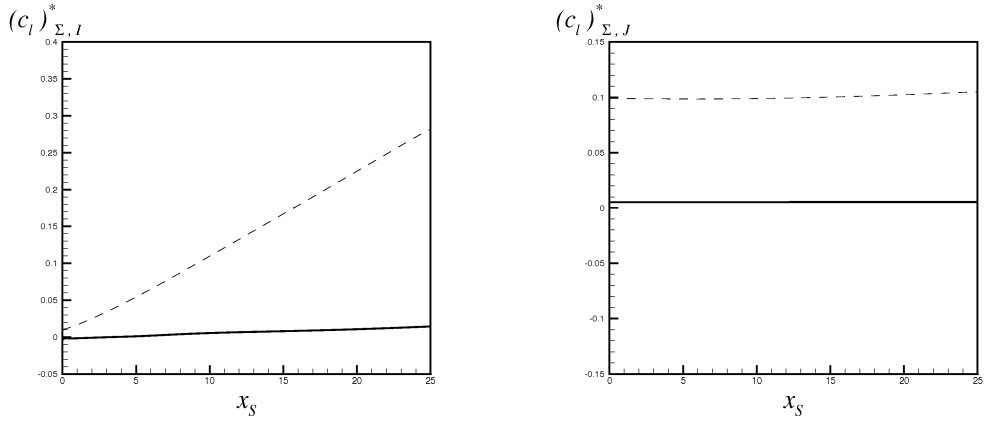

(a) (b)

Figure 4.5: Steady turbulent flow solutions at $Re = 10^7$ and angle of attack $\alpha = 6°$. Normalized contributions of the lift coefficients by varying the outer boundary distance. —, $y_S = 50c$; $--$, $y_S = 15c$. (a), $(C_l)^*_{\Sigma_I}$; (b), $(C_l)^*_{\Sigma_J}$.

Effects of the Σ_I location on C_d

In figure (4.6a) the normalized drag coefficients at $\alpha = 0°$ are reported. The drag coefficient, computed by the formula (4.52), agrees with the *near field* data up to $x_S \approx 10c$. The 25 % of uncertainty on the normalized drag coefficient is equivalent to about 30 drag counts at Reynolds 10^6 , and to 19 drag counts at Reynolds 10^7. The volume contribution $(C_d)_{\Omega} \to 0$ as x_S increases, figure (4.6b), and the main part of the drag remains associated with the surface contribution $(C_d)_{\Sigma_I}$, as shown in figure (4.6c). The contribution $(C_d)_{\Sigma_J}$, (figure 4.6d), provides a constant term. As $x_S \to \infty$, it is possible to proof that $(C_d)_{\Sigma_I}$ reduces to the well known formula of the viscous drag [79], as already shown by J.C. Wu [73] in 1981. In fact, by assuming a boundary layer approximation, in the far wake it is possible to put $u \approx 1 - u'$ where $u' \ll 1$ is the flow defect,

$$\begin{aligned}(C_d)_{\Sigma_I} &= -2\int_{\Sigma_I} y\,\omega\,u\,dS = \int_{\Sigma_I} y\,\frac{\partial u^2}{\partial y}\,dS = \Big[u^2 y\Big]_{-y_S}^{+y_S} - \int_{-y_S}^{+y_S} u^2 dy \\ &= 2y_S - \int_{-y_S}^{+y_S}(1-2u')dy = 2\int_{-y_S}^{+y_S} u'dy = 2\theta \end{aligned} \tag{4.55}$$

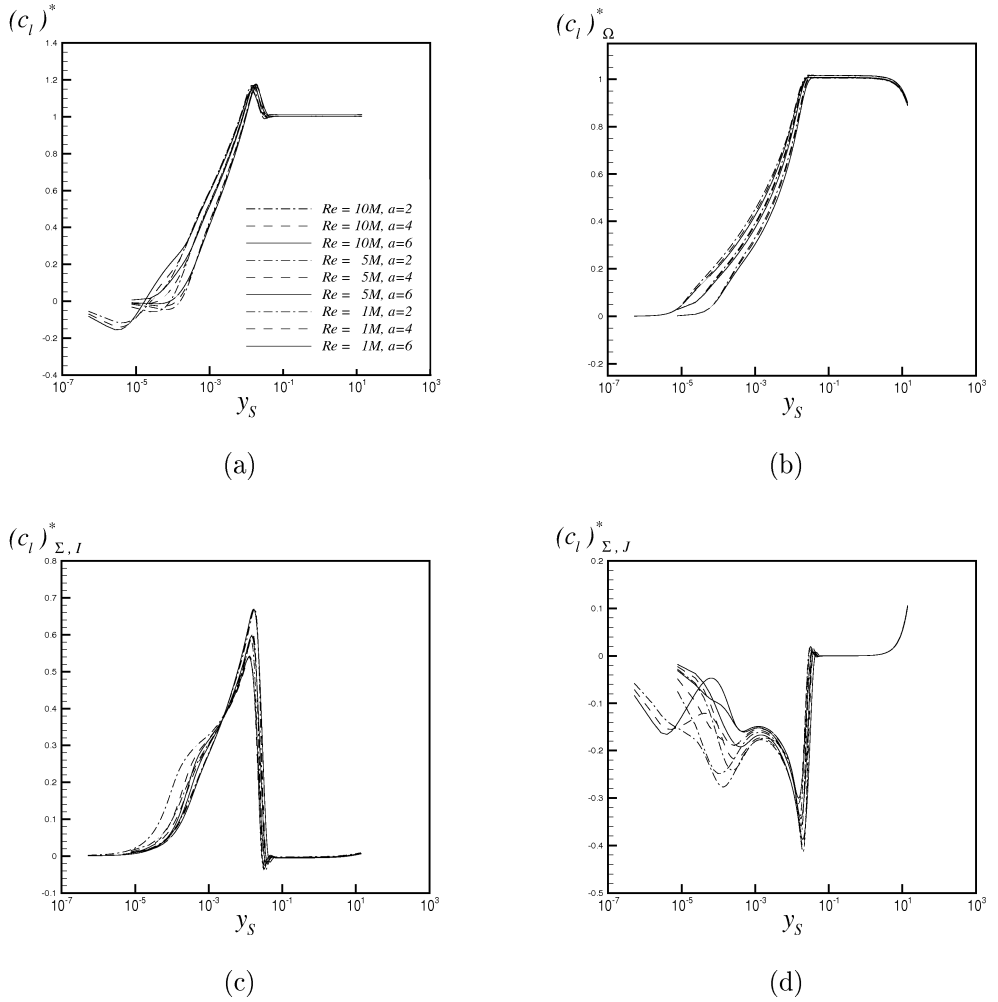

Figure 4.6: Steady turbulent flow solutions at $\alpha = 0°$. Normalized contributions of the drag coefficients by varying x_S. $-\cdot-$, $Re = 10^6$; $--$, $Re = 5 \cdot 10^6$; —, $Re = 10^7$. (a), $(C_d)^*$; (b), $(C_d)^*_{\Omega}$; (c), $(C_d)^*_{\Sigma_I}$; (d), $(C_d)^*_{\Sigma_J}$.

where θ is the displacement thickness of the wake. As a consequence, when Σ_I is located far in the wake, the drag coefficient accuracy is mainly affected by the quality of the CFD solution, which is usually not sufficient after few chords downstream in the wake.

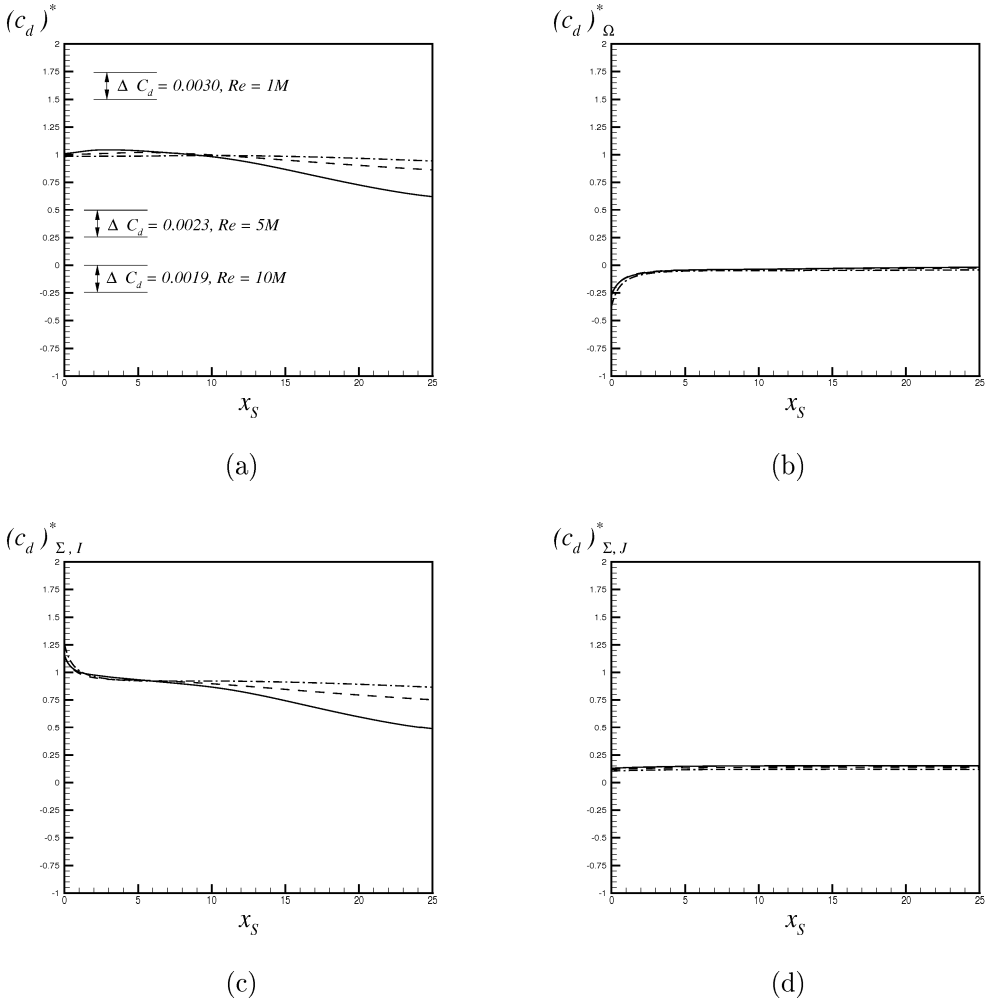

Figure 4.7: Steady turbulent flow solutions at $Re = 10^6$, $5 \cdot 10^6$ and 10^7, angles of attack $\alpha = 2°$. $4°$ and $6°$. Normalized contributions of the lift coefficients by varying y_S. (a), $(C_l)^*$; (b), $(C_l)^*_\Omega$; (c), $(C_l)^*_{\Sigma_I}$; (d), $(C_l)^*_{\Sigma_J}$.

Effects of the Σ_J location on C_l

The effects on the *far field* aerodynamic coefficients are analyzed by varying the location y_S of the surface Σ_J. The Σ_I surface is fixed at $x_S = 0.004$ just after the trailing edge airfoil. In figure (4.7a), the lift coefficient contributions (4.52a) are reported as function of y_S. The logarithmic scale is used to highlight the turbulent viscous layer. The integrals converge toward the *near field* values for y_S greater than the boundary layer thickness. No dependency

is visible upon α and Re. once the convergence is achieved. It has also to be noted, in figure (4.7b), that for y_S greater than the boundary layer thickness, $(C_l)^*_\Omega \to 1$, whereas, in figures (4.7c) and (4.7d), the normalized surface contributions $(C_l)^*_{\Sigma_I}$ and $(C_l)^*_{\Sigma_J} \to 0$. For $y_S > 10c$ an effect of the numerical boundary conditions is visible on $(C_l)^*_\Omega$ and $(C_l)^*_{\Sigma_J}$. For $y_S \leq 10^{-1}c$, large overshoots are obtained because of the neglected terms associated with the turbulent and laminar shear stress components.

Effects of the Σ_J location on C_d

The diagrams of the drag coefficients are reported in figures (4.8a), (4.8b), (4.8c) and (4.8d). The C_d contributions are correctly computed by increasing the distance y_S beyond the boundary layer. It can also be noted that for the selected domain the surface contribution $(C_d)^*_{\Sigma_I}$ tends to 1.45, and $(C_d)^*_\Omega \to -0.55$. These singular values depend on the distance of the surface Σ_I from the airfoil as already seen from the C_d diagrams in figures (4.6).

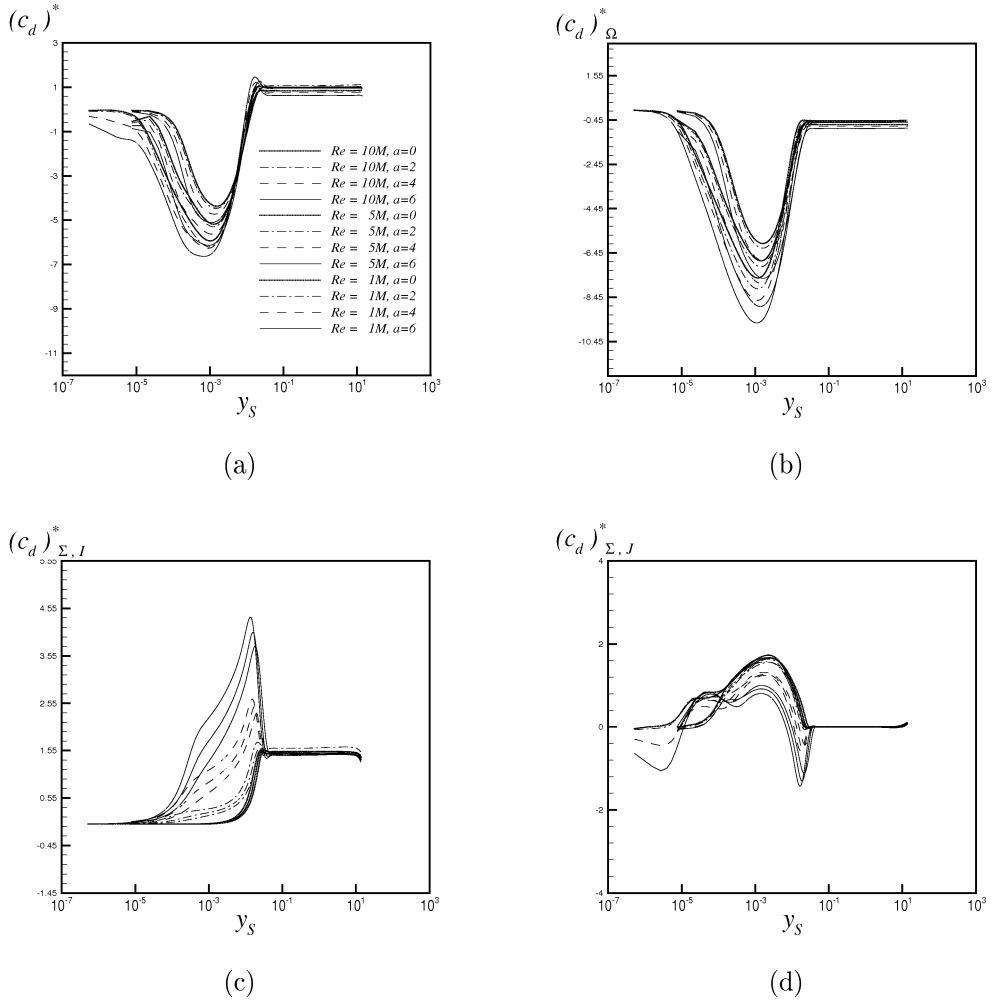

Figure 4.8: Steady turbulent flow solutions at $Re = 10^6$, $5 \cdot 10^6$ and 10^7 angles of attack: $\alpha = 0°$, $\alpha = 2°$, $4°$ and $6°$. Normalized contributions of the drag coefficients by varying y_S. (a), $(C_d)^*$; (b), $(C_d)^*_\Omega$, (c), $(C_d)^*_{\Sigma_I}$; (d), $(C_d)^*_{\Sigma_J}$.

Convergence of the *far field* method towards the *near field*

The analysis of the previous sections has been carried out by using the aerodynamic coefficients expressed by (4.52), and by neglecting the terms associated with $\langle \underline{\mathbf{F}}_{II} \rangle$. We analyze the behaviour of the *far field* when Σ_J intersects the turbulent boundary layer. In such a case, the relative weight of $\langle \underline{\mathbf{F}}_{II} \rangle$ increases as $\Sigma \to \partial B$, and the Lamb vector integrals vanish. First, we verify the consistency of $\langle \underline{\mathbf{F}}_{II} \rangle$ with the *near field* form (4.1) by expressing the

equation (4.33) in terms of the divergence of the shear stress tensor:

$$\langle \underline{\mathbf{F}}_{II} \rangle = \int_{\Sigma} \underline{\mathbf{r}} \times \underline{n} \times \underline{\nabla} \cdot \underline{\underline{\tau}}\, dS + \int_{\Sigma} \underline{\underline{\tau}} \cdot \underline{n}\, dS - \langle \underline{\mathbf{F}}^{t} \rangle$$

The integral $\langle \underline{\mathbf{F}}^{t} \rangle$ can be cast as:

$$\begin{aligned} \langle \underline{\mathbf{F}}^{t} \rangle &= \int_{\Omega} \underline{\mathbf{r}}\underline{\nabla} \times \rho \langle \underline{\boldsymbol{l}}'' \rangle dV = -\int_{\Omega} \underline{\mathbf{r}} \times \underline{\nabla} \times \underline{\nabla} \cdot \underline{\underline{\tau}}^{t} dV = \\ &= -\int_{\Omega} \underline{\nabla} \cdot \underline{\underline{\tau}}^{t} dV - \int_{\Sigma} \underline{\mathbf{r}} \times \underline{n} \times \underline{\nabla} \cdot \underline{\underline{\tau}}^{t} dS \\ &= -\int_{\Sigma} \underline{\underline{\tau}}^{t} \cdot \underline{n} - \int_{\Sigma} \underline{\mathbf{r}} \times \underline{n} \times \underline{\nabla} \cdot \underline{\underline{\tau}}^{t} dS \end{aligned}$$

Namely, by grouping the terms,

$$\langle \underline{\mathbf{F}}_{II} \rangle = \underbrace{\int_{\Sigma} \underline{\mathbf{r}} \times \underline{n} \times \underline{\nabla} \cdot (\underline{\underline{\tau}} + \underline{\underline{\tau}}^{t})\, dS}_{A} + \underbrace{\int_{\Sigma} \underline{\underline{\tau}}^{t} \cdot \underline{n}\, dS}_{B} + \underbrace{\int_{\Sigma} \underline{\underline{\tau}} \cdot \underline{n}\, dS}_{C}$$

We note that the part (A) contains the divergence of the laminar and turbulent stress tensors, which are equilibrated by the momentum convective terms and by the pressure gradient. The parts (B) and (C) instead are the direct contribution of the laminar and turbulent shear stresses. When $\Sigma \to \partial B$, the Reynolds stress tensor $\underline{\underline{\tau}}^{t} \approx\to 0$ and,

$$\langle \underline{\mathbf{F}}_{II} \rangle = \int_{\Sigma} \underline{\mathbf{r}} \times \underline{n} \times \underline{\nabla} \cdot \underline{\underline{\tau}}\, dS + \int_{\Sigma} \underline{\underline{\tau}} \cdot \underline{n}\, dS$$

By the momentum equation, we have:

$$\langle \underline{\mathbf{F}}_{II} \rangle = \int_{\Sigma} \underline{\mathbf{r}} \times \underline{n} \times (\langle \underline{\mathbf{u}} \rangle \cdot \underline{\nabla} \langle \underline{\mathbf{u}} \rangle + \underline{\nabla} p)\, dS + \int_{\Sigma} \underline{\underline{\tau}} \cdot \underline{n}\, dS$$

Finally, when $\Sigma \equiv \partial B$,

$$\langle \underline{\mathbf{F}}_{II} \rangle = \int_{\Sigma} \underline{\mathbf{r}} \times \underline{n} \times \underline{\nabla} p\, dS + \int_{\Sigma} \underline{\underline{\tau}} \cdot \underline{n}\, dS$$

and, by the transformation (4.5)

$$\langle \underline{\mathbf{F}}_{II} \rangle = -\int_{\Sigma} p\, \underline{n}\, dS + \int_{\Sigma} \underline{\underline{\tau}} \cdot \underline{n}\, dS$$

The sign is opposite with respect to the standard *near field* form expressed by equation (4.1) because the surface Σ has the normal direction in opposition with respect to ∂B.

We consider an integration domain by fixing $x_S = 0.001$ and by varying the position y_S of the surface Σ_J within the boundary layer thickness. By expressing the coordinate y_S in wall units $y_S^+ = y_S \frac{u_\tau}{\nu}$ where $u_\tau = \sqrt{\frac{\tau_w}{\rho}}$ and

$$\tau_w = \rho\nu \left(\frac{d\langle U \rangle}{dy} \right)_{x = x_S,\, y=0}$$

the role of the terms (A), (B) and (C) is analyzed. In figures (4.9a) and (4.9b) the diagrams of $(C_l)^*$ and $(C_d)^*$ are reported as function of y_S^+ for a case at $Re = 10^6$ and $\alpha = 2°$. The classical regions of a turbulent boundary layer (defined in terms of y^+,[59]) have also been highlighted. The normalized lift and drag coefficients are now correctly computed up to the solid wall. The contribution (A) takes into account the dynamical part of the boundary layer and balances the Lamb vector integral. (A) tends to zero outside the boundary layer and provides the pressure part of the lift and drag at the solid wall. The Reynolds stress tensor term (B) allows to identify the logarithmic layer as well as the end of the turbulent boundary layer. The buffer layer, in which the turbulent fluctuations are the same order of magnitude of the laminar terms, is recognizable as the region in which (B) and (C) compensate each other. Finally, in the viscous sub layer, the dominance of the laminar viscosity is visible. The term (C) provides the viscous part of the lift and drag at the solid wall.

Observations

The effects of the variation of Ω on the computed aerodynamic coefficients has been discussed for several steady RANS solutions around a two dimensional airfoil. It has been shown that the lift coefficient reduces to the Lamb vector volume integral, namely, to the vortex force, by increasing the dimension of Ω. Analogously, the drag coefficient reduces to a surface integral on the

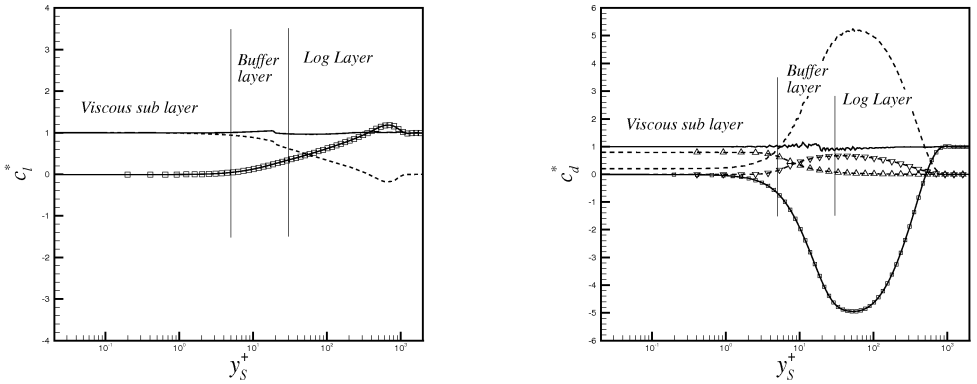

(a) (b)

Figure 4.9: Steady turbulent flow solution at $Re = 10^6$ and $\alpha = 2°$. Normalized contributions of the aerodynamic coefficients as function of y_S^+. —, sum of all contributions; –□–, Lamb vector integrals; – – , (A) $\bigtriangledown$, (B) $\bigtriangleup$, (C); (a) lift coefficients (b) drag coefficients.

wake. Namely,

$$\lim_{(x_S, y_S) \to \infty} (C_l)_{\Omega} = C_l$$
$$\lim_{(x_S, y_S) \to \infty} (C_d)_{\Sigma_I} = C_d$$

This result agrees with the theory developed in chapter 3 for inviscid and unbounded flows. The neglected terms contained in $\underline{\mathbf{F}}_{II}$ have a secondary effect on the aerodynamic force. The substantial difference between the inviscid and viscous theories stems in the way in which the vorticity is created. But, once a distribution of vorticity is achieved, the aerodynamic force is governed by the same physical mechanisms.

Conversely, as Ω collapses to the solid body surface, the equations (4.52) are no longer able to predict the aerodynamic force and the turbulent and viscous terms have to be computed. From a numerical point of view, the most favourable condition has been obtained for $x_S \sim 0$ and y_S greater than the boundary layer thickness. In this way the effects on the aerodynamic force associated with $\langle\, \underline{\mathbf{F}}_{II} \,\rangle$ are avoided.

4.4.3 Inviscid flow applications

In this section, a strategy to compute the aerodynamic force using the *advection* form (4.52) also in case of a numerical solution of the Euler equations is addressed.

An airfoil immersed in an inviscid and steady flow experiences a non zero lift when the circulation is non zero. This points out the presence of vorticity in the field. The absence of physical viscosity constrains to model the vorticity in some way as discussed in chapter 3. The *advection* form of Wu's theory embodies this concept through the Lamb vector, and for this reason is able to predict the aerodynamic force also in case of rotational inviscid flow. However, the application of the *far field* formulation (4.52) to a numerical solution of an inviscid flow is not trivial.

In fact, the numerical solution of the Euler equations does not provide vorticity, and, as a consequence, the *far field* integrals (4.52) applied on a such flow field do not give any lift. A reconstruction of the vortex sheet by considering the Euler solution as a limit process of a Navier Stokes solution for $Re \to \infty$ is tried to overcome this limitation. Batchelor ([69]) proves that the correct Euler limit of a Navier Stokes solution is established by taking first the steady state ($t \to \infty$), and then by decreasing the viscosity to zero. The Lamb vector integral on a volume including such vorticity layer will provide the correct aerodynamic force. The consistency of this concept is first proved analytically and then by a numerical application. Let ε be the normal spacing of the first cell near the solid wall and (s, r) a local coordinate system with s along the body surface and r in the normal direction (opposite to $\underline{n}$), as sketched in the scheme (4.10). For an inviscid flow, the velocity vector $\underline{\mathbf{u}}_1$ in the first cell near the wall at $r = \varepsilon/2$ is parallel to the s direction. By assuming a zero velocity at the wall ($r = 0$), a vorticity layer, extending for $\varepsilon/2$, is created. The vorticity at $r = \varepsilon/4$ is defined as:

$$\underline{\omega}_{\varepsilon/4} = \frac{2\,\underline{\mathbf{u}}_1}{\varepsilon} \times \underline{n} \tag{4.56}$$

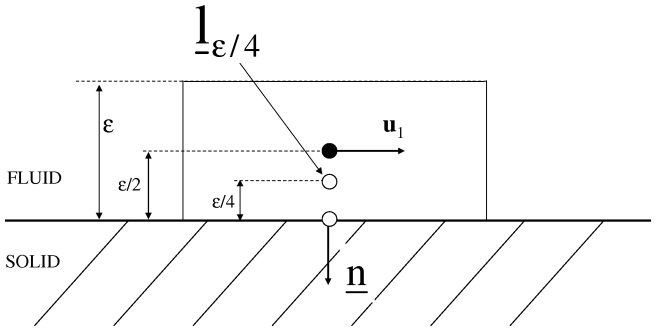

Figure 4.10: Lamb vector definition for an inviscid flow

As a consequence, the Lamb vector at $r = \varepsilon/4$ is:

$$\underline{\boldsymbol{l}}_{\varepsilon/4} = \underline{\omega}_{\varepsilon/4} \times \underline{\mathbf{u}}_{\varepsilon/4} = \left(\frac{2\,\underline{\mathbf{u}}_1}{\varepsilon} \times \underline{n} \right) \times \underline{\mathbf{u}}_{\varepsilon/4} \tag{4.57}$$

where $\underline{\mathbf{u}}_{\varepsilon/4} = 0.5\,\underline{\mathbf{u}}_1$ is the velocity at $r = \varepsilon/4$. Thus, the aerodynamic force is obtained by computing the vortex force in a volume Ω surrounding the solid body, having a thickness $\varepsilon/2$ in r:

$$\begin{aligned} \underline{\mathbf{F}} &= -\int_\Omega \underline{\boldsymbol{l}}_{\varepsilon/4}\, dV = -\int_{\partial B} \left(\int_0^{\varepsilon/2} \left[\left(\frac{2\,\underline{\mathbf{u}}_1}{\varepsilon} \times \underline{n} \right) \times \frac{\underline{\mathbf{u}}_1}{2} \right] ds \right) dr \\ &= \frac{1}{2} \int_{\partial B} [\,\underline{\mathbf{u}}_1 \times (\underline{\mathbf{u}}_1 \times \underline{n})]\, ds = -\int_{\partial B} \frac{\underline{\mathbf{u}}_1 \cdot \underline{\mathbf{u}}_1}{2}\, \underline{n}\, ds \end{aligned}$$

where in the last equality the rule of the double cross product with the assumption that $\underline{\mathbf{u}}_1 \perp \underline{n}$ has been used. Finally, by using the Bernoulli theorem, we have:

$$\underline{\mathbf{F}} = -\int_{\partial B} \frac{\underline{\mathbf{u}}_1 \cdot \underline{\mathbf{u}}_1}{2}\, \underline{n}\, ds = \int_{\partial B} p_1\, \underline{n}\, ds \tag{4.58}$$

Thus, the consistency of equation (4.57) for $\varepsilon \to 0$ is proved by equation (4.58), which is the standard *near field* expression of the aerodynamic force in an inviscid steady flow (see equation (3.8)).

This result has been verified for a numerical inviscid solution around the NACA0012 airfoil at $\alpha = 2°$ and $\alpha = 4°$. In figure (4.11a), the vorticity at the wall computed by using equation (4.57) is plotted versus the airfoil chord for the solution at $\alpha = 4°$ and different mesh size.

As may be seen, the vorticity intensity grows as the grid spacing ratio h decreases. In figure (4.11b), the lift coefficients calculated by refining the grid are reported. These values are computed with both the *near field* formula and equation (4.52). The vortex force converges towards the *near field* result as $h \to 0$.

4.5 Summary

In summary, the present analysis leads to the following observations:

- The theory of Wu was initially developed for flows governed by the unsteady Navier Stokes equations. Here, an extension to high Reynolds number flows by using the Reynolds Averaged Navier Stokes equations has been made.

- It has been shown that in case of laminar boundary layer approximation, some contributions of the complete expression of the aerodynamic force are negligible.

- In case of turbulent boundary layer, the same analysis remarks the importance of a term associated with the turbulent stress tensor. However, it has been shown that this contribution does not need to be computed by a proper choice of the external surface orientation.

- The effect of the integration domain has been investigated at different Reynolds numbers and angles of attack. By decomposing the aerodynamic force in surface and volume contributions, it has been possible to identify the specific contributions to the total aerodynamic force.

- It has also been verified that as the external boundary of the computational domain tends towards infinity, the lift reduces to the volume

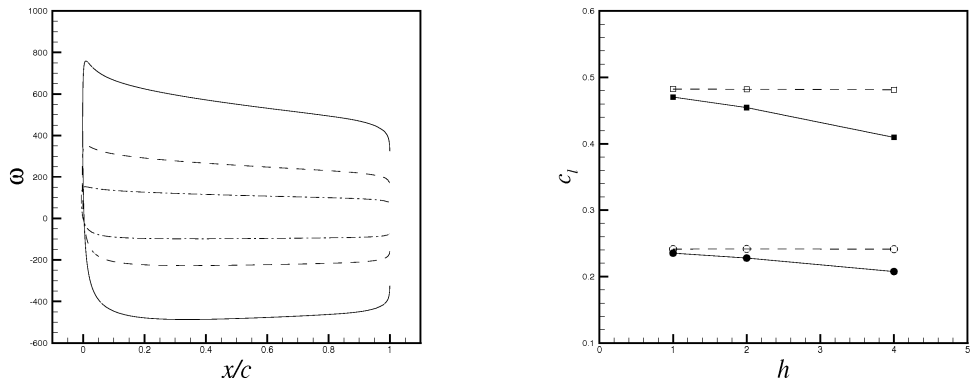

(a) (b)

Figure 4.11: Steady inviscid flow solutions. (a) Wall vorticity from equation (4.57). —, $h = 1$; $--$, $h = 2$; $- \cdot -$, $h = 4$. (b) Lift coefficients: open symbols refer to the *near field* method, full symbols to the *far field* method. circle, $\alpha = 2°$; square, $\alpha = 4°$.

integral of the Lamb vector (vortex force), whereas the drag coefficient results expressed by a surface integral intersecting the airfoil wake. This represents a linkage with the inviscid theories illustrated in the chapter 3.

- From a numerical point of view, the most accurate values of the aerodynamic force have been obtained with an integration domain that intersects the wake just downstream the airfoil trailing edge and that contains the whole boundary layer region. A certain dependency upon the outer boundary conditions has been noted. The accuracy of the drag is sensitive to the solution quality in the flow region where the surface is located.

- Through a proper reconstruction of the Lamb vector, the computation of the aerodynamic force from an inviscid flow field has been possible as well.

Chapter 5

Numerical Simulations of an Oscillating Airfoil

In this chapter, the numerical simulation of a dynamic stall past an oscillating airfoil is presented. The focus is to investigate the capabilities of the RANS methods in the prediction of a dynamic stall in the transitional flow regime. Few applications are found for low Reynolds numbers, even if in some important cases the dynamic stall occurs at Reynolds numbers of order $\sim 10^5$, as the wind turbines. The lack of well assessed comparisons between numerical experimental comparisons at low Reynolds numbers is due to the complexity of experiments. Besides, the well known limits of the turbulence modeling in the RANS methods make this kind of analyses fairly uncertain. In the following, a dynamic stall experiment at $Re = 1.35 \cdot 10^5$ past an oscillating airfoil is taken as a reference for the numerical simulations. A particular concern is the dynamics of the laminar separation bubble (LSB), formed at the leading edge of the airfoil, and its interaction with the dynamic stall vortex (DSV). First, a steady analysis is carried out, and then several pitching conditions are discussed by varying the amplitude and the frequencies of the airfoil motion.

5.1 The experiment of Lee

In 2004, Lee & Gerontakos [80] published a set of experimental data concerning the flow around an oscillating airfoil at Reynolds number of $1.35 \cdot 10^5$. The tests were carried out in the wind tunnel test facility at University of

McGill in Canada. The dimensions of the test section are 0.9m × 1.2m × 2.7m. The model consists of a rectangular wing with a constant NACA0012 section. The chord is 15 cm long and the span is 37.5 cm. Two circular end-plates, having a diameter of 30 cm, are mounted at the tips of the wing in order to reduce the three dimensional effects of the flow. The angle of attack of the model is changed by means of a flywheel oscillation mechanism with the rotation axis at $0.25c$. A small gap, less than 1 mm, is leaved between the wing and the stationary end-plates.

The free stream velocity in the experiment is 35 m/s, with a turbulence level of 0.08%. A natural transition from laminar to turbulent flow occurs on the airfoil surface. Both static and dynamic measurements of the aerodynamic lift and drag are obtained by monitoring 61 pressure taps distributed on the airfoil surface. The description of the phenomenon is supported by smoke flow visualizations as well. The test model is equipped with an array of 140 multi-element hot-film sensors (MHS) to check the flow transition, the separation and the turbulent reattachment of the laminar bubbles. In a previous work, Lee & Basu, [81], exposed the method to extract such information form the MHS signals.

5.2 The numerical setup

The numerical simulation of the experimental conditions indicated by Lee is a challenging test for any RANS code. The Reynolds number of $1.35 \cdot 10^5$ allows for the formation of the LSB on the suction side of the airfoil surface. The natural transition of the flow requires the use of specific prevision methods to be coupled in the RANS method. Besides, under pitching conditions, the transition location and the laminarization abscissas vary with the angle of attack in unsteady way. This problem was addressed by Radespiel et al. [82] in 2006 by assembling a transition method coupled with the time integration of a RANS method. In the present work, the problem has been handled by performing fully turbulent simulations with very low values of the free stream parameters. The effectiveness of this approach has been verified by Catalano

& Tognaccini in 2009 [83] on an airfoil in static conditions at $Re = 6 \cdot 10^4$. They obtained the formation of a LSB without fixing the transition point by using a RANS method.

A C-type computational grid has been designed to operate at moderate angles of attack. The airfoil and the wake edges are discretized with 512 and 128 cells respectively. In the normal wall direction 200 cells are used. The total CFD grid is constituted by 153600 cells. The flow domain extends for $30c$ in all the directions. The size of the first cell near the wall is about $10^{-4}c$ to achieve a y^+ of order one. The turbulence models used in this application are the SST model of Menter [63] and the TNT model of Kok [62].

5.3 Static analysis

5.3.1 Grid size effects

The numerical simulations of the steady flow have been performed by varying the angle of attack α from 0° to 14°. The SST model has been used for the two dimensional simulations at Mach number $M = 0.1$. By coarsening the computational grid of a factor 2 in each direction, mesh refinement studies have been made up to $\alpha = 6°$. For $\alpha > 8°$ the convergence was improved by using the time accurate algorithm, even if the flow solution obtained has always been steady up to $\alpha = 14°$. In figures (5.1), the effects of the grid refinement are showed in terms of lift and drag coefficients. The lift and drag are plotted versus the average grid spacing ratio h. The finest level corresponds to $h = 1$. The quadratic behaviour of the interpolating curves proves the second order accuracy of the solution. In figure (5.2), the pressure coefficient C_P and the skin friction C_f distributions on the airfoil surface are plotted for the three grid levels at $\alpha = 0°$ and $\alpha = 6°$. At $\alpha = 0°$, the grid refinement effects on C_P are not perceptible, while a difference is visible on C_f where the transition occurs. At $\alpha = 6°$, the grid effects are visible on the pressure coefficient at about $x = 0.2c$, and, on skin friction coefficient, near the LSB. However, these effects have a small influence in terms of global

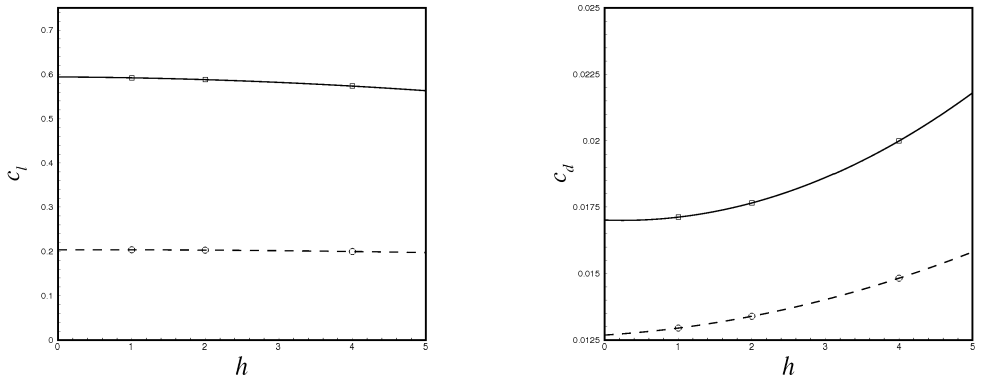

(a) (b)

Figure 5.1: Steady turbulent flow at $Re = 1.35 \cdot 10^5$. Effects of the grid convergence on the lift and drag coefficient. Quadratic extrapolation to infinite mesh values. (a) C_l: $-\circ-$, $\alpha = 2°$; -□- , $\alpha = 6°$; (b) C_d: $-\circ-$, $\alpha = 0°$; -□- , $\alpha = 6°$;

aerodynamic coefficients.

5.3.2 Two dimensional analysis

In figure (5.3a), the numerical $C_l - \alpha$ curve is compared with a set of experimental data. Lee [80] and McCroskey [78] refer both at Reynolds $1.35 \cdot 10^5$, while the data of Hansman [84] are at Reynolds $3.1 \cdot 10^5$ and those from Alreafi [85] at Reynolds $1.1 \cdot 10^5$. In the linear part of the lift curve $\alpha \leq 6°$, the agreement of the numerical data is satisfactory with all the experimental curves except for Lee. The slope of the lift curve $C_{l\alpha}$, obtained numerically, is 0.0987. In [80], the authors confirms that the measured $C_{l\alpha}$ is 0.08. This value disagrees with the hypothesis of a two dimensional flow, and it is fairly near to a $C_{l\alpha}$ of a finite wing. The numerical data show a change in the $C_{l\alpha}$ for $\alpha > 8°$. In the computations, the static stall occurs between $\alpha = 10°$ and $\alpha = 12°$ and it is fairly anticipated with respect to the experimental one, $\alpha_s \approx 13°$. The lift recovery in the post stall condition is similar in the shape to the experiments but without a correspondence with the angles. In figures (5.3b), the drag coefficients are reported against the angle of attack.

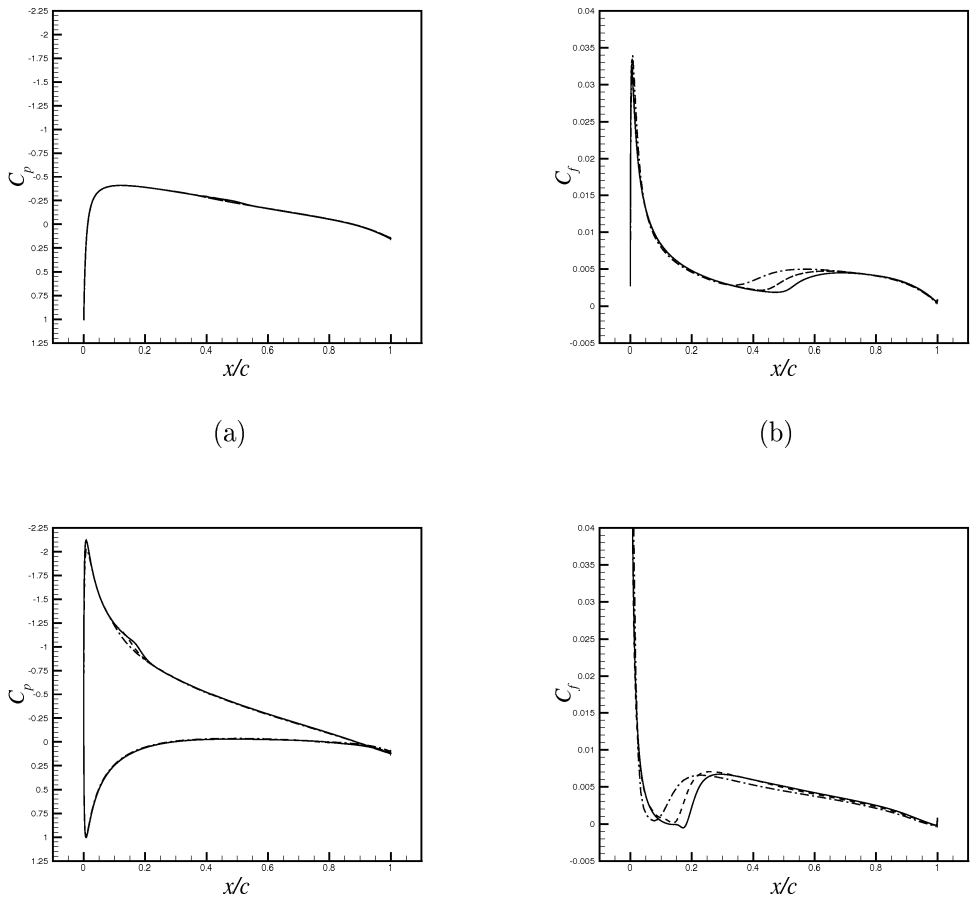

Figure 5.2: Steady turbulent flow at $Re = 1.35 \cdot 10^5$. Grid convergence effects on C_P and C_f distributions. (a), C_P at $\alpha = 0°$; (b), C_f at $\alpha = 0°$ (suction side); (c), C_P at $\alpha = 6°$; (d), C_f at $\alpha = 6°$ (suction side). $- \cdot -$, $h = 4$; $- - -$, $h = 2$; $-$, $h = 1$.

The present RANS computations are compared with some experimental data of McCroskey [78] and with a numerical solution using the Detached Eddy Simulation (DES) model by Shur et al. [86] at Reynolds number 10^5. The maximum drag coefficient at $\alpha = 13°$ of Lee's experiment is also indicated. At $\alpha = 0°$, the experimental C_d provided by McCroskey is slightly higher than RANS. At $\alpha = 8°$ and $\alpha = 10°$ the RANS data match well the DES results. The maximum drag coefficient is reached at $\alpha = 12°$ by RANS and

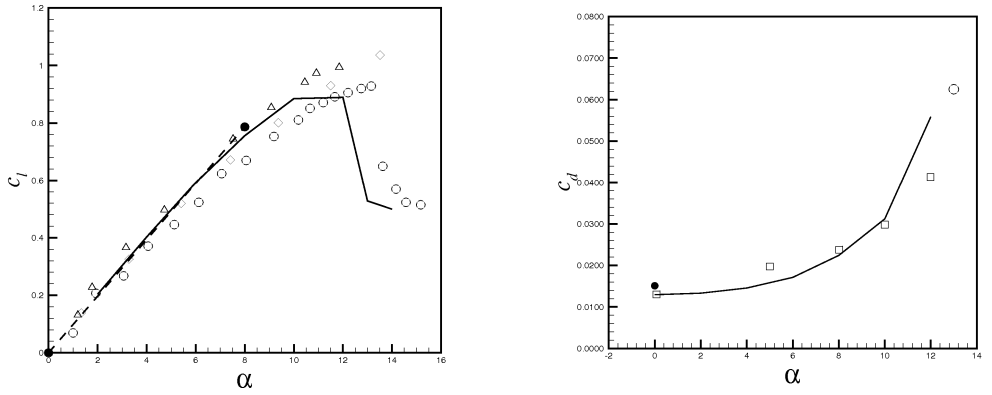

(a) (b)

Figure 5.3: Steady turbulent flow at $Re = 1.35 \cdot 10^5$. Lift and drag curves. − , RANS model; -•- McCroskey [78]; ∘, Lee [80]; ◇, Hansman [84] ($Re = 3.1 \cdot 10^5$); △, Alreafi [85] ($Re = 1.1 \cdot 10^5$); □ , DES [86] ($Re = 10^5$). (a), C_l; (b), C_d.

is lower than one indicated by Lee. However, an overall agreement between the lift and drag curves is obtained. Some isolated discrepancies are justified due the different treatment of the transition in the various numerical and experimental data.

In figure (5.4a), the position of the laminar separation at the leading edge is reported for each angle of attack and compared with the corresponding experimental locations from Lee [80]. In the numerical solutions, the separation appears for $\alpha \geq 6°$ while in the experiments is observed already at $\alpha \geq 2°$. The trend in terms of x and α ratio is similar. In figure (5.4b), the transition location indicated by the experiments is analyzed at different α. The area in which the numerical eddy viscosity ratio, μ_t/μ, grows from 1 to 10 has been delimited by two curves. In such a region, the experimental data confirms the presence of the transition from laminar to turbulent flow. The turbulent separation location at the trailing edge is reported as function of α in figure (5.4c). In the numerical results, the RANS solutions provide a turbulent flow separation at the trailing edge zone for $\alpha \geq 6°$. In the experiments, large zones of separated flow occur for lower angles of attack.

From these comparisons, several inconsistencies appear between the ex-

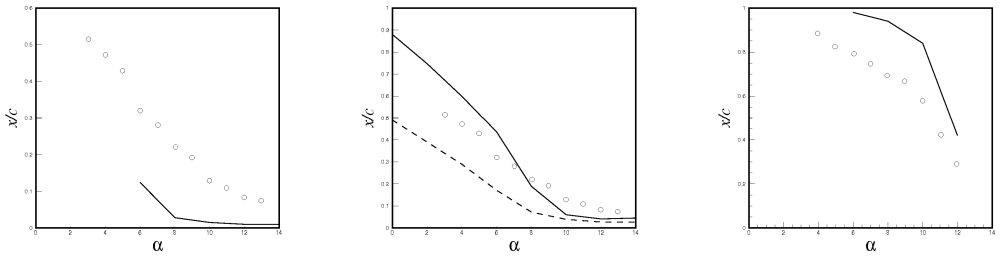

(a) (b) (c)

Figure 5.4: Steady turbulent flow at $Re = 1.35 \cdot 10^5$. Critical flow points on the suction side of the airfoil. (a) Laminar separation at the leading edge; (b) Transition location; (c) Trailing edge separation. ∘, experimental values from Lee [80]; —, present RANS computation. In (b), − − − $\mu_t/\mu = 1$ and — $\mu_t/\mu = 10$.

periment of Lee and the present RANS solutions. For the latter, the agreement improves with other low Reynolds data set. From the numerical point of view, a critical issue is the treatment of the transition from laminar to turbulent regime as well as the effectiveness of the turbulence models at low Reynolds numbers. About the experimental test, some doubts about the two dimensionality of the flow arise.

5.3.3 The three dimensional analysis

In a paper published in 2005 [87], Birch & Lee reported a scheme of the experimental setup used in the laboratory. The top view is depicted in figure (5.5). As may be seen, the wing is limited by two circular end-plates and a small gap between the test model and the end-plate exists. Besides, the end-plates are not in touch with the wind tunnel walls, but are located at a certain distance. It is reasonable to expect that such configuration exhibits three dimensional effects in the middle sections. To investigate these aspects, the simulation of the effective experimental apparatus has been conducted. In particular, two geometrical parameters have been analyzed: the first is the distance H between the end-plates and the lateral wind tunnel walls, the second is the gap between the end-plate and the test model. A discussion

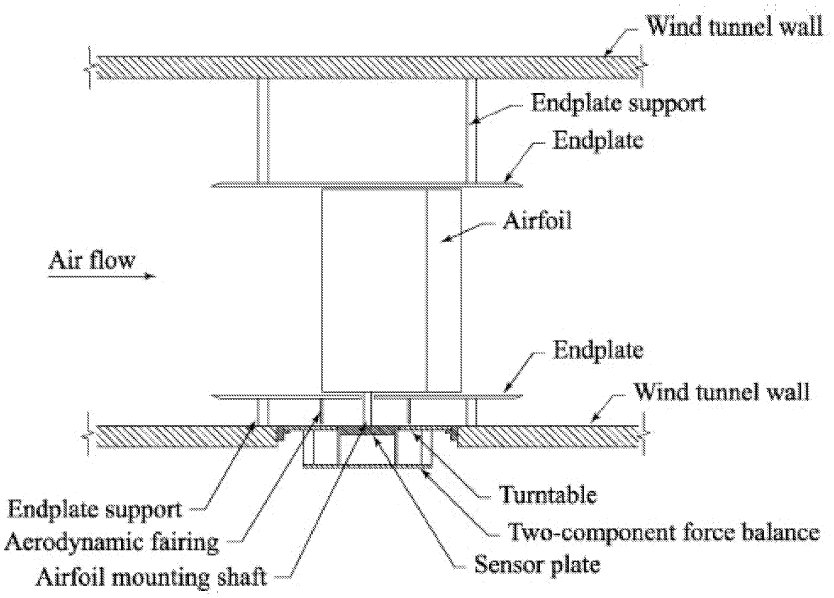

Figure 5.5: Top view of the experimental setup described by Lee in [87].

on the effects of the gap size of the semi-span models can be found in the work of Marchman in 1987 [88]. A conclusion was that the gap can cause higher drag values and a shift of the zero lift angle of attack, especially at low Reynolds number. The size of the gap, instead, seems to have a secondary influence.

A geometrical model has been defined and indicated in figure (5.6). The hypothesis of the flow symmetry in the middle section has been adopted. The semi-span model is $1.25c$ wide. The end-plates have been simulated as a circular flat plate of zero thickness. A gap of $0.0067c$ has been foreseen. Besides, the wind tunnel lateral wall has been simulated at different distances H from the end-plates.

The three dimensional computational mesh has $8.5 \cdot 10^6$ cells on the finest level. The topology and the superficial grids are visible in figure (5.7). The end-plates are simulated with a no-slip wall condition and the lateral wind tunnel wall with a slip-solid wall one. The flow condition at $\alpha = 6°$ has been considered. The TNT turbulence model has been used for these analyses.

First, the effect of the parameter H is examined without considering

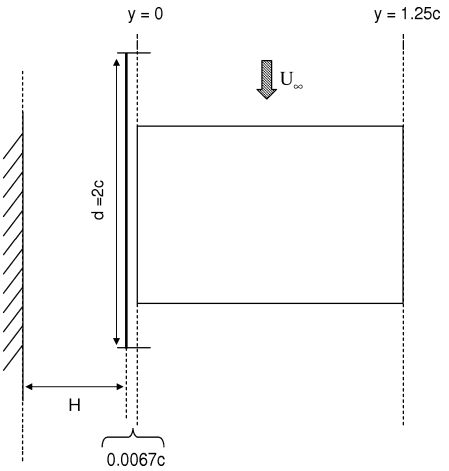

Figure 5.6: Three dimensional CFD model.

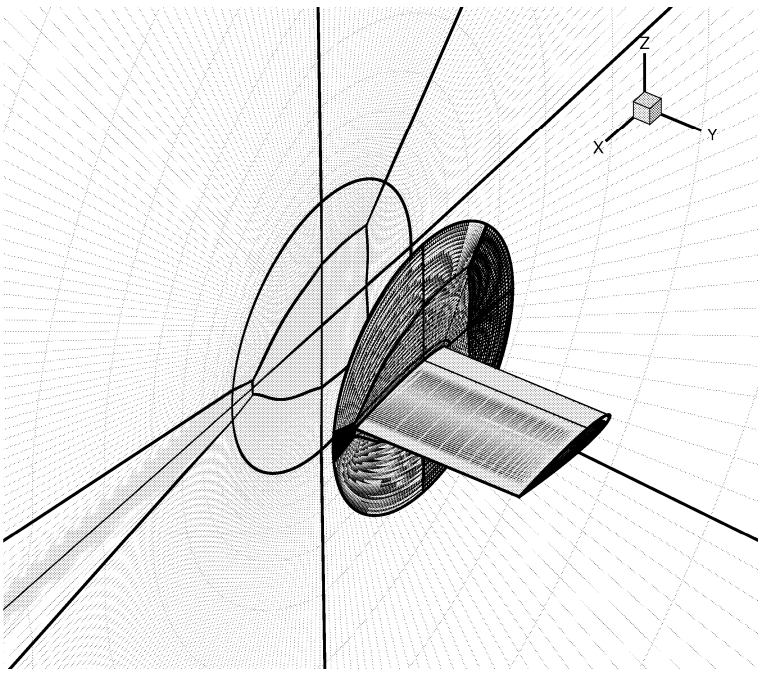

Figure 5.7: Computational mesh of the three dimensional geometry.

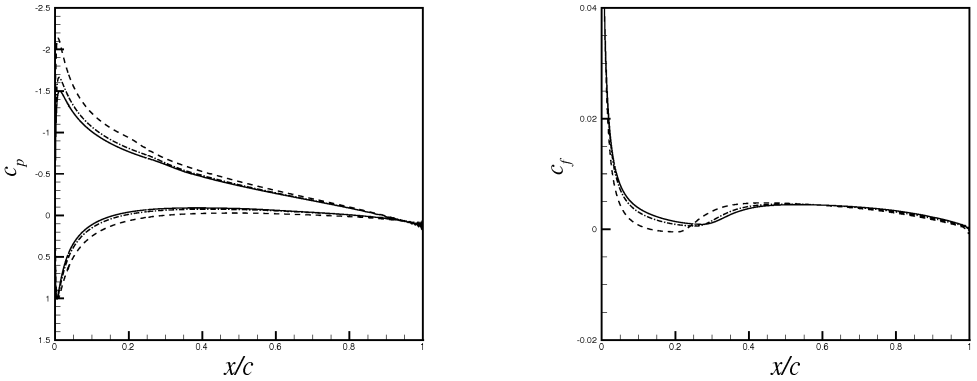

(a) (b)

Figure 5.8: Steady turbulent flow at $Re = 1.35 \cdot 10^5$ at $\alpha = 6°$. Three dimensional simulations. Effects of the lateral wall of the wind tunnel test section. $- - -$, $H = 0$; $- \cdot -$, $H = 0.75c$; —, $H = 15c$. (a), C_P; (b), C_d.

the gap. In this case the end-plates are joined with the test model. The simulations are compared with the two dimensional numerical simulation in the symmetry plane at $y = 1.25c$. The results are shown in figures (5.8a) and (5.8b) in terms of C_P and C_f. The case $H = 0$, which corresponds to the end-plate in touch with the wind tunnel walls, does not provide any three dimensional effect. The C_P and C_f curves overlap to the 2D simulation plots at the same α. The boundary layer developed between the end-plate and the test model does not affect significantly the total lift and drag and, consequently, the flow in the section $y = 1.25c$. A second test at $H = 0.75c$, which is the distance observed in the scheme (5.5), shows a reduction of the expansion peak on the pressure distribution at $y = 1.25$, and, as a consequence, the disappearance of the LSB. By increasing the distance H up to $15c$, this trend is confirmed by a further reduction of the expansions on the upper surface of the test model. The LSB disappears as H increases, and the turbulent transition is delayed.

The effects of the gap, instead, are analyzed by fixing the lateral wall distance at $H = 15c$. The results in terms of C_P and C_f are reported in figures (5.9a) and (5.9b). As may be seen, the gap has the effect to reduce

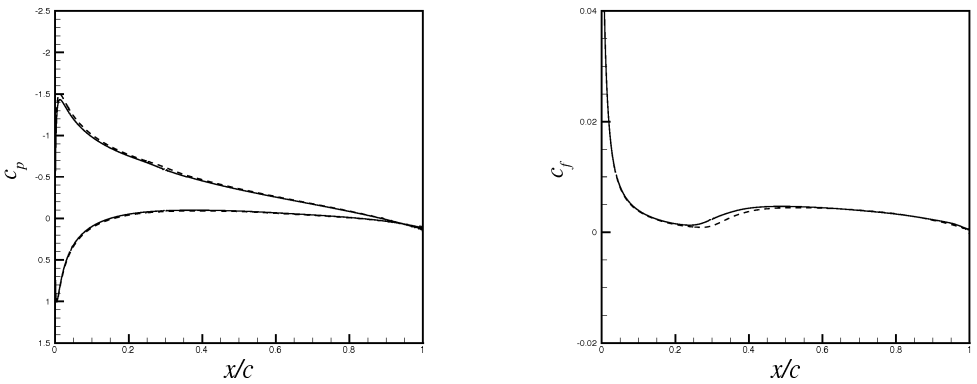

(a) (b)

Figure 5.9: Steady turbulent flow at $Re = 1.35 \cdot 10^5$ at $\alpha = 6°$. Three dimensional simulations. Effects of the gap between the end-plates and the test model. $- - -$, gap filled; —, gap not filled. (a), C_P; (b), C_d.

the pressure coefficient peak, but to anticipate the transition. However such effects have a secondary importance on the integrated coefficients.

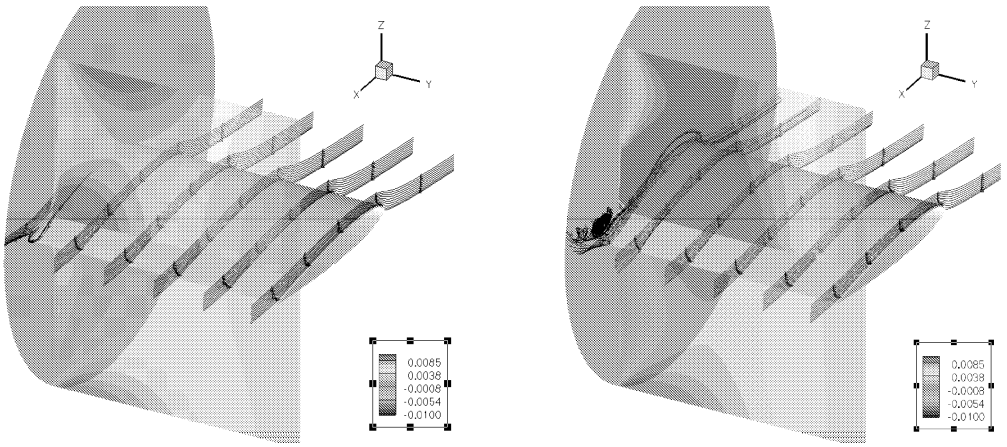

(a) (b)

Figure 5.10: Steady turbulent flow at $Re = 1.35 \cdot 10^5$ at $\alpha = 6°$. Stream lines near the intersection of the end-plate and the test model. Contour slide of the y component of the velocity vector. (a), without gap; (b), with the gap.

In figures (5.10a) and (5.10b), a three dimensional visualization of the flow field is reported. The presence of the gap increases the separation near the intersection between the end-plate and the test model, as can be noted by the strem lines. A slide reporting the contour levels of the y component of the velocity highlights the blockage effect caused by the flow passage between the end-plate and the wind tunnel lateral walls. The configuration $H = 0.75c$ without gap has been used to compute the static lift curve from $\alpha = 3°$ to $\alpha = 14°$. As may be seen in figure (5.11), the experimental C_{l_α} is correctly reproduced by the three dimensional computations. The lift values are slightly underestimated. But, further geometrical tuning can improve the results. The abrupt stall, not captured by the 2D simulations, has been reproduced as well. The static stall angle, $\alpha = 13°$, agrees with the experimental information as well as the maximum lift coefficient. The hypothesis of three dimensional effects in the wind tunnel measurements has been confirmed. It has also been verified that the boundary layer developed along the intersection between the end-plate and the test model has a negligible effect on the pressure and skin friction distributions in the middle section. Other aspects, such as the transition, have to be investigated with more proper

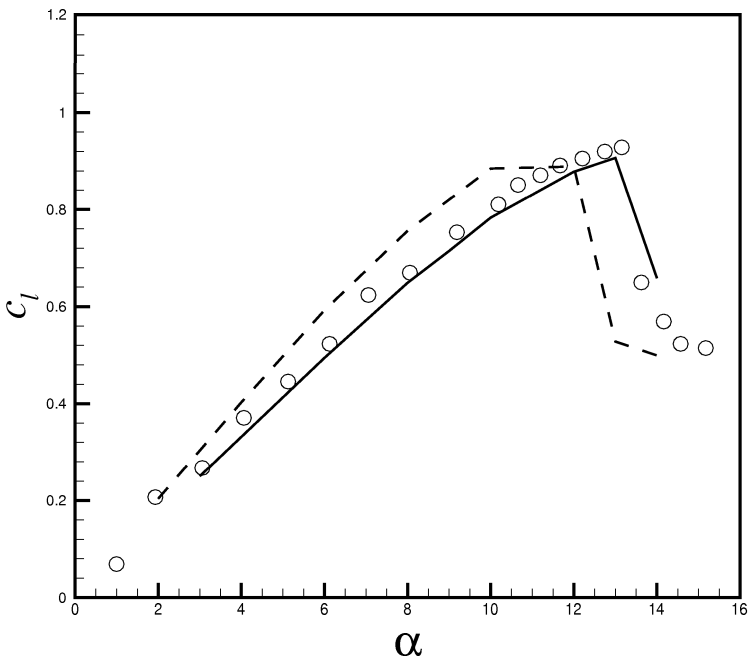

Figure 5.11: Steady turbulent flow at $Re = 1.35 \cdot 10^5$ at $\alpha = 6°$. Static lift curve. − − − , 2D computations; — , 3D computations; ∘, experiments.

techniques.

5.4 Dynamic analysis

The excessive computation effort required by the three dimensional configuration does not permit to continue the numerical simulations for the oscillatory conditions. For these reasons, the unsteady analysis is carried out by using the two dimensional geometry.

5.4.1 Pre stall simulations

In the *pre stall* regime, the airfoil oscillates within a range of α without reaching the static stall angle. Such simulation is performed by imposing the

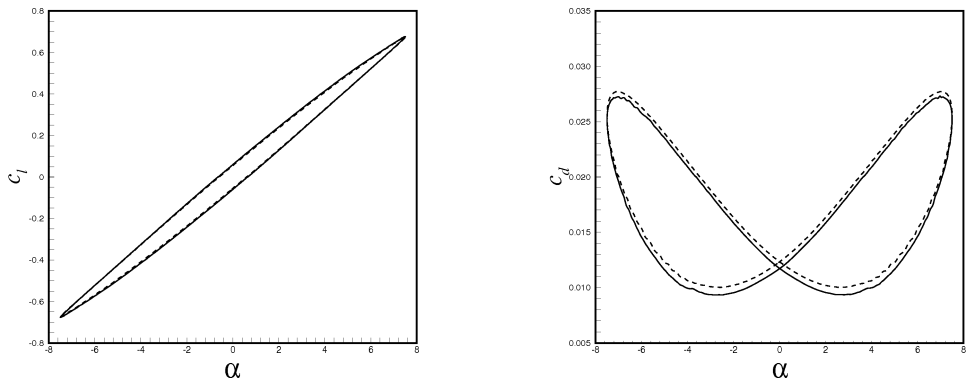

(a) (b)

Figure 5.12: Unsteady turbulent flow. $Re = 1.35 \cdot 10^5$, $\alpha = 7.5° \sin(2kt)$, $k = 0.05$. $- - -$, $h = 2$; $-$, $h = 1$. (a), C_l ; (b), C_d .

following pitching motion:

$$\alpha = 7.5° \ \sin(2kt)$$

with a reduced frequency $k = 0.05$ is considered. The non dimensional period T is related to the reduced frequency as $T = \pi/k$. A sensitivity study on the time step effects has been done by refining of a factor 2, from $T/128$ to $T/1024$. A full convergence in time has been achieved by sampling T with 1024 steps. The effects of the grid refinements are visible in figures (5.12a) and (5.12b). For this range of oscillations, the grid independency has been achieved in terms of C_l. A small sensitivity on the C_d is observed by figure (5.12b). The hysteresis loops of the lift and drag are exactly symmetrical because of the symmetry of the angular motion and the airfoil geometry. In figure (5.13a), the hysteresis cycle of the lift coefficient is compared with the analytical solution provided by Theodorsen and the static lift curve. The analytical solution agrees with the numerical one within the range $|\alpha| \leq 3°$. The fluid viscosity produces a reduction of the maximum lift coefficient obtained at the extremities of the cycle with respect to the theoretical curve. The static lift coefficients have also been reported for a reference. The comparison with the experimental data of Lee is shown in figure (5.13b). The

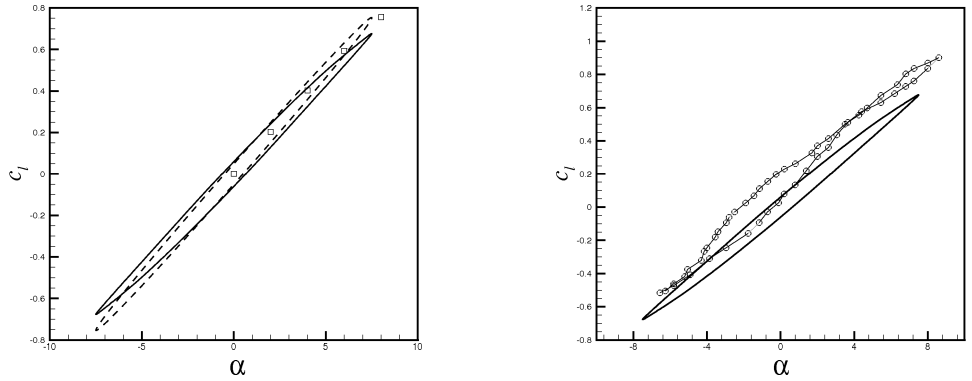

(a) (b)

Figure 5.13: Unsteady turbulent flow. $Re = 1.35 \cdot 10^5$, $\alpha = 7.5° \sin(2kt)$, $k = 0.05$. Hysteresis loops of C_l. $-$, unsteady RANS; $- - -$, Theodorsen solution; □ , steady RANS; $- \circ -$, experimental data.

agreement is qualitative and a shift in terms of the mean angle of attack and the angular amplitude is visible. The discrepancies are partially associated with the three dimensional effects discussed before. A lack of the symmetry in the hysteresis cycle is visible in the experimental curve. This suggests the presence of an asymmetry in the pitching motion. Two angular corrections of kind

$$\alpha = \Delta\alpha_m + (7.5° + \Delta\alpha_0)\ \sin(2kt)$$

have been proposed: the first with ($\Delta\alpha_m = 1°$, $\Delta\alpha_0 = 0.1°$), and the second with ($\Delta\alpha_m = 2.5°$, $\Delta\alpha_0 = 2.5°$). The resulting hysteresis loops are reported in figures (5.14). The first test matches only the actual angular variation. The second test gives an agreement in the $C_{l max}$ and $C_{l min}$. The asymmetry is numerically reproduced as well, although the agreement is only qualitative.

The effects of the unsteadiness in terms of C_P and C_f are visible in figures (5.15). The pressure and skin friction distributions on the airfoils obtained at $\alpha = 7.5°$, are compared with the steady solution at the same angle of attack. The flow unsteadiness produces a smaller expansion peak on the pressure and delays the laminar separation. Lee finds an important reduction in size of the laminar separation bubble when the airfoil is pitching

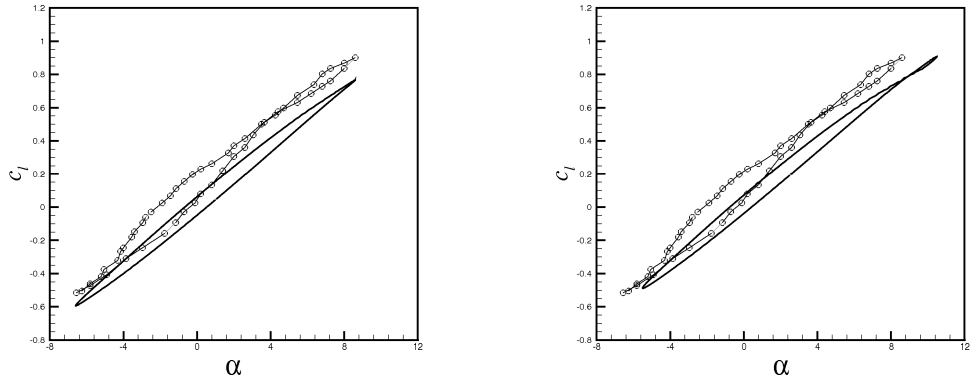

(a) (b)

Figure 5.14: Unsteady turbulent flow. $Re = 1.35 \cdot 10^5$, $\alpha = 7.5° \sin(2kt)$, $k = 0.05$. Hysteresis loops of C_l. (a) $\Delta\alpha_m = 1°$, $\Delta\alpha_0 = 0.1°$; (b) $\Delta\alpha_m = 2.5°$, $\Delta\alpha_0 = 2.5°$. $-\circ-$, exp; —, unsteady RANS.

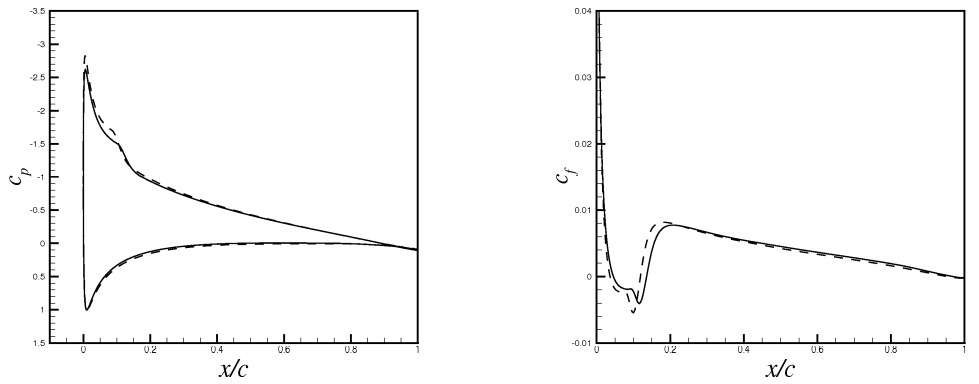

(a) (b)

Figure 5.15: Unsteady turbulent flow. $Re = 1.35 \cdot 10^5$, $\alpha = 7.5° \sin(2kt)$, $k = 0.05$. $---$, steady RANS at $\alpha = 7.5°$. —, unsteady RANS at $\alpha = 7.5°$. (a) C_P; (b) C_f.

up (from $0.11c$ of the static case to $0.044c$ of the unsteady case at $\alpha = 7.5°$). In the present numerical simulations, the bubble extension does not change significantly. In figure (5.16), the location of the unsteady transition from laminar to turbulent zone, extracted on the upper side of the airfoil at each time instant, is reported as function of α. The transition point has been

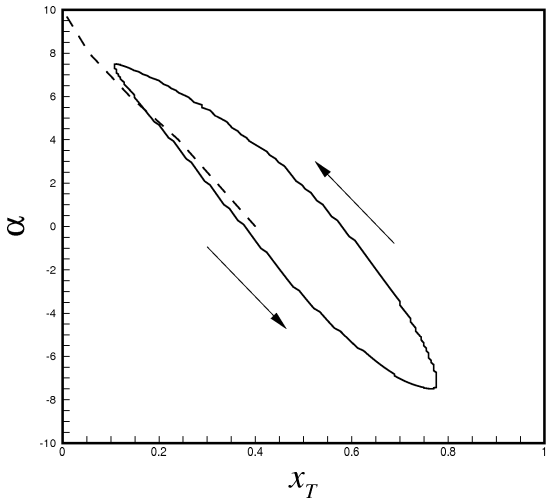

Figure 5.16: Unsteady turbulent flow. $Re = 1.35 \cdot 10^5$, $\alpha = 7.5° \sin(2kt)$, $k = 0.05$. Transition abscissa on the upper side of the airfoil. $- - -$, steady computation; —, unsteady computation at $\alpha = 7.5°$.

detected through the inspection of the μ_t/μ field in the boundary layer. The versus of the hysteresis loop confirms the experimental observation that the transition is delayed with respect to the steady case during the pitching-up phase.

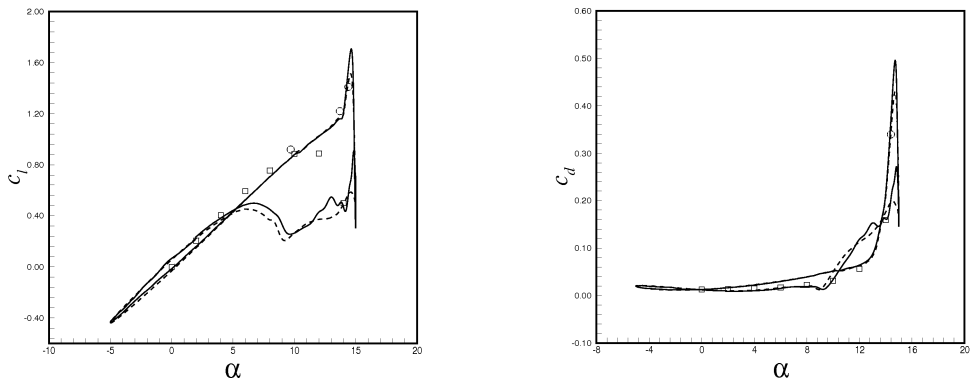

(a) (b)

Figure 5.17: Unsteady turbulent flow. $Re = 1.35 \cdot 10^5$, $\alpha = 5° + 10° \sin(2kt)$, $k = 0.05$. Aerodynamic coefficient loops. □ static data. $- - -$, $h = 2$; — , $h = 1$; (a), C_l ; (b), C_d .

5.4.2 Light stall simulation

A *light stall* simulation has been carried out by imposing the following pitching motion:

$$\alpha = 5° + 10° \sin(2kt)$$

with a reduced frequency $k = 0.05$. The angular motion is such that the dynamic stall occurs within a fraction of the oscillating cycle. The period T has been sampled with 1024 time steps. Fully periodic conditions have been achieved after a simulated time equal to $4T$. The grid refinement study, (see figures 5.17) shows a mesh size dependency on the $C_{l\,max}$, and during the pitching down phase. This effect is associated with the convection of large vortices far away from the solid surface where the grid resolution is not sufficiently high. The maximum lift and drag coefficients indicated in the experiment are lower with respect to the numerical ones. The static curve is also reported for a reference. In the following the discussion is referred to some specific points of the hysteresis cycle. In figure (5.18) the identification of these points is reported on the lift, drag and moment curves. Besides, the corresponding distributions of C_P and C_f are reported in figures (5.19) and

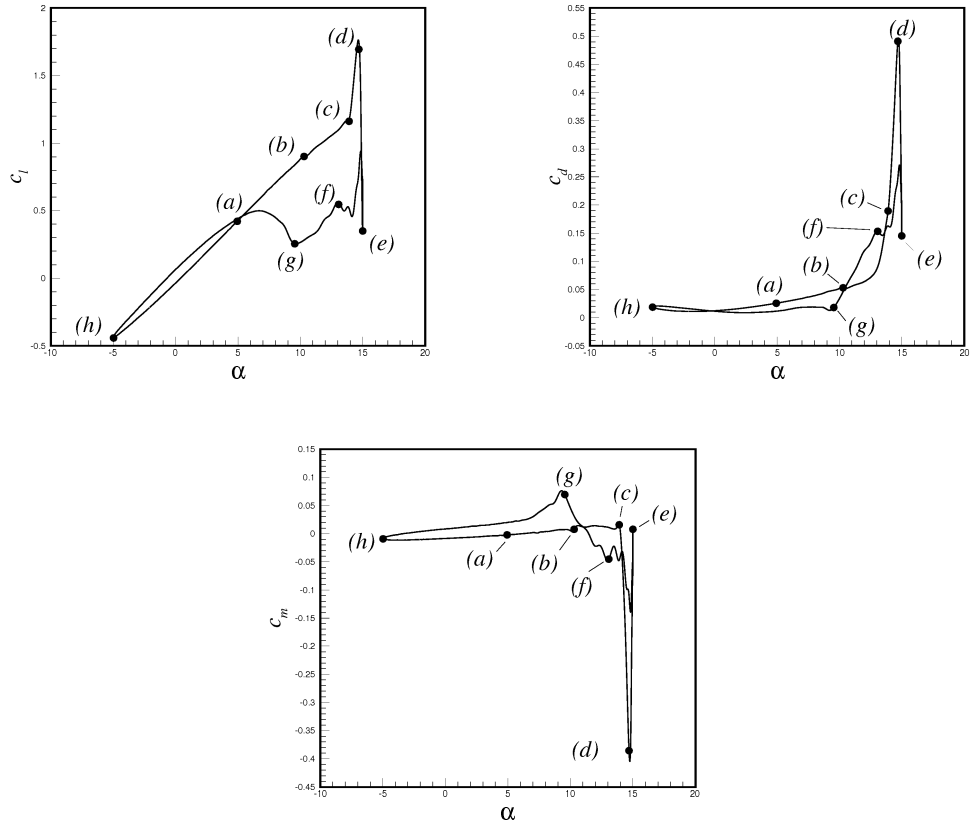

Figure 5.18: Unsteady turbulent flow. $Re = 1.35 \cdot 10^5$, $\alpha = 5° + 10° \sin(2kt)$, $k = 0.05$. Identification of some specific points on the aerodynamic coefficient loops.

(5.20).

- Phase (a)-(b). $\alpha = 5° \div 10.3°$. The lift curve is within the linear behaviour. A sort of extrapolation of the linear slope is achieved even if the static stall angle is exceeded. The LSB appears at $\alpha = 7.3°$ and, in the point (b), is clearly visible by the C_f diagram (see figure 5.20b). The bubble moves toward the leading edge reducing its extension as the flow incidence increases.

- Phase (b)-(c). $\alpha = 10.3° \div 13.9°$. The lift continues to increases linearly. The drag increases showing a rapid change in the slope. The moment curve is still flat. Several phenomena occur simultaneously in

the boundary layer. The LSB reaches the minimum extension and the negative pressure peak grows at the leading edge. A separation begins at the trailing edge while the LSB disappears leaving the place to the formation of the dynamic stall vortex (DSV). In (c) the DSV is visible by the C_P diagram.

- Phase (c)-(d). $\alpha = 13.9° \div 14.5°$. The C_{l_α} increases and the lift reaches the maximum value in the point (d). The drag takes its maximum value as well. The moment coefficient stalls during the lift growth because of an unbalanced distribution of pressure. In the point (c), the flow is separated up to $0.5c$. The separation propagates forward toward the trailing edge. As the DSV is convected forward, secondary vortices produce a local reattachment around $x = 0.4c$. In the outer layers, the DSV increases in intensity following the external stream direction. A visible distortion of the pressure coefficient distribution gives evidence of the DSV passage on the airfoil.

- Phase (d)-(e). $\alpha = 14.5° \div 15°$. After the maximum value reached in the point (d), the lift collapses suddenly. Simultaneously, the moment coefficient recovers. The DSV is convected downstream in the turbulent wake. The secondary vortices detach from the airfoil trailing edge. In the point (e), the pressure coefficient distribution is quite flat and the skin friction coefficient reveals partial separations of the flow.

- Phase (e)-(f). $\alpha = 15° \div 13°$. In the point (e), at $\alpha = 15°$, the lift reaches a minimum. The drag and the moment curves shows some peaks associated with the secondary vortices. At $\alpha = 15°$, the airfoil is similar to a bluff body of size $c \sin \alpha$. The airfoil is completely stalled and behaves as in a post stall static condition. The C_P and C_f diagrams confirm the massive separation on the airfoil upper side. The angle of attack begins to decrease but the airfoil angular position remains completely dissociated from the time flow evolution.

- Phase (f)-(g). $\alpha = 13° \div 9.3°$. The process of the flow reattachment

begins from the leading edge. The lift and drag decrease while the moment coefficient recovers. Even if the angle of attack decreases, the pressure coefficient expands contributing to the reattachment process. A small LSB appears in the point (g).

- Phase (g)-(h). $\alpha = 9.3° \div -5°$. The aerodynamic coefficients slowly recover the linear form. The reattachment of the boundary layer continues from the leading edge achieving gradually fully attached flow conditions.

The present analysis highlights the fundamental linkage between the LSB and the DSV. As α increases, the former reduces its dimensions. The latter originates once the LSB disappears. In the rear part of the DSV, the secondary vortices produce partial flow reattachments. But, once the DSV leaves the airfoil surface, a fully stalled condition is achieved. The moment stall arises before of the lift one. At the maximum flow incidence, the airfoil behaves as a bluff body of size $c \sin \alpha$. The onset of the reattachment process occurs from the leading edge zone. As the linear behaviour is recovered, the pressure gradient allows the new formation of the LSB.

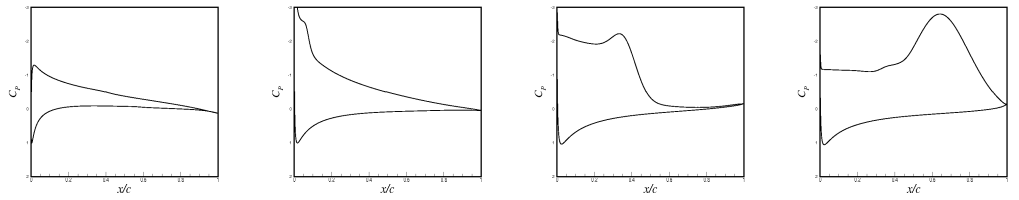

(a) $\alpha = 5°$ (b) $\alpha = 10.3°$ (c) $\alpha = 13.9°$ (d) $\alpha = 14.5°$

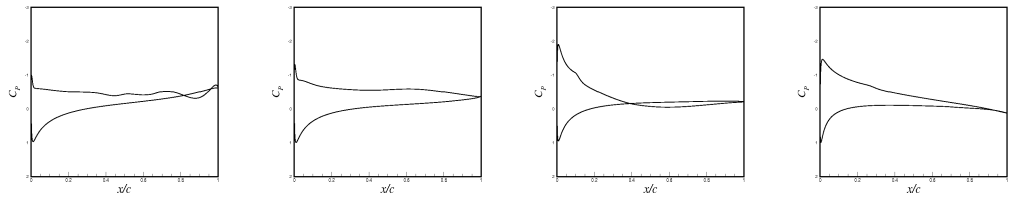

(e) $\alpha = 15°$ (f) $\alpha = 13°$ (g) $\alpha = 9.3°$ (h) $\alpha = -5°$

Figure 5.19: Unsteady turbulent flow. $Re = 1.35 \cdot 10^5$, $\alpha = 5° + 10° \sin(2kt)$, $k = 0.05$. C_P in different phases.

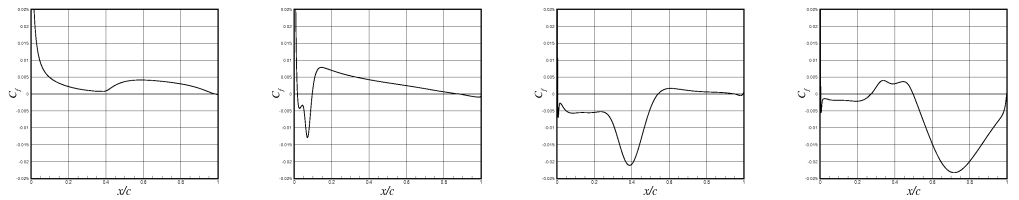

(a) $\alpha = 5°$ (b) $\alpha = 10.3°$ (c) $\alpha = 13.9°$ (d) $\alpha = 14.5°$

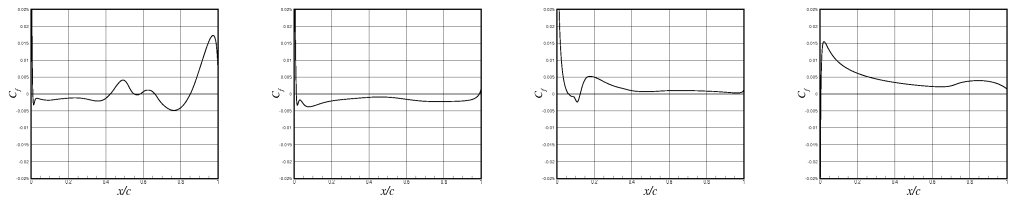

(e) $\alpha = 15°$ (f) $\alpha = 13°$ (g) $\alpha = 9.3°$ (h) $\alpha = -5°$

Figure 5.20: Unsteady turbulent flow. $Re = 1.35 \cdot 10^5$, $\alpha = 5° + 10° \sin(2kt)$, $k = 0.05$. C_f in different phases.

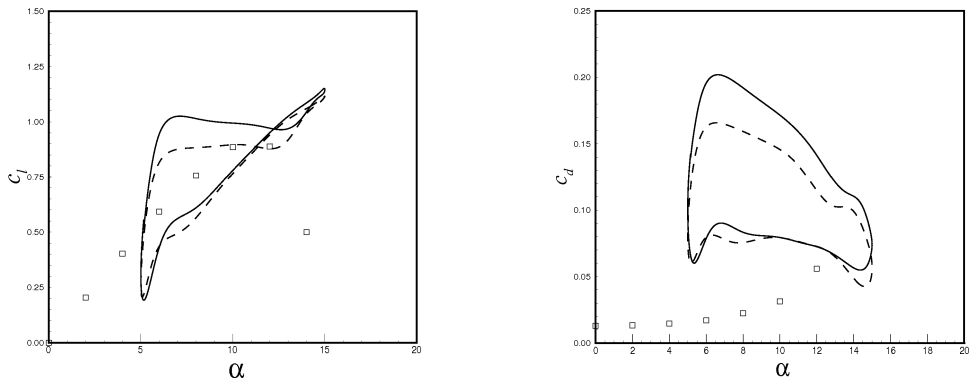

(a) (b)

Figure 5.21: Unsteady turbulent flow. $Re = 1.3 \cdot 10^5$, $\alpha = 10° + 5° \sin(2kt)$, $k = 0.5$. Aerodynamic coefficient loops. —, $h = 2$, medium grid level; $- - -$, $h = 1$, finest grid level; □ steady RANS. (a), C_l ; (b), C_d .

5.4.3 Deep stall simulation

The *deep stall* simulation has been carried out by imposing the following pitching motion:

$$\alpha = 10° + 5° \ \sin(2kt)$$

with a reduced frequency $k = 0.5$, $Re = 1.3 \cdot 10^5$ and $M = 0.3$. Such conditions are similar to a Large Eddy Simulation (LES) carried out by Nagarajan et al. in 2006 [41] and do not have a correspondence with the experiment of Lee. However, the comparison with the high accurate LES solution represents a significant benchmark for the present RANS method. The present *deep stall* case differs from the previous *light stall* in the mean angle of attack and the higher reduced frequency. The angular motion is such that stalled flow conditions occur during the whole cycle leaving the reattachment process incomplete. The time step used is $T/1024$. The comparison of the lift and drag curves obtained on the medium ($h = 2$) and fine($h = 1$) grid levels, (see figure 5.21), shows a major sensitivity on the mesh size with respect to the previous cases. In figure (5.22), the time history of C_l and C_d are compared with the corresponding solutions obtained by LES. The agreement is satisfac-

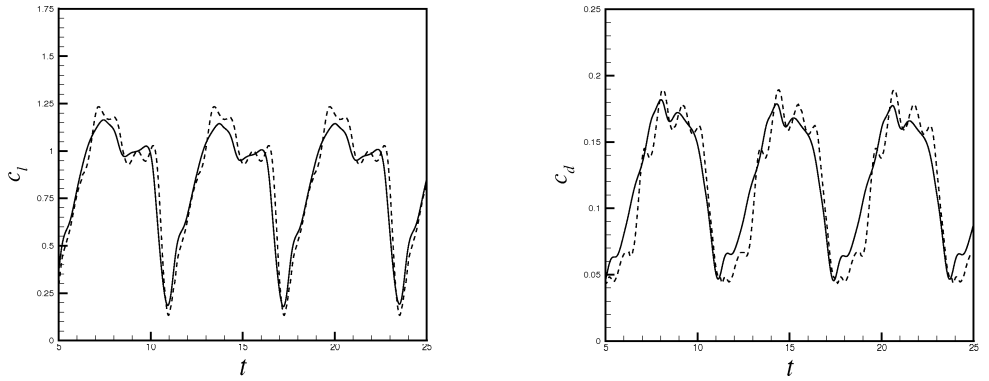

(a) (b)

Figure 5.22: Unsteady turbulent flow. $Re = 1.3 \cdot 10^5$, $\alpha = 10° + 5° \sin(2kt)$, $k = 0.5$. Aerodynamic coefficient time histories. — , unsteady RANS; $- - -$, LES data, [41]. (a), C_l ; (b), C_d .

tory showing that the main flow structures, resolved by LES, are captured by the present RANS solution. In the C_l time history, the double lift peak gives evidence of the dynamic stall vortex passage. The RANS solution slightly underestimates the maximum values of lift and drag. The LES computation shows higher frequencies that in the RANS curve are fairly smooth, but the global agreement is satisfactory. Besides, some distributions of the pressure coefficients of both RANS and LES solutions are reported in figures (5.23a), (5.23b), (5.23c) and (5.23d). The instantaneous α correspond to the passage of the dynamic stall vortex over the upper side of the airfoil. The agreement of the two numerical methods confirms the reliability of the RANS method in predicting such complex flow. Some points of the hysteresis loop are discussed. The identification of the points on the aerodynamic loops is reported in figures (5.24). In figures (5.25) and (5.26) the corresponding distributions of C_P and C_f are indicated.

- Phase (a)-(b). $\alpha = 9.3° \div 12.5°$. The lift increases with a linear slope. The drag and the moment raise simultaneously. A LSB is visible from the C_P and C_f moving toward the leading edge. The LSB restriction is similar to that observed in the *light stall* case. However, a small

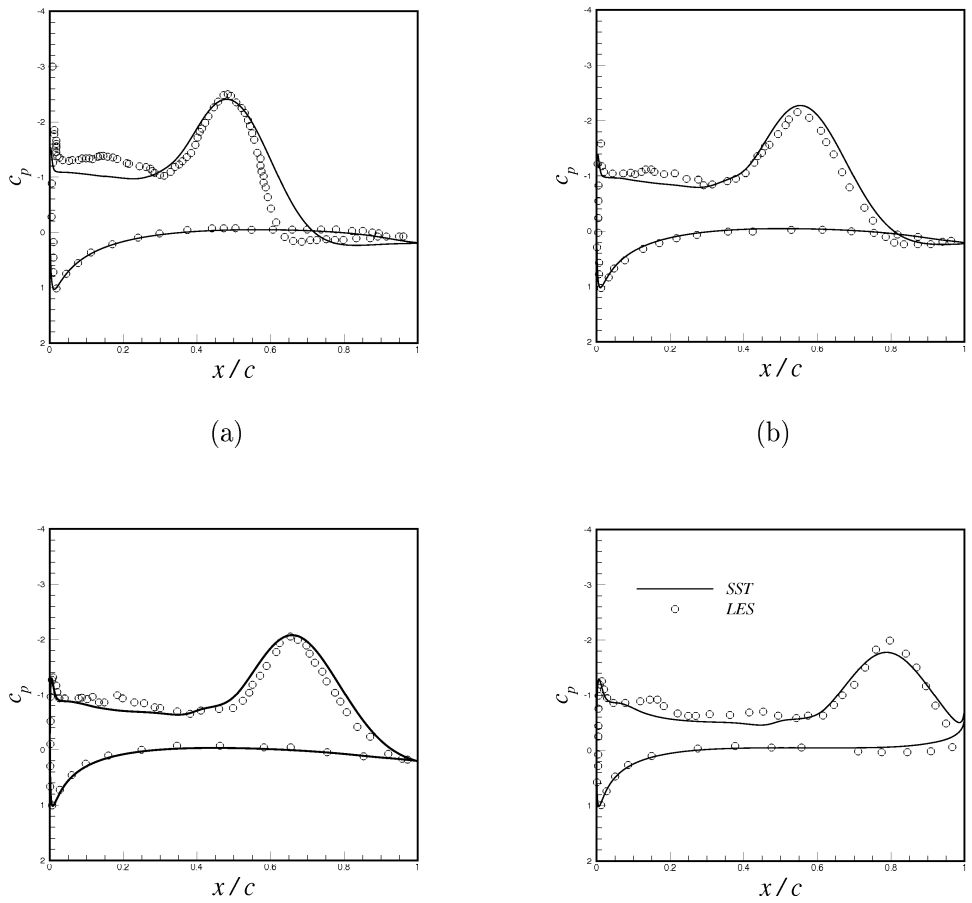

Figure 5.23: Unsteady turbulent flow. $Re = 1.3 \cdot 10^5$, $\alpha = 10° + 5° \sin(2kt)$, $k = 0.5$. Pressure coefficient distributions on the airfoil surface. — unsteady RANS ; ∘, LES data, [41]. (a), $\alpha = 10.3°$; (b), $\alpha = 8.8°$; (c), $\alpha = 7.1°$; (d), $\alpha = 5.6°$.

separation in the middle zone of the airfoil surface is visible in the point (a).

- Phase (b)-(c). $\alpha = 12.5° \div 15°$. The lift continues to increase following the linear slope. The maximum lift coefficient is attained in the point (c), while a change in the drag slope is achieved. A small variation in the slope is visible in the moment curve. The LSB reaches the minimum extension causing the formation of the DSV. The secondary separation

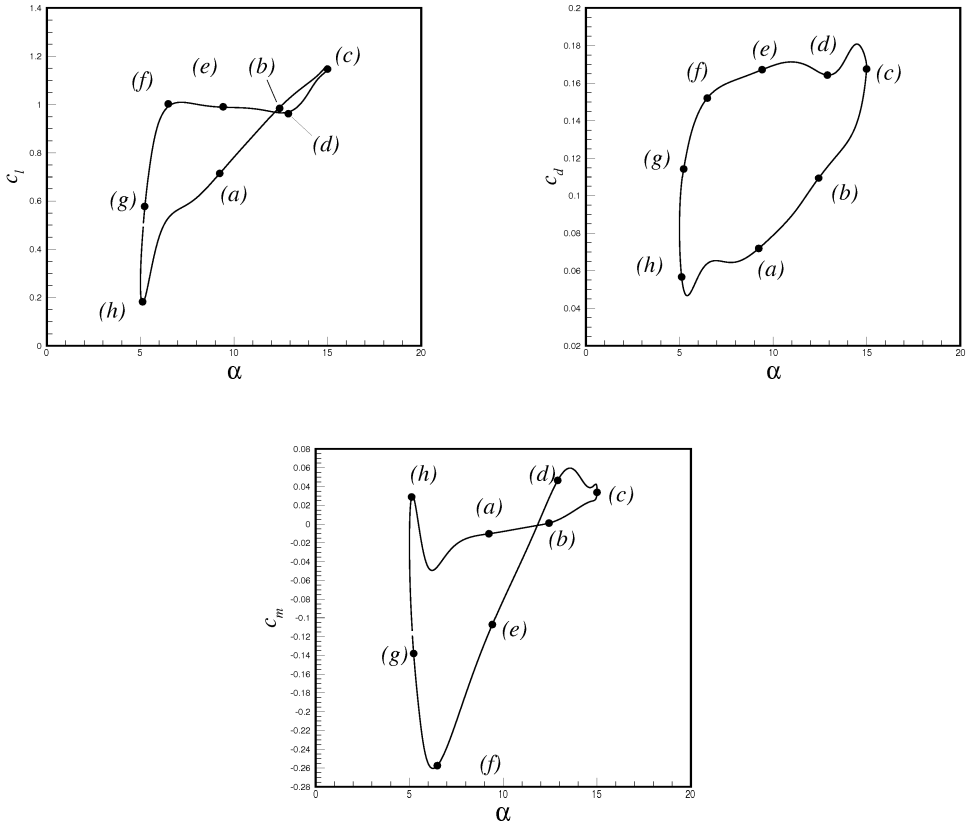

Figure 5.24: Unsteady turbulent flow. $Re = 1.3 \cdot 10^5$, $\alpha = 10° + 5° \sin(2kt)$, $k = 0.5$. Identification of some specific points on the aerodynamic coefficient loops. (a), C_l ; (b), C_d ; (c), C_m .

in the middle region of the airfoil extends.

- Phase (c)-(d). $\alpha = 15° \div 12.9°$. The lift decreases and, in the point (d), reaches a local minimum. The drag curve shows a maximum after the point (d) and then decreases. A similar behaviour is observed on the moment curve. From the pressure coefficient diagrams, the DSV is clearly detected along the airfoil chord. In the point (d), the flow is separated for the 60% of the chord.

- Phase (d)-(e). $\alpha = 12.9° \div 9.4°$. After the local minimum, the lift increases even if the angle of attack is decreasing. The drag is approx-

imately constant while a strong loss in the moment curve is achieved. The DSV is convected along the airfoil chord by distorting the pressure distribution. The secondary vortices produce a partial flow reattachment in the rear part of the DSV. In the point (e), the DSV is approximately at $x = 0.5c$. The separated flow extends for the 80% of the chord.

- Phase (e)-(f). $\alpha = 9.4° \div 6.5°$. The lift continues to increase and in the point (f) obtains another relative maximum. Simultaneously, the drag decreases and the moment coefficient collapses. The moment stalls in the point (f) because of the unbalanced pressure expansion associated with the DSV position. The partial reattachment of the flow, visible in the middle part of the chord, is due to the secondary vortices behind the DSV.

- Phase (f)-(g). $\alpha = 6.5° \div 5.3°$. A rapid loss of lift and drag is visible, accompanied by a moment recovery. The DSV leaves the airfoil surface and moves toward the turbulent wake. The C_f diagram in the point (g) reveals a small reattachment of the flow at the leading edge.

- Phase (g)-(h). $\alpha = 5.3° \div 5.1°$. In this phase, a further decrease of the lift is achieved. The drag follows the same evolution while the moment coefficient takes a local maximum in the point (h). A small expansion in the pressure distribution is visible by the C_P diagram in the points (g) and (h), which correspond to the onset of the flow reattachment. The remaining part of the flow is still separated. Between the points (h) and (a), the flow has not the time to complete the reattachment process. The secondary vortices persist on the surface when α begins to increase.

The *deep stall* case exhibits some differences but also several analogies with the *light stall* one. The main angle of attack is such that a partial separation remains in the airfoil surface during all the cycle. Also for the *deep stall* case, the DSV is formed from the LSB, but the scale of the separations is much

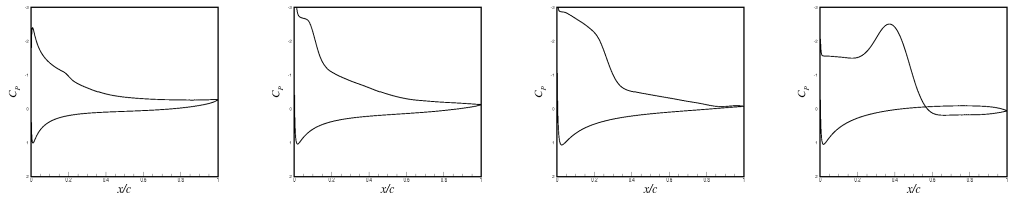

(a) $\alpha = 9.3°$ (b) $\alpha = 12.5°$ (c) $\alpha = 15°$ (d) $\alpha = 12.9°$

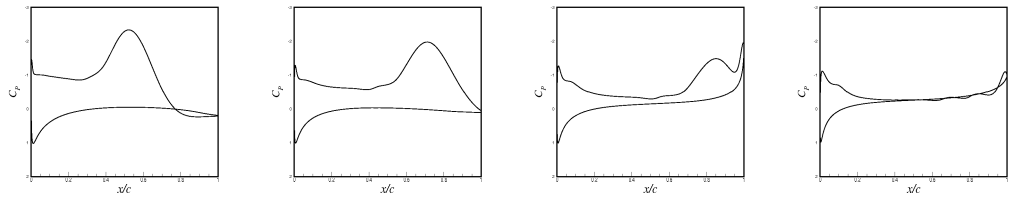

(e) $\alpha = 9.4°$ (f) $\alpha = 6.5°$ (g) $\alpha = 5.3°$ (h) $\alpha = 5.1°$

Figure 5.25: Unsteady turbulent flow. $Re = 1.3 \cdot 10^5$, $\alpha = 10° + 5° \sin(2kt)$, $k = 0.5$. C_P diagrams in different phases.

higher than the *light stall* . The high reduced frequency of the pitching motion is comparable with the Strouhal number of the natural vortex shedding of the flow. Finally, also in this case, the stall of the moment occurs before of the lift one.

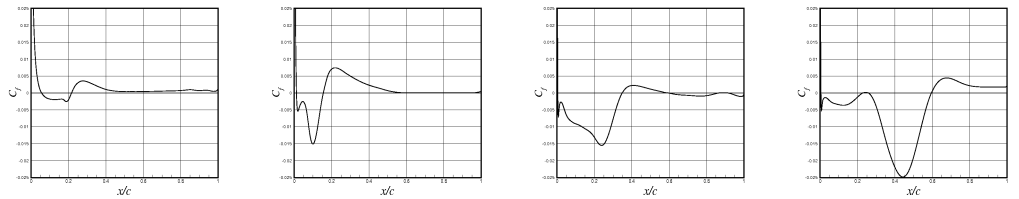

(a) $\alpha = 9.3°$ (b) $\alpha = 12.5°$ (c) $\alpha = 15°$ (d) $\alpha = 12.9°$

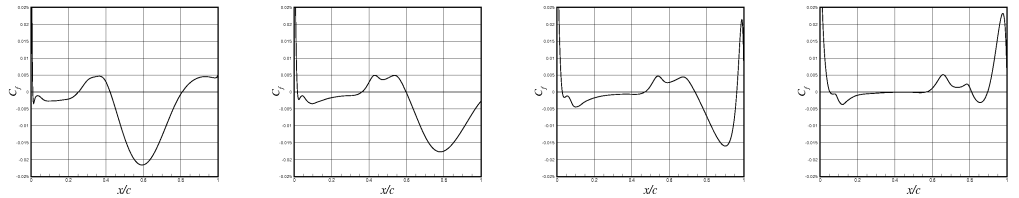

(e) $\alpha = 9.4°$ (f) $\alpha = 6.5°$ (g) $\alpha = 5.3°$ (h) $\alpha = 5.1°$

Figure 5.26: Unsteady turbulent flow. $Re = 1.3 \cdot 10^5$, $\alpha = 10° + 5° \sin(2kt)$, $k = 0.5$. C_f diagrams in different phases.

5.5 Some comments

The CFD simulations of the flow around an oscillating airfoil has been performed. The flow conditions reproduce a recent experimental test at low Reynolds number. The numerical simulation of such a flow is complicated by the coexistence of laminar and turbulent regions on the airfoil surface. The problem increases in the oscillating airfoil cases. The use of very low values of the free stream turbulence parameters has allowed the achievement of a natural (i.e. numerical) transition on the airfoil surface without fixing the transition point. This approach has been used for the steady analysis as well as for the dynamic one. The comparisons with the experimental data have shown several inconsistencies explained, in part, through three dimensional static simulations. The pitching conditions taken into account correspond to a *pre stall* , *light stall* , and a *deep stall* flow regime. For the latter, the agreement with an high accuracy numerical solution (LES) has confirmed the reliability of the present RANS simulation in predicting such complex flows. The DSV produces an increase of the lift and causes an anticipated moment stall.

The analyses and the discussions of the oscillating airfoil results have been carried out by exploiting a *near field* point of view, without a quantitative correlation with the flow field evolution. This issue will be addressed in the next chapter.

Chapter 6

Far Field Analysis of Oscillating Airfoil Flows

This chapter deals with the use of the *far field* technique on the turbulent flow simulations around oscillating airfoils. With respect to the results showed in chapter 4, the contribution associated with the time rate of change of the hydrodynamic impulse has to be taken into account. The body acceleration term is non zero as well and represents the *virtual* mass of the body. An intensive post-processing analysis is carried out by storing the flow field at each time instant during the last oscillation period. The time derivative of the vorticity field is computed *a posteriori* by a forward formula accurate at the second order. By referring to the scheme (4.3) in §4, a proper location of the external surfaces Σ_I and Σ_J has been considered in the computation of the *far field* integrals (4.52). In particular, the surface Σ_I is located just downstream of the airfoil trailing edge ($x_S \sim 0$), and the surface Σ_J is outside of the boundary layer thickness ($y_S > \delta$). The breakdown of the aerodynamic force in its main contributions is also presented.

6.1 Far field analysis of the aerodynamic force

6.1.1 Pre stall case

The unsteady flow solution obtained at $Re = 1.35 \cdot 10^5$, $M = 0.1$, with $\alpha = 7.5^\circ \sin(2kt)$ and $k = 0.05$ is analyzed. In figures (6.1) the aerodynamic coefficients C_l and C_d, computed both with the *near field* and the *far field*

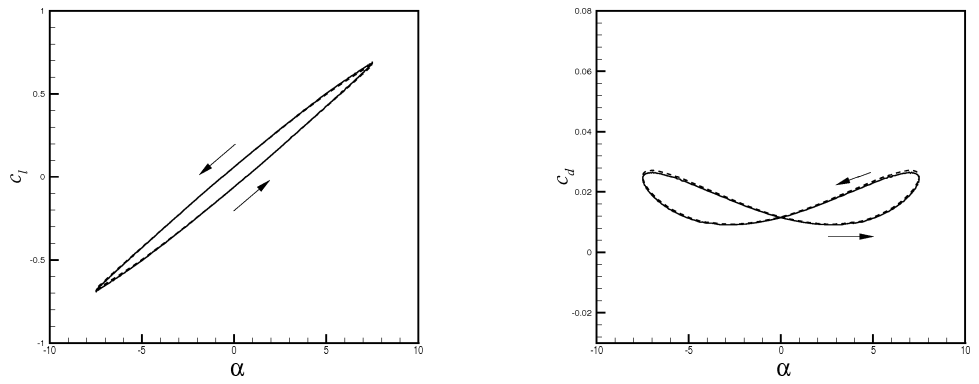

(a) (b)

Figure 6.1: Unsteady turbulent flow. $Re = 1.35 \cdot 10^5$, $\alpha = 7.5° \sin(2kt)$, $k = 0.05$. − − − , *near field* method; —, *far field* method. (a), $C_l - \alpha$ curve; (b), $C_d - \alpha$ curve.

methods, are reported. As may be seen from figures (6.1a) and (6.1b), a very satisfactory agreement has been achieved. The lift and drag hysteresis curves obtained from the *near field* integration are faithfully reproduced by the *far field* integration. The equations (4.52) represent an alternative way to the *near field* computation of the aerodynamic force also in case of an oscillating airfoil. The viscous and turbulent terms, $\langle \underline{\mathbf{F}}_{II} \rangle$ and $\langle \underline{\mathbf{F}}^t \rangle$, can be avoided in the computation because of the absence of massive flow separations intersecting the Σ_I surface. By analyzing the single components contained in equations (4.52a) and (4.52b), it is interesting to observe the part of the lift and drag associated with the vortex force integrals (i.e. $(C_l)_\Omega$ and $(C_d)_\Omega$). Such contributions are reported in figures (6.2a) and (6.2b). As may be seen, the vortex force takes into account for the main part of the circulation. The hysteresis cycle is slightly enlarged with respect to the total lift coefficient. Besides, the same effects on the drag coefficients are negative, as it can be noted in figure (6.2d). The vortex force appears as a thrust on the airfoil surface. The lift and drag are compensated by the terms computed on Σ, reported in figures (6.2b) and (6.2e). The drag term $(C_d)_\Sigma$ accounts for the main part of the aerodynamic resistance. In figures (6.2c) and (6.2f), the rate of change of the hydrodynamic impulse contributions, $(C_l)_{\dot{\omega}}$ and

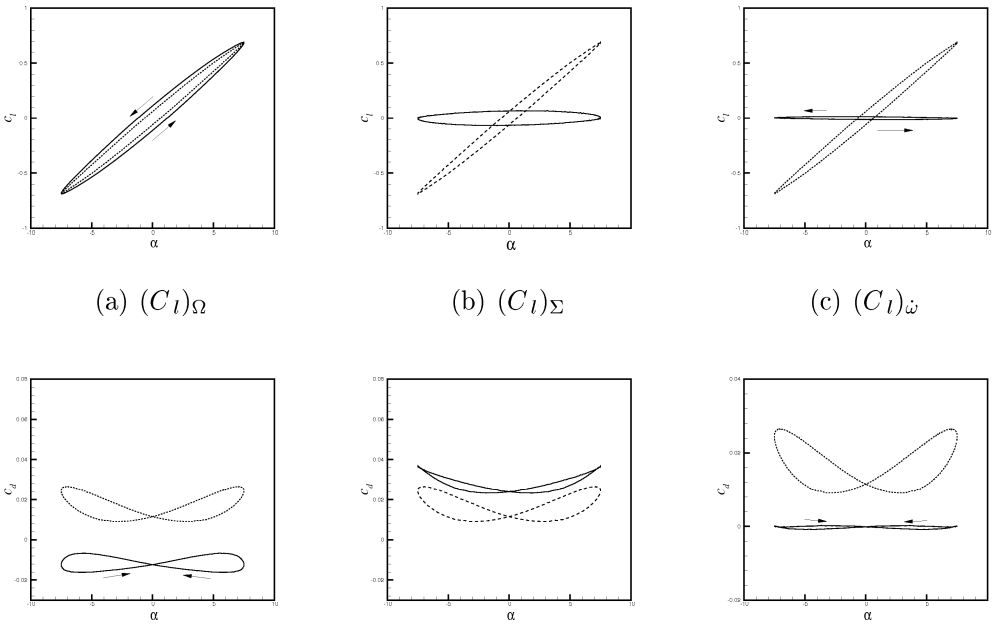

(a) $(C_l)_\Omega$ (b) $(C_l)_\Sigma$ (c) $(C_l)_{\dot{\omega}}$

(d) $(C_d)_\Omega$ (e) $(C_d)_\Sigma$ (f) $(C_d)_{\dot{\omega}}$

Figure 6.2: Unsteady turbulent flow. $Re = 1.35 \cdot 10^5$, $\alpha = 7.5° \sin(2kt)$, $k = 0.05$. Breakdown of the aerodynamic coefficients. $--$, *near field* method; —, *far field* integrals

$(C_d)_{\dot{\omega}}$ are plotted. They represent the integrated effects of the vorticity displacement and are fairly small with respect to the other contributions. The *non circulatory* behaviour of these terms is highlighted because of the zero net mean value over the entire cycle. The solid body acceleration terms, $(C_l)_B$ and $(C_d)_B$, (not reported), are negligible because of the small reduced frequency of the specific case.

6.1.2 Light stall case

In this section, the *light stall* solution achieved at $Re = 1.35 \cdot 10^5$, $M = 0.1$, $\alpha = 5° + 10° \sin(2kt)$ and $k = 0.05$, is discussed by using the *far field* integrals in the equations (4.52). In such a case, the *light stall* is characterized by large zones of separated flow during a portion of the cycle. The lift and drag curves, obtained with the *near field* and the *far field* methods, are reported in figures (6.3a) and (6.3b). The aerodynamic force computed with the *far field* is in

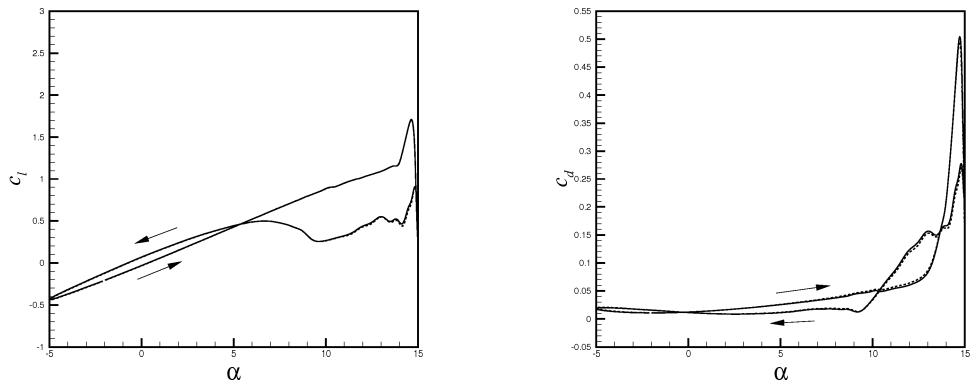

(a) (b)

Figure 6.3: Unsteady turbulent flow. $Re = 1.35 \cdot 10^5$, $\alpha = 5° + 10° \sin(2kt)$, $k = 0.05$. $--$, *near field* method; —, *far field* method. (a), $C_l - \alpha$ curve; (b), $C_d - \alpha$ curve.

a very good agreement with the *near field* one. Also in this case, the viscous and turbulent terms associated with the integrals $\langle \underline{\mathbf{F}}_{II} \rangle$ have a secondary effect in the computation of the aerodynamic force. In the figures (6.4a) and (6.4b), the $(C_l)_\Omega$ and $(C_d)_\Omega$ associated with the vortex force are reported. The Lamb vector integrals account for the main part of the total lift. The main slope of the hysteresis cycle is reproduced also in the zone of the stall. In the linear part of the cycle, instead, a similar behaviour to the *pre stall* case is observed. The maximum value obtained in the $(C_l)_\Omega$ exceeds the $C_{l\,max}$. Conversely, the remaining contributions, $(C_l)_\Sigma$ and $(C_d)_\Sigma$, are associated with the shedding of the vorticity in the wake. During the stalled portion of the cycle, strong oscillations are visible in figures (6.4b) and(6.4e) . In figures (6.4c), the peaks, visible in the $(C_l)_{\dot{\omega}}$ curve, point out the detachment and the convection of vorticity downstream the airfoil. Such oscillations increase during the reattachment phase. A sort of compensation between $(C_l)_\Sigma$ and $(C_l)_{\dot{\omega}}$ occurs. As for the previous test, the solid body acceleration terms, $(C_l)_B$ and $(C_d)_B$, have a negligible effect on total aerodynamics force.

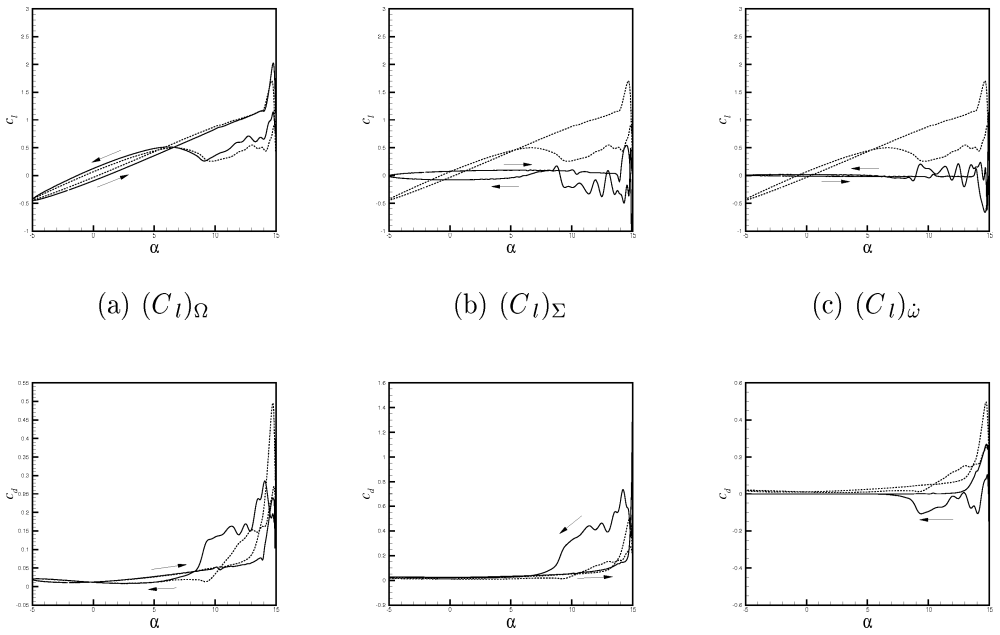

(a) $(C_l)_\Omega$ (b) $(C_l)_\Sigma$ (c) $(C_l)_{\dot{\omega}}$

(d) $(C_d)_\Omega$ (e) $(C_d)_\Sigma$ (f) $(C_d)_{\dot{\omega}}$

Figure 6.4: Unsteady turbulent flow. $Re = 1.35 \cdot 10^5$, $\alpha = 5° + 10° \sin(2kt)$, $k = 0.05$. $--$, *near field* method; —, *far field* method.

6.1.3 Deep stall case

The *far field* method is applied to the *deep stall* case discussed in chapter 5. The flow solution was achieved at $Re = 1.3 \cdot 10^5$, $M = 0.3$, and $\alpha = 10° + 5° \sin(2kt)$ with $k = 0.5$. Even if the compressibility effects of this test are significant, they are confined in the leading edge zone of the airfoil. The application of the *far field* integrals in equation (4.52) provide the hysteresis curves depicted in figures (6.5a) and (6.5b). A satisfactory agreement is visible also in this case. The major discrepancies are observed in the lift curve in the lower angles of the periodical motion, and on the drag curve at the higher angles of attack. For such a case, the terms associated with $\langle \underline{\mathbf{F}}_{II} \rangle$ and $\langle \underline{\mathbf{F}}^t \rangle$ have to be taken into account because of the massive flow separations. In figures (6.6), the breakdown of the aerodynamic coefficients is reported. Very unusual hysteresis loops are visible in each contribution that make difficult the physical interpretation. The role of each term is

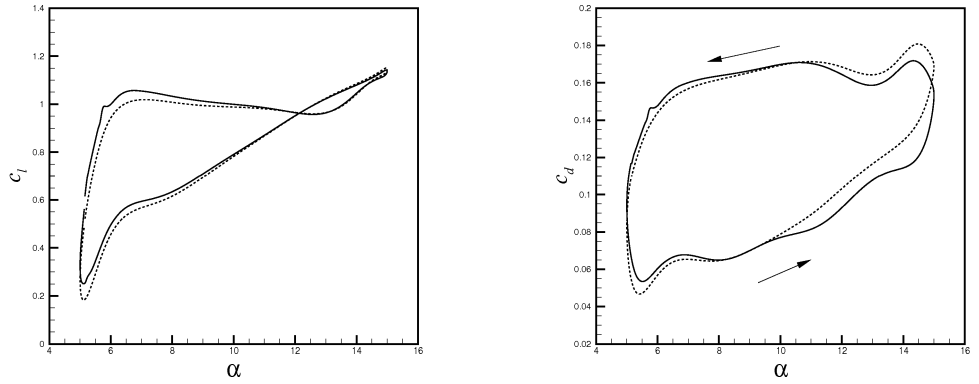

(a) (b)

Figure 6.5: Unsteady turbulent flow. $Re = 1.3 \cdot 10^5$, $\alpha = 10° + 5° \sin(2kt)$, $k = 0.5$. $- - -$, *near field* method; ——, *far field* method. (a), $C_l - \alpha$ curve; (b), $C_d - \alpha$ curve.

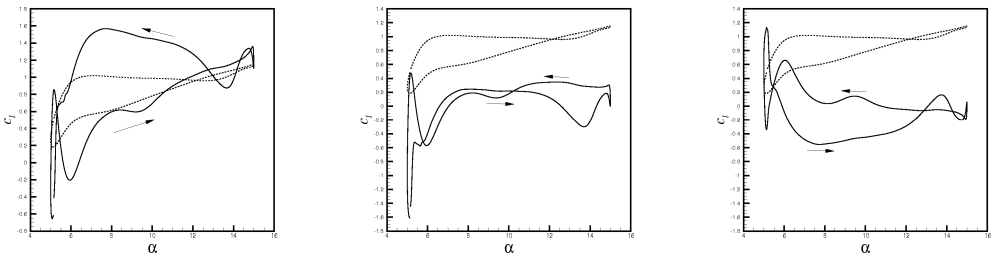

(a) $(C_l)_\Omega$ (b) $(C_l)_\Sigma$ (c) $(C_l)_{\dot{\omega}}$

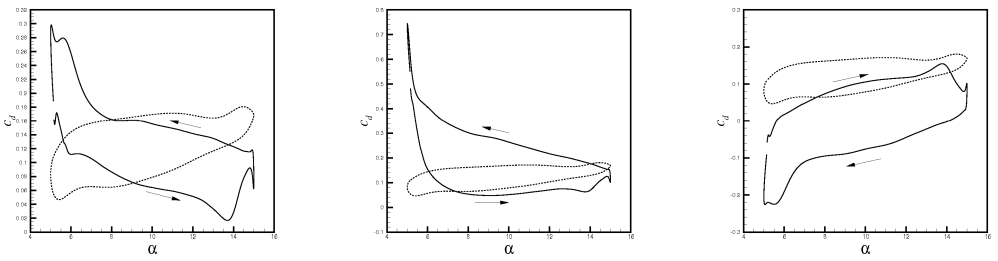

(d) $(C_d)_\Omega$ (e) $(C_d)_\Sigma$ (f) $(C_d)_{\dot{\omega}}$

Figure 6.6: Unsteady turbulent flow. $Re = 1.3 \cdot 10^5$, $\alpha = 10° + 5° \sin(2kt)$, $k = 0.5$. $- - -$, *near field* method; ——, *far field* method.

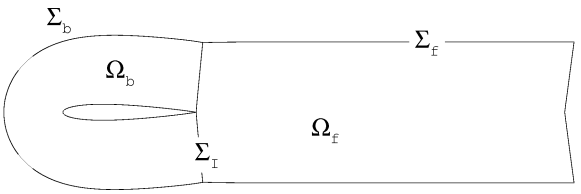

Figure 6.7: Identification of the *bound* and *free* vorticity.

no well distinguished as for the previous cases. The Lamb vector integrals account only for a part of the aerodynamic force. The surface terms $(C_l)_\Sigma$ and $(C_d)_\Sigma$ point out that a significant part of the vorticity is shed through the wake surface. A substantial difference with respect to the previous cases is due to the rate of change of the hydrodynamic impulse terms, $(C_l)_{\dot{\omega}}$ and $(C_d)_{\dot{\omega}}$, reported in figures (6.6c) and (6.6f). They contribute for a significant part during the entire cycle.

6.2 Vorticity decomposition

The possibility to detect the contributions associated with the *bound* and *free* vorticity is discussed in the following. As pointed in chapter 3, an inviscid flow around an oscillating airfoil is characterized by a release of *free* vorticity $\underline{\omega}^f$ in the wake. This vorticity is responsible for the time delay between the aerodynamic force and the airfoil angular position, and it is superimposed to the *bound* vorticity $\underline{\omega}^b$ associated with the airfoil surface. Also in case of the turbulent oscillating airfoil solutions, the Lamb vector integrals allows for a decomposition of the aerodynamic force of kind $C_l = C_l^f + C_l^b$, where C_l^f and C_l^b are the contributions associated with $\underline{\omega}^f$ and $\underline{\omega}^b$ respectively. The *advection* form of the aerodynamic force is used to address these scopes.

By referring to the scheme (6.7), the volume of integration is subdivided

in two zones, Ω_b and Ω_f, such that $\Omega = \Omega_b \cup \Omega_f$. The aerodynamic force is computed by integrating over Ω_b and Ω_f equivalently. Consider a decomposition of kind:

$$\underline{\mathbf{F}} = \underline{\mathbf{F}}_b + \underline{\mathbf{F}}_f \tag{6.1}$$

where $\underline{\mathbf{F}}_f$ is the vortex force exerted on the body by the free vorticity:

$$\underline{\mathbf{F}}_f = \int_{\Omega_f} \underline{\omega}^f \times \underline{\mathbf{u}}\, dV \tag{6.2}$$

In the vortex force definition (6.2), the sign is changed with respect to the standard definition because Ω_f does not contain B. To identify $\underline{\mathbf{F}}_b$ and $\underline{\mathbf{F}}_f$, we apply the definition of the aerodynamic force to Ω_b and to $\Omega_b \cup \Omega_f$. The following relation is achieved:

$$\begin{aligned} \underline{\mathbf{F}} &= -\int_{\Omega_b} \underline{\omega}^b \times \underline{\mathbf{u}}\, dV - \int_{\Sigma_b \cup \Sigma_I} \underline{\mathbf{r}} \times \underline{n} \times (\, \underline{\omega}^b \times \underline{\mathbf{u}}\,)\, dS = \\ &= -\int_{\Omega_b} \underline{\omega}^b \times \underline{\mathbf{u}}\, dV - \underline{\mathbf{F}}_f - \int_{\Sigma_f} \underline{\mathbf{r}} \times \underline{n} \times (\, \underline{\omega}^f \times \underline{\mathbf{u}}\,)\, dS \\ &- \int_{\Sigma_b} \underline{\mathbf{r}} \times \underline{n} \times (\, \underline{\omega}^b \times \underline{\mathbf{u}}\,)\, dS \end{aligned} \tag{6.3}$$

from that

$$\underline{\mathbf{F}}_f = -\int_{\Sigma_f} \underline{\mathbf{r}} \times \underline{n} \times (\, \underline{\omega}^f \times \underline{\mathbf{u}}\,)\, dS + \int_{\Sigma_I} \underline{\mathbf{r}} \times \underline{n} \times (\, \underline{\omega}^b \times \underline{\mathbf{u}}\,)\, dS \tag{6.4}$$

If the surface Σ_f is sufficiently far its contribution is negligible, and the *free* vorticity force is detected:

$$\underline{\mathbf{F}}_f = \int_{\Sigma_I} \underline{\mathbf{r}} \times \underline{n} \times (\, \underline{\omega} \times \underline{\mathbf{u}}\,)\, dS \tag{6.5}$$

where $\underline{\omega}^f$ and $\underline{\omega}^b$ are equal on Σ_I. The *bound* vorticity contribution instead is given for difference by:

$$\underline{\mathbf{F}}_b = \underline{\mathbf{F}} - \int_{\Sigma_I} \underline{\mathbf{r}} \times \underline{n} \times (\, \underline{\omega} \times \underline{\mathbf{u}}\,)\, dS \tag{6.6}$$

Thus, the force associated to the *bound* and *free* vorticity are defined. The

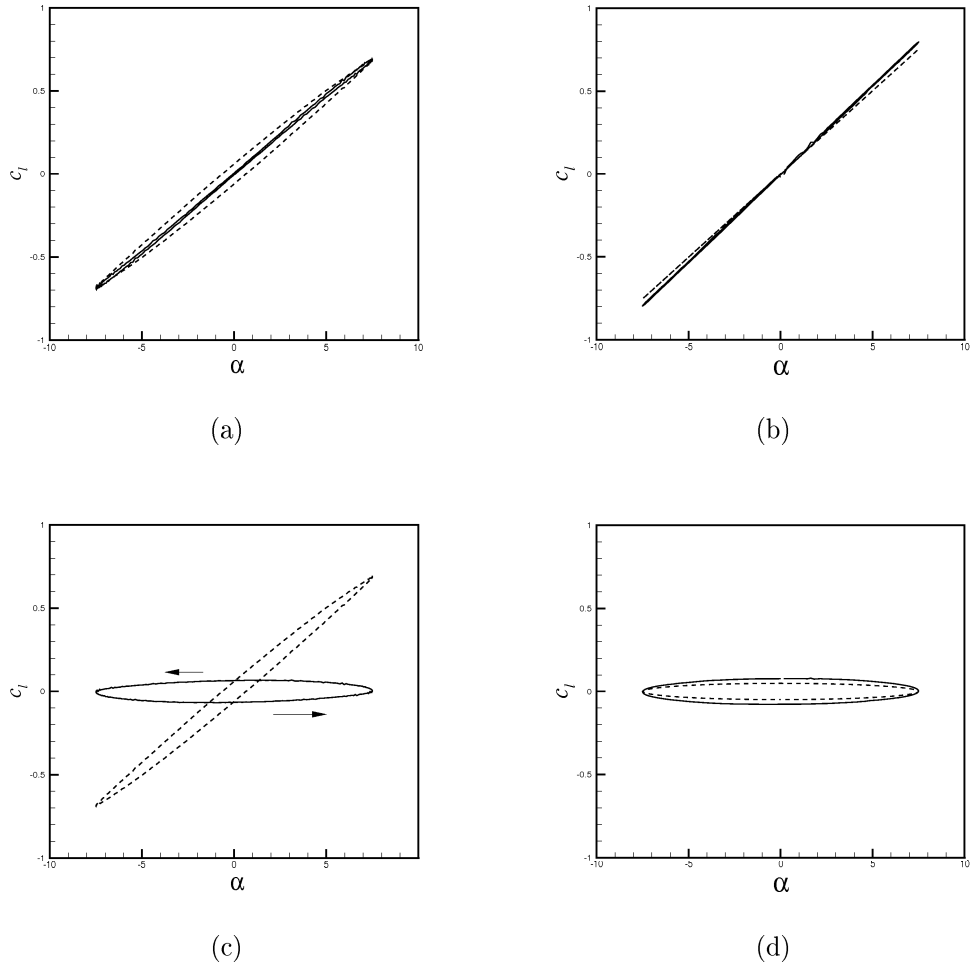

Figure 6.8: *Bound* and *free* decomposition. (a) and (c), turbulent flow solution. (b) and (d), inviscid flow solution. (a), *bound* vorticity, $-$, *far field* decomposition, $- - -$ *near field* ; (b), *bound* vorticity $-$, *far field* decomposition, $- - -$ Theodorsen solution; (c), *free* vorticity $-$, *far field* decomposition, $- - -$ *near field* ; (d), *free* vorticity $-$, *far field* decomposition, $- - -$ Theodorsen solution;

verification of these concepts has been made by referring first to an unsteady inviscid flow solution, and then to the turbulent viscous case (*pre stall*). The analytical solution provided by Theodorsen, expressed in equation (3.118), has also been used as a reference. For small values of the reduced frequency, it can be assumed that the real and imaginary parts of equation (3.118) provide the contribution of the *bound* vorticity $\underline{\omega}^b$ and of the *free* vorticity

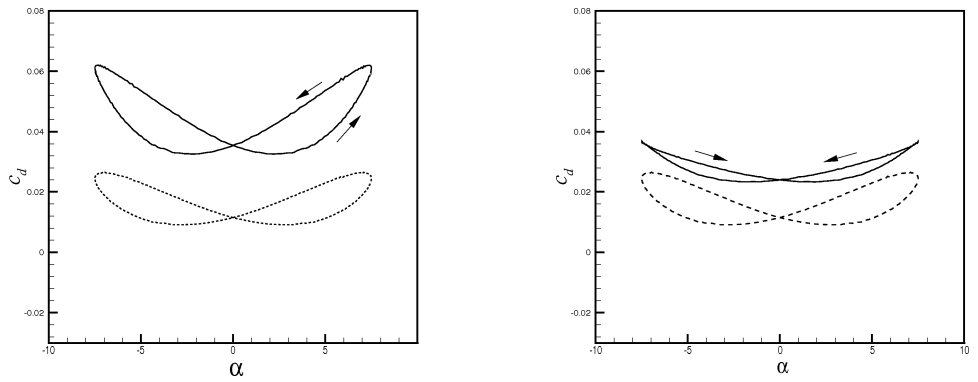

(a) (b)

Figure 6.9: Unsteady turbulent flow. $Re = 1.35 \cdot 10^5$, $\alpha = 7.5° \sin(2kt)$, $k = 0.05$. Drag decomposition. (a) —, *bound* vorticity contribution; $--$, *near field* data. (b) —, *free* vorticity contribution; $--$, *near field* data.

$\underline{\omega}^f$ to the total lift.

These contributions are plotted in figures (6.8). In the plot (6.8a), the $(C_l)_b$ contribution is compared with the total lift coefficient. It can be observed that the *bound* vorticity provides a contribution in phase with respect to the instantaneous angular position α. In figure (6.8b), the same comparison is made for the inviscid flow solution and the curve provided by Theodorsen. The differences in the shape of the hysteresis curve are due to the thickness effects of the airfoil, not taken into account by Theodorsen's theory. The *free* vorticity effects are reported in figures (6.8c) and (6.8d). This contribution represents the isolated effect of the free vorticity $\underline{\omega}^f$ released by the airfoil. The agreement between the curves shows the ability of equation (4.52) in detecting the contribution C_l^f. The time lag effect of C_l^f is clearly visible in both the viscous and the inviscid flow solutions. The non circulatory nature of this contribution is highlighted by the zero mean value over the period T. By applying such decomposition to the drag components, the curves C_d^b and C_d^f are showed in figures (6.9a) and (6.9b). The *bound* vorticity drag C_d^b is shifted toward higher values with respect to the *near field* data, while the drag associated with the *free* vorticity has a smaller role.

6.3 The dynamic stall vortex

As point out in chapter 5, the *near field* method allows for an analysis based solely on the superficial distributions of pressure and skin friction coefficients. The *far field* method permits to observe the same phenomenon under a different perspective. One of the main concerns of the studies on the dynamic stall regards the identification of the DSV properties. In particular, a significant problem is the definition of the dynamic stall onset in terms of the angular position. This turns out useful for the designers as well as for the tuning of more refined semi-empirical models. For example, the Beddoes-Leishman model, [49], makes use of several semi-empirical constants to characterize the dynamic stall vortex. A better definition of some parameters can improve the quality of the results, as Sheng et al. ([89]) have demonstrated. The most widely used criterion to detect the DSV onset is based on the observation of the pitching moment curve. When a drop of 0.05 in the C_m value occurs, the dynamic stall onset is identified. Other methods consider the lift curve slope and define the onset of the dynamic stall in the point where the C_{l_α} changes. Procedures based on the pressure coefficient distributions are used as well.

By using the present *far field* method, an alternative way to accomplish this task is proposed. By exploiting the definition of the centroid of a vorticity distribution (Saffman, [71]),

$$\underline{\mathbf{x}}_V = \int_\Omega \frac{(\underline{\mathbf{r}} \times \underline{\omega}) \cdot \underline{\mathbf{I}}}{I^2} \, \underline{\mathbf{r}} \, dV \tag{6.7}$$

where $\underline{\mathbf{I}}$ is the hydrodynamic impulse, defined in (3.24) the movement of the DSV center results to be associated with $\underline{\mathbf{x}}_V$. In fact, the velocity of the centroid is given by its time derivative:

$$\underline{\mathbf{U}}_V = \frac{d\,\underline{\mathbf{x}}_V}{dt} = \frac{d}{dt} \int_\Omega \frac{(\underline{\mathbf{r}} \times \underline{\omega}) \cdot \underline{\mathbf{I}}}{I^2} \, \underline{\mathbf{r}} \, dV \tag{6.8}$$

In equation (6.8), the contribution of the aerodynamic force associated with the rate of change of the hydrodynamic impulse is recognizable. In fact, it

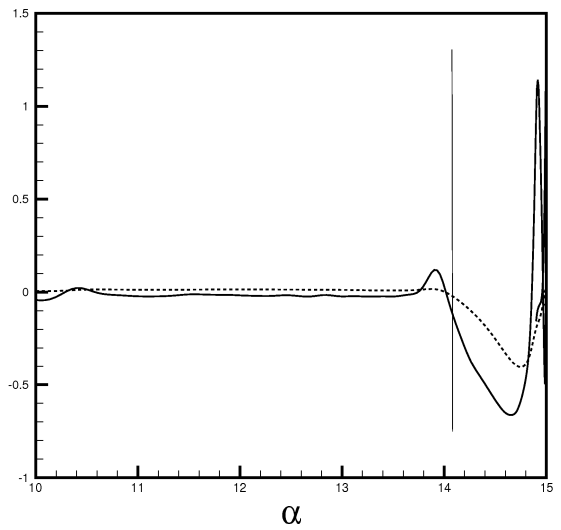

Figure 6.10: Unsteady turbulent flow. $Re = 1.35 \cdot 10^5$, $\alpha = 5° + 10° \sin(2kt)$, $k = 0.05$. Dynamic Stall onset criterion . —, $(C_l)_{\dot{\omega}}$. − − − moment curve.

results a proportionality of kind:

$$\underline{\mathbf{U}}_V \sim \int_\Omega \underline{\mathbf{r}} \times \frac{\partial \underline{\omega}}{\partial t}\, dV \tag{6.9}$$

Thus, the effects of the vorticity convection can be detected by observing the time history of the contributions $(C_l)_{\dot{\omega}}$ and $(C_d)_{\dot{\omega}}$. The application of this method has been made by referring to the *light stall* case. In figure (6.10), the term $(C_l)_{\dot{\omega}}$ is reported during the α-increasing phase and compared with the moment curve in the interval $10° \leq \alpha \leq 15°$. The correspondence between the c_m curve and the $(C_l)_{\dot{\omega}}$ is visible. As may be seen in the figure, the curve of $(C_l)_{\dot{\omega}}$ is fairly flat up to 13.8°. First, a positive peak is observed followed by a strong negative drop. Simultaneously, the pitching moment curve has a similar behaviour and takes a minimum approximately in the same angular position of $(C_l)_{\dot{\omega}}$. In order to computed the DSV onset, the analogy between $(C_l)_{\dot{\omega}}$ and c_m curves is useful because it allows to avoid the computation of the pitching moment.

Another useful information regards DSV convection speed. The first experimental studies indicated that the DSV is convected at a velocity between

$1/3U_\infty$ and $1/2U_\infty$. In 1990, Chandrasekhara and Carr [90] made a systematic study on the DSV convection as function of the reduced frequency and the Mach number confirming this observation. Also in the experiment of Lee [80] it is reported a convection speed of $0.45U_\infty$ for a case with $k = 0.1$. As already observed in the previous chapter, the DSV location can be identified through the distortion of the pressure distribution over the airfoil surface. Here, by making use of the equations (6.7) and (6.8), the velocity observed through the *far field* approach is calculated and compared with the location of the maximum negative pressure peak on the airfoil surface (*near field* point of view). Such comparisons are reported in figures (6.11) for both the *light stall* and the *deep stall* case. In figure (6.11a), the position of the DSV is reported as function of α. It can be observed that the vorticity distribution initially is located in the first half of the airfoil chord. As α increases, it moves downstream and for $\alpha \geq 14°$ convects toward the trailing edge. In figure (6.11b), the velocity of DSV is reported and compared with the *near field* data. For $\alpha \leq 13°$ the vorticity centroid moves at a slow constant rate. For $\alpha > 13°$, a sudden increase in the velocity is observed. Then, the DSV is formed and convected at a speed of $0.15U_\infty$ approximately. The *near field* method provides a slightly higher convection speed. These values, however, disagree with the experimental observations.

For the *deep stall* case a similar analysis is presented. In such a case, the DSV is formed and convected during the α-decreasing phase. The DSV appears around at 13° and, as α decreases, it moves toward the trailing edge. The convection velocity obtained by the *far field* method is underestimated with respect to the *near field* information.

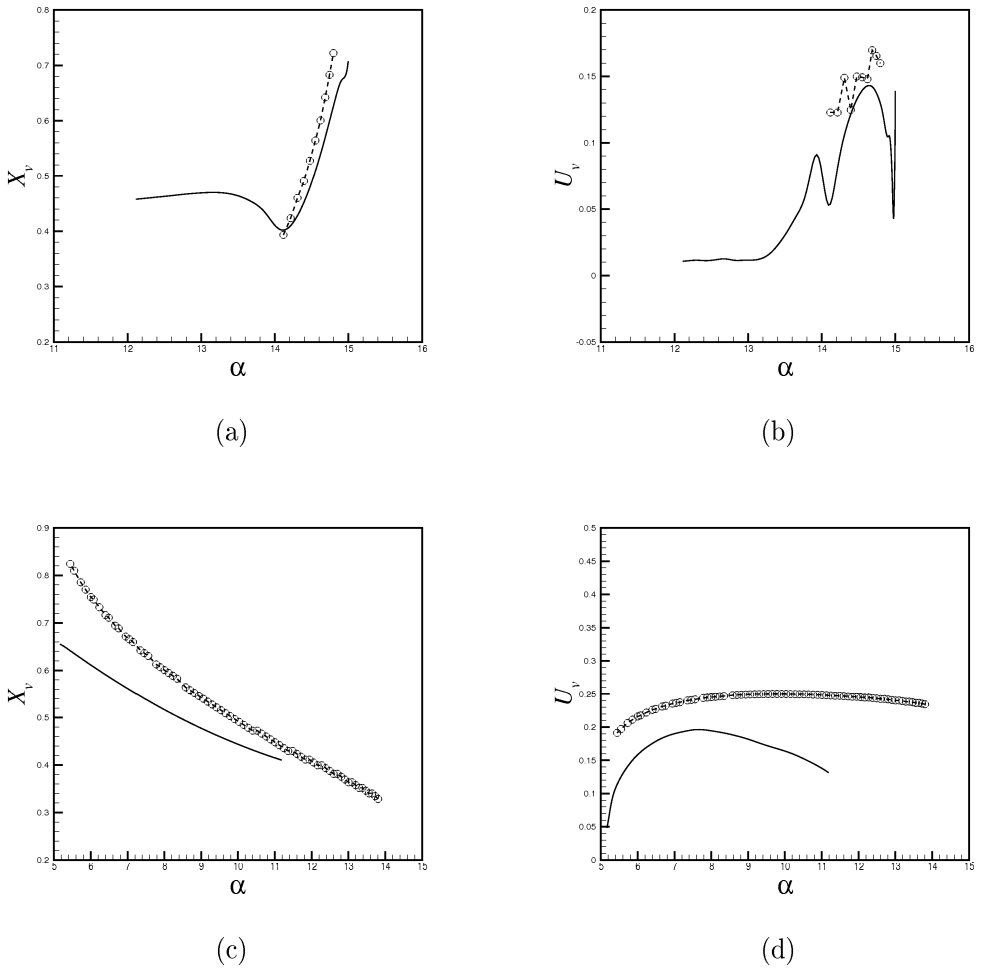

Figure 6.11: Unsteady turbulent flow. Position and velocity of the DSV. – – –, *near field* method; ——, *far field* method. (a), position of DSV, *light stall* ; (b), velocity of DSV, *light stall* ; (c), position of DSV, *deep stall* ; (d), velocity of DSV, *deep stall* .

Chapter 7

Conclusions

The present thesis has described the work carried out on the prediction of the aerodynamic force for oscillating airfoils. The aims were to provide a contribution in the physical interpretation of the fundamental mechanisms of the aerodynamic force generation. This objective has been accomplished by exploiting both theoretical results and numerical solutions.

A series of numerical flow solutions around an oscillating airfoil has been obtained at low Reynolds number. The transitional flow regime has been simulated by an unsteady RANS solver using the $\kappa - \omega$ turbulence models. Several pitching conditions have been analyzed by referring to a new set of experimental data. The preliminary static analysis has permitted to discover three dimensional effects in the experimental measurements of the flow. The simulation of the effective experimental apparatus has confirmed this assertion. The *pre stall* , *light stall* , and *deep stall* flow regimes have been discussed. The reliability of the present RANS simulations in predicting such complex flows has been confirmed through other data set. An intensive post processing activity has allowed the identification of the main flow features of the dynamic stall.

The use of the *far field* methods has become much popular both in experimental and numerical aerodynamics. The reasons of such a success are severals. However, many *far field* methods apply solely to steady flows. In this thesis, it has been developed a *far field* method to analyze the aerodynamic force on the oscillating airfoil. The theory on which this analysis is founded, was initially developed for flows governed by the unsteady Navier

Stokes equations. In the present work, the theory has been extended and verified to flows governed by the Reynolds Averaged Navier Stokes equations. It has been shown that in case of boundary layer approximation, some contributions of the complete expression of the aerodynamic force are negligible. The effect of the integration domain has been investigated at different Reynolds numbers and angles of attack. By decomposing the aerodynamic force in surface and volume contributions, it has been possible to identify the specific components to the total aerodynamic force.

The theory has been applied to the flow solutions obtained around the oscillating airfoil. The decomposition of the aerodynamic force into the volume and surface contributions has permitted to detect the effects of the *free* vorticity shed in the wake. Such a contribution has been identified by the Lamb vector integrals and compared with the analytical results provided by Theodorsen for an oscillating flat plate. In the *pre stall* case, the effects of the *bound* vorticity have also been recognized as the part in phase with the instantaneous angular position of the airfoil. In the dynamic stall case, this analysis provides useful information on the dynamic stall vortex, such as the position and the convection speed.

The *far field* method discussed in the present thesis represents a useful device for the analysis of the aerodynamic force. The applications carried out demonstrate the reliability of the approach as well as its coherence with other existing theories.

Bibliography

[1] Ham, N. D., 1968. Aerodynamic Loading on a Two-Dimensional Airfoil During Dynamic Stall. *AIAA Journal*, **6**, 1927–1934.

[2] Carr, L. W., 1988. Progress in Analysis and Prediction of Dynamic Stall. *Journal of Aircraft*, **25**, 1.

[3] Hanff, E. S. & Jenkins, S. B., 1990. Large-Amplitude High-Rate Roll Experiments on a Delta and Double Delta Wing. *28th Aerospace Sciences Meeting*, 8-11 Januray, Reno, AIAA 90-0224.

[4] Ferreira, C. S., van Kuik, G., van Bussel, G. & Scarano, F. , 2009. Visualization by PIV of dynamic stall on a vertical axis wind turbine. *Exp Fluids*, **46**, 97–108.

[5] von Karman, Th. & Burgers, J.M., 1935. *General Aerodynamic Theory.* Volume II, Springer.

[6] McCroskey, W. J., 1982. Unsteady Airfoils. *Annual Review Fluid Mech.*, **14**, 285–311.

[7] Leishman, J. G., 2002. Challenges in Modeling the Unsteady Aerodynamics of Wind Turbines. *21th ASME Wind Energy Symposium and the 40th AIAA Aerospace Sciences Meeting*, Reno, NV, AIAA 2002-0037.

[8] Leishman, J. G. , 2000. *Principles of Helicopter Aerodynamics.* Cambridge Univ. Press, New York.

[9] Ham, N. D. & Young, M. I. , 1966. Torsional Oscillation of Helicopter Blades Due to Stall. *Journal of Aircraft*, **3**, No. 3, 218–224.

[10] McCroskey, W. J., 1981. *The Phenomenon of Dynamic Stall.* NASA TM-81264.

[11] McCroskey, W. J., Carr, L. W. & McAlister K. W., 1976. Dynamic Stall Experiments on Oscillating Airfoils. *AIAA Journal*, **14**, No 1., 57–63.

[12] Ericsson, L. E. & Reding, J.P., 1976. Dynamic Stall Analysis in Light of Recent Numerical and Experimental Results. *Journal of Aircraft*, **13**, No. 4, 248–255.

[13] Ericsson, L. E. & Reding, J.P., 1977. Further Consideration of Spilled Leading-Edge Vortex Effects on Dynamic Stall. *Journal of Aircraft*, **14**, No. 6., 601–603.

[14] Ericsson, L. E. & Reding, J.P., 1980. Dynamic Stall at High Frequency and Large Amplitude. *Journal of Aircraft*, **17**, No 3, 136–142.

[15] Lorber, P. & Carta, F. , 1988. Airfoil Dynamic Stall at Constant Pitch Rate and High Reynolds Number. *Journal of Aircraft*, **25**, 548–556

[16] Carr, L. W. & Chandrasekhara, M. S., 1992. Design and Development of a Compressible Dynamic Stall Facility. *Journal of Aircraft*, **29**, No 29.

[17] Chadrasekhara, M. S., Wilder, M. C. & Carr, L. W., 1998. Competing Mechanism of Compressible Dynamic Stall. *AIAA Journal*, **36**, No 3.

[18] Greenblatt, D. & Wygnanski, I., 2001. Dynamic Stall Control by Periodic Excitation, Part 1: NACA0015 Parametric Study. *Journal of Aircraft*, **38**, No 3.

[19] Weaver, D., McAlister, K.W. & Tso, J., 2004. Control of VR-7 Dynamic Stall by Strong Steady Blowing. *Journal of Aircraft*, **41**, No. 6, 1404–1413.

[20] Post, M. L. & Corke, T. C., 2006. Separation Control Using Plasma Actuators: Dynamic Stall Vortex Control on Oscillating Airfoil. *AIAA Journal*, **44**, No. 12, 3125–3135.

[21] Panda, J. & Zaman, K. B. M. Q., 1994. Experimental investigation of the flow field of an oscillating airfoil and estimation of lift from wake surveys. *J. of Fluid Mech.*, **265**, 65–95.

[22] Noca, F., Shiels, D. & Jeon, D. , 1998. A comparison of methods for evaluating time-dependent fluid dynamic forces on bodies, using only velocity fields and their derivatives. *J. Fluids Struct.*, **13**, 551–578.

[23] Wernert, P., et al. , 1996. Experimental and numerical investigation of dynamic stall on a pitching airfoil. *AIAA Journal*, **34**, No. 5, 982–989.

[24] Ferreira, C. S., van Bussel, G., Scarano, F. & van Kuik, G., 2008. PIV Visualization of Dynamic Stall VAWT and Blade Load Determination. *46th AIAA Aerospace Sciences Meeting and Exhibit*, 7-10 January, Reno, Nevada, AIAA 2008-1317.

[25] Kurtulus, D. F., Scarano, F. & David, L., 2007. Unsteady aerodynamic forces estimation on a square cylinder by TR-PIV. *Exp. Fluids*, **42**, 185–196.

[26] Spalart, P. R., 2000. Strategies for turbulence modeling and simulations. *International Journal of Heat and Fluid Flow*, 21, pp. 252–263.

[27] Ekaterinaris, J. A. & Menter , F. R., 1994. Computation of Oscillating Airfoil Flows with One- and Two-Equation Turbulence Models. *AIAA Journal*, 32, No. 12, 2359–2465.

[28] Ekaterinaris, J. A., & Schiff, L. B., 1995. Navier-Stokes Solutions for an Oscillating Double-Delta Wing. *Journal of Aircraft*, 32, No. 2, 228–234.

[29] Spentzos, A., 2005. CFD analysis of 3D Dynamic Stall. *PHD Thesis*, University of Glasgow, Faculty of Engineering.

[30] Spentzos, A., Barakos, G., Badcock, K., Richards, B., Wernert, P., Schreck, S. & Raffael, M., 2005. Investigation of Three-Dimensional Dynamic Stall Using Computational Fluid Dynamics. *AIAA Journal*, **43**, No. 5.

[31] Spentzos, A., Barakos, G., Badcock, K., Richards, B., Coton, F., Galbraith, R. A., Berton, E. & Favier, D., 2007. Computational Fluid Dynamics Study of Three-Dimensional Dynamic Stall of Various Planform Shapes. *Journal of Aircraft*, 44, No. 4, 1118–1128.

[32] Hahn, S. , Duraisamy, K., Iaccarino, G., Nagarajan, S., Sitaraman, J., Wu, X. , Alonso, J. J., Baeder, J. D., Lele, S. K., Moin, P. & Schmits, F., 2006. Coupled high-fidelity URANS simulation for helicopter applications. *Annual Research Briefs*, Center for Turbulence Research, 73–82.

[33] Hahn, S., Anantham, S., Iaccarino, G., Baeder, J. D. & Moin, P., 2007. Coupled URANS simulation for the MDART rotor in forward flight. *Annual Research Briefs*, Center for Turbulence Research, 73–82.

[34] Choi, S., Alonso, J. J., Weide, E. & Sitaraman, J., 2007. Validation Study of Aerodynamic Analysis Tools for Design Optimization of Helicopter Rotors. *25th AIAA Applied Aerodynamics Conference June 25-28, Miami, FL*, AIAA 2007–3929.

[35] Ekaterinaris, J. A., 2002. Numerical Investigations of Dynamic Stall Active Control for Incompressible and Compressible Flows. *Journal of Aircraft*, **39**, No. 1, 71–78.

[36] Joo, W., Lee, B.S., Yee, K. & Lee, D. H., 2006. Combining Passive Control Method for Dynamic Stall Control. *Journal of Aircraft*, **43**, No 4.

[37] Ahn, T., Kim, C.& Rho, O. H., 2004. Dynamic-Stall Control Based on an Optimal Approach. *Journal of Aircraft*, **41**, No 5.

[38] Van Dyken, R. D., Ekaterinaris, J. A., Chandrasekhara, M. F., & Platzer, M. F., 1997. Analysis of Compressible Light Dynamic Stall Flow at Transitional Reynolds Numbers. *AIAA Journal*, 34, No. 7, 1420–1427.

[39] Geissler, W. & Haselmeyer, H., 2006. Investigation of dynamic stall onset. *Aerospace Science and Technology*, **10**, 590–600.

[40] Martinat, G., Brazaa, M., Hoaraub, Y. & Harran, G., 2008. Turbulence modelling of the flow past a pitching NACA0012 airfoil at 10^5 and 10^6 Reynolds numbers. *Journal of Fluids and Structures*, **24**, 1294–1303.

[41] Nagarajan, S., Hahn, S. & Lele, S. K., 2006. Prediction of Sound Generated by a Pitching Airfoil: A Comparison of RANS and LES. *12th AIAA/CEAS Aeroacoustics Conference 27th AIAA Aeroacoustics Conference*. 8 - 10 May 2006, Cambridge, Massachusetts, AIAA 2006-2516.

[42] Mavriplis, D. J. & al., 2008. Grid Quality and Resolution Issues from the Drag Prediction Workshop Series. *46th AIAA Aerospace Sciences Meeting and Exhibit*, 7-10 January 2008, Reno, Nevada, AIAA 2008-930.

[43] Laflin, K. R. & al., 2005. Data Summary from Second AIAA Computational Fluid Dynamics Drag Prediction Workshop. *Journal of Aircraft*, **42**, No. 5.

[44] Vassberg, J. C. & al., 2008. Abridged Summary of the Third AIAA Computational Fluid Dynamics Drag. Prediction Workshop. *Journal of Aircraft*,**45**, No. 3.

[45] van Dam, C. P., 1999. Recent Experience with Different Methods of Drag Prediction. *Progress in Aerospace Sciences*, **35**, 751–798.

[46] Paparone, L. & Tognaccini, R., 2003. Computational Fluid Dynamics-Based Drag Prediction and Decomposition. *AIAA Journal* **41**, 9.

[47] Tognaccini, R., 2003. Methods for drag decomposition, Thrust-drag bookkeeping from CFD calculations. *VKI Lecture Series 2003-02, CFD-Based.*

[48] Tognaccini, R., 2005. Drag Computation and Breakdown in Power-on Conditions. *Journal of Aircraft*,**42**, No. 1, 245–252.

[49] Beddoes, T. S. & Leishman, J. G., 1986. A generalised model for airfoil unsteady aerodynamic behaviour and dynamic stall using the indicial method. 42^{nd} *Annual Forum of the American Helicopter Society.*

[50] Andersen, P. B., Gaunaa, M., Bak, C.& Hansen M. H., 2007. A dynamic Stall Model for Airfoils with Deformable Trailing Edges. *Journal of Physics: Conference Series*, **75**, No 1., 012028

[51] Johnson, W. , 1998. Rotorcraft Aerodynamics Models for a Comprehensive Analysis. *American Helicopter Society 54th Annual Forum*, May 20-22. Revised version of paper, Washington, DC.

[52] Destarac, D.& van der Vooren, J., 2004. Drag-thrust analysis of jet-propelled transonic transport aircraft, definition of physical drag components. *Aerospace Science and Technology*, **8**, 545–556.

[53] Yamazaki, W., Matsushima, K. & Nakahashi, K., 2008. Aerodynamic Design Optimization Using the Drag-Decomposition Method. *AIAA Journal*, **46**, No. 5.

[54] Spalart, P. R., 2008. On the far wake and induced drag of aircraft. *J. Fluid Mech.*, **603**, 413–430.

[55] Theodorsen, T., 1935. General theory of aerodynamic instability and the mechanism of flutter. *NACA-Report*, 496.

[56] Tannehill, J. C., Anderson, D. A. & Pletcher, R. H., 1997. Computational Fluid Dynamics and Heat Transfer. *Washington, Taylor & Francis.*

[57] Hirt, C. W., Amsden, A. A., & Cook, J. L., 1974. An Arbitrary Lagrangian-Eulerian Computing Method for All Flow Speeds. *Journal of Computational Physics*, **14**, 227–253.

[58] Marongiu, C., Panizza, A. & Vitagliano, P. L., 2007. A Moving Grid Method for Unsteady Flow Computations. 18^{th} *AIAA Computational Fluid Dynamics Conference*, 25-28 June, Miami, Florida, AIAA 2007-4470.

[59] Pope, S. B., 2000. *Turbulent flows.* Cambridge University Press.

[60] Catalano, P.& Amato, M., 2000. Assessment of κ-ω turbulence modeling in the CIRA flow solver ZEN. *ECCOMAS 2001 Conference*, Swansea, Wales.

[61] Wilcox, D. C., 1998. Turbulence modeling for CFD. *2nd edn. DCW Indus.*, La Ca-ada, CA, 1998.

[62] Kok, J., 2000. Resolving the Dependence on Free-Stream Values for the κ-ω Turbulence Model. *A*IAA Journal, **38**, 7, 1292–1295.

[63] Menter, F. R., 1994 Two Equation Eddy Viscosity Turbulence Models for Engineering Applications. *A*IAA Journal, **32**, 8,1598–1605.

[64] Catalano, P. & Amato, M. , 2003. An Evaluation of RANS Turbulence Modelling for Aerodynamic Applications. *Aerospace Science and Technology Journal*, **7**, 7, 493–509.

[65] Jameson, A., Schmidt, W. & Turkel, E., 1981. Numerical Solutions of the Euler Equations by Finite Volume Methods Using Runge-Kutta Time Stepping Schemes. *AIAA Paper*, 1981–1259.

[66] Jameson, A., 1991. Time Dependent Calculations Using Multigrid, with Applications to Unsteady Flows Past Airfoils and Wings. *AIAA Paper* , 1991–1596.

[67] Marongiu, C., Catalano, P., Amato, M., & Iaccarino, G., 2004. U-ZEN: A Computational Tool Solving U-RANS Equations For Industrial Unsteady Applications. 34^{th} *AIAA Fluid Dynamics Conference & Exhibit*, 28 June - 1 July, Portland, OR, AIAA 2004–2345.

[68] Marongiu, C., Vitagliano, P. L., Catalano, P., Tarantino, V., & di Serafino D., 2005. An Improvement of the Dual Time Stepping Technique for Unsteady RANS Computations. *European Conference for Aerospace Sciences*, 4-7 July, Moscow.

[69] Batchelor, G. K., 1967. An Introduction to Fluid Mechanics. *Cambridge Mathematical Library.*

[70] Ashley, H., 1965. Aerodynamics of wings and bodies. *Dover pubblications Inc. New York.*

[71] Saffman, P. G., 1992. *Vortex Dynamics.* Cambridge Monographs on Mechanics and Applied Mathematics.

[72] Bisplinghoff, R. L., Ashley, H. & Halfman, R. L., 1955. *Aeroelasticity.* Dover.

[73] Wu, J. C., 1981. Theory for Aerodynamic Force and Moment in Viscous Flows. *AIAA Journal*, **19**, 4.

[74] Wu, J.-Z., Ma H. -Y. & Zhou M. -D., 2006. *Vorticity and Vortex Dynamics.* Springer.

[75] Wu, J.-Z., Lu X.-Y.& Zhuang L.-X, 2007. Integral force acting on a body due to local flow structures. *J. of Fluid Mech.*, **576**, 265–286.

[76] Wu, J.Z., Zhou, Y., Lu, X.Y.& Fan, M.,, 1999. Turbulence force as a diffusive field with vortical sources. *Physics of Fluids*, **11**,3, 627–635.

[77] Schlichting, H. , 1978. *Boundary-Layer Theory.* McGraw-Hill, New York.

[78] McCroskey, W.J., 1987. *A Critical Assessment of Wind Tunnel Results for the NACA0012 Airfoil.* AGARD CP-429.

[79] Betz, A. , 1925. *A Method for the Direct Determination of Profile Drag.* ZFM, **16**.

[80] Lee, T. & Gerontakos, P. , 2004. An experimental analysis of the flow over an oscillating airfoil. *J. of Fluid Mech.*, **512**, 313–341.

[81] Lee, T. & Basu, S., 1998. Measurements of unsteady boundary layer developed on an oscillating airfoil using multiple hot-film sensors. *Experiments in Fluids*, **25**, 108–117.

[82] Radespiel, R., Windte, J. & Scholz, U., 2006. Numerical and Experimental Flow Analysis of Moving Airfoils with Laminar Separation Bubbles. *AIAA Aerospace Sciences Meeting and Exhibit*, Reno, NV, Jan-3-5, AIAA 2006–0501.

[83] Catalano, P. & Tognaccini, R., 2009. Influence of Free-stream Turbulence on Simulations of Laminar Separation Bubbles. 47^{th} *AIAA Aerospace Sciences Meeting and Exhibit*, Jan., Orlando, FLorida, AIAA paper 2009-1471.

[84] Hansman, Jr. R. J. & Craig, A. P., 1987. Low Reynolds Number Tests of NACA 64-210, NACA0012, and Wortmann FX67-K170 Airfoils in Rain. *Journal of Aircraft*, **24**,8.

[85] Alrefai, M.& Acharya, M., 1996. Controlled Leading-Edge Suction for Management of Unsteady Separation over Pitching Airfoils. *AIAA Journal*, **34**, 11.

[86] Shur, M., Spalart, P. R., Strelets, M. & Travin, A., 1999. Detached-eddy simulation of an airfoil at high angle of attack., *Engineering Turbulence Modelling and Experiments*, **4**, Eds. W. Rodi and D. Laurence.

[87] Birch, D. & Lee, T., 2005. Effect of trailing-edge flap on the tip vortex flow. *Journal of Aircraft*, **42**,2, 442–447.

[88] Marchman, J. F., 1987. Aerodynamic Testing at Low Reynolds Numbers. *Journal of Aircraft*, **24**, 2.

[89] Sheng, W., Galbraith, R. A. McD. & Coton, F. N., 2006. A New Stall-Onset Criterion for Low Speed Dynamic-Stall. *Journal of Solar Engineering*, **128**, 4.

[90] Chadrasekhara, M. S. & Carr, L. W., 1990. Flow Visualization Studies of the Mach Number Effects on Dynamic Stall of an Oscillating Airfoil. *Journal of Aircraft*, **27**, No 6., 516–522.